The imprint of galaxy formation and the nature of dark matter on galactic scales

VICTOR JUAN FOROUHAR-MORENO

The imprint of galaxy formation and the nature of dark matter on galactic scales

Victor J. Forouhar Moreno

A thesis presented for the degree of

Doctor of Philosophy

Institute for Computational Cosmology

Ogden Centre for Fundamental Physics

Department of Physics

Durham University

September 2023

The imprint of galaxy formation and the nature of dark matter on galactic scales

Victor J. Forouhar Moreno

Abstract

The standard model of cosmology assumes most matter is made up of cold dark matter (CDM), which provides an excellent agreement between observations and predictions concerning the large-scale structure of the Universe. On smaller scales, discrepancies in its sub-galactic distribution exist, motivating alternative dark matter (DM) models. These scales are nonetheless poorly resolved in cosmological simulations and susceptible to the effects of galaxy formation. This thesis explores both issues in the context of Milky Way-mass haloes (MW) and their satellite population. We first investigate the role of internal processes of galaxies hosted in $\sim 10^{12}\,\mathrm{M}_{\odot}$ DM halos in shaping their central DM density, finding that stellar bars and gas blowouts driven by Active Galactic Nuclei counteract gravitational contraction. As both of these components reflect the evolutionary history of their host, this underscores the importance of accounting for assembly histories when modelling contracted haloes. The second part of this thesis compares the properties of the satellite population of MWs across cold, warm (WDM) and self-interacting (SIDM) dark matter models, finding that the assumed nature of the DM affects their abundance, characteristic mass function, and spatial distribution. This reflects a suppression in the number of galaxies forming (WDM) and more tidal stripping (SIDM) compared to CDM. As the stellar halo is built from the stripped remnants, its spatial distribution and phase-space structure are also affected. However, certain galaxy formation models result in similar structural differences. Given the uncertainty in how to model star formation, this hinders the use of the brightest satellites as powerful constraints on the nature of DM. Conversely, haloes hosting ultra-faint galaxies are less affected by these degeneracies, making them better constraints on the nature of DM. These are, nonetheless, poorly resolved in simulations, complicating comparisons to real data. We conclude this thesis by discussing preparations targeted towards running the highest-resolution simulation of a MW halo in CDM and WDM to date, which will provide unbiased predictions concerning its satellite population. Together with upcoming surveys, which will provide the deepest characterisation of the real MW satellite population as of yet, this will enable the use of ultra-faints to further constrain the nature of the DM.

Supervisors: Carlos Frenk, Shaun Cole & Alejandro Benitez-Llambay

Acknowledgements

To Aude, who has been my strongest pillar through thick and thin of my PhD journey. Thank you for listening me talk about science mumbo-jumbo constantly, helping me get organised (with varying degrees of success) and being there when the stress of quickly approaching deadlines got the best of me. This thesis is as much mine as it is yours.

To my supervisors, whose unwavering support throughout these last four years have helped me come out of this experience (relatively) unscathed. I will forever cherish Carlos' endless repertoire of anecdotes, Shaun's illuminating coffee break discussions and Alejandro's commitment to help me, regardless of whether it was a quick question or a three-hour long C++ rubber ducking session. Thank you all for sharing your values with me, and making me the scientist I am today.

To my office, who have been on the receiving end of my endless rants, and heard the click-clack of my mechanical keyboard every day for the past year. I was lucky enough to share an office with you three, but unlucky to not have done it since the beginning. We have definitely had much more fun than what should be allowed in a PhD.

To the Durham astronomy group, who made me look forward to coming to the office each morning. Thank you Adriano, Aidan, Alex R., Andreia, Anna G., Azi, Behzad, Ben, Chris, Dimitri, Ellen, Emmy, Francesca, Isabel, Jack, James N., Joaquin A., Joaquin S., Josh, Kyle, Nicole, Omer, Scott, Sergio, Shaun B., Simone, Willem and many others.

Thank you.

Contents

Declaration

The work in this thesis is based on research carried out at the Institute for Computational Cosmology, Ogden Centre for Fundamental Physics, Department of Physics, University of Durham, United Kingdom. No part of this thesis has been submitted elsewhere for any other degree or qualification, and it is the sole work of the author unless referenced to the contrary in the text.

Some of the work presented in this thesis has been published in journals and conference proceedings - the relevant publications are listed below.

Publications

Forouhar Moreno V., Benitez-Llambay A., Cole S. Frenk C. 2022, MNRAS, 517, 5627 – Chapter 2

Forouhar Moreno V., Benitez-Llambay A., Cole S. Frenk C. 2022, MNRAS, 511, 3910 – Chapter 3

List of Figures

List of Tables

First Chapter

Introduction

1.1 The Standard Cosmological Model

1.1.1 Modelling the Universe

Modelling the dynamical evolution of our Universe involves an accurate description of the forces that play an important role on large scales. Only two out of the four fundamental forces are sufficiently long-range – i.e. the potential falls off as the inverse of the distance – to play a driving role: gravity and electromagnetism. However, based on observations of the large-scale structure of the Universe, the latter plays no major role, suggesting that the Universe is electrically neutral.

General Relativity postulates that gravity is not a force *per se*, but rather a consequence of the curvature of space-time itself. Formulated over a century ago, its predictions have been corroborated over a wide range of scales and distances (Dyson et al., 1920; Shapiro, 1964; Nordtvedt, 1968; Hafele & Keating, 1972; Vessot et al., 1980; Taylor & Weisberg, 1989; Everitt et al., 2011; Abbott et al., 2016; Psaltis et al., 2020; GRAVITY Collaboration et al., 2020; Touboul et al., 2022), which have cemented it as the best theory of gravity we have.

Nonetheless, the complexity involved in solving the Einstein Field Equations, which comprise a set of ten non-linear partial differential equations, means that simplifying assumptions need to be made in order to have (more tractable) cosmological applications of General Relativity.

One key assumption is the so-called Cosmological Principle, which states that the Universe is homogeneous and isotropic on large scales. In other words, there is no preferred location or direction, which is in stark contrast to the geocentric views of the first astronomers. In

practice, it means that the dynamical state of the Universe only depends on the average density of its constituent components, ρ_i. This is expressed in the Friedmann equations (e.g. Weinberg, 2008):

$$\left(\frac{\dot{a}}{a}\right)^2 = \frac{8\pi G}{3}\sum_i^N \rho_i + \frac{kc^2}{a^2}\,, \tag{1.1}$$

$$\frac{\ddot{a}}{a} = -\frac{4\pi G}{3}\sum_i^N \left(\rho_i + \frac{3p_i}{c^2}\right), \tag{1.2}$$

where a is the time-evolving scale factor, and k is a constant related to the curvature of the Universe, and whether it is flat ($k = 0$), positively ($k > 0$) or negatively curved ($k < 0$). By modelling the components as ideal fluids, i.e. assuming their pressure is proportional to their density, $p = w\rho c^2$, the evolution of their average density is given by:

$$\rho(a) = \rho_0\left(\frac{a}{a_0}\right)^{-3(1+w)}\,, \tag{1.3}$$

where $\rho_0 \equiv \rho(a_0)$ is the density value at a reference expansion factor a_0, which is typically taken to be $a_0 = 1$ at the present time.

1.1.2 Towards a Standard Model

The first application of General Relativity to Cosmology was made by Einstein (Einstein, 1917), when he proposed a static, flat Universe. This model required a non-zero cosmological constant, which provided a repulsive force to counteract the eventual collapse that would be caused by gravity. However, this static view of the model fell out of favour over the next decade.

Firstly, it was proven to be unstable (Eddington, 1930), since any deviation from the delicate balance between gravity and the repulsiveness of the cosmological constant, either on local or cosmological scales, would cause a runaway expansion or contraction of the Universe. Additionally, mounting observational evidence suggested that most extragalactic *nebulae* – later identified as galaxies in their own right Hubble (1926) – were receding away from us (Slipher, 1917). A dependence between their recession velocity and distance was eventually found (Hubble, 1929), and an expanding universe became accepted (Einstein & de Sitter, 1932).

Alongside these developments, other world-models were developed, like the matter-devoid, exponentially expanding de Sitter Universe (de Sitter, 1917). It garnered the attention of observers (Wirtz, 1924), and seems to be an accurate description of the very early and late Universe. Nonetheless, the equations describing the evolution of any homogeneous and isotropic universe were derived in Friedmann (1922). These were later independently derived by Belgian priest Lemaître, who established the relation between an expanding Universe and a redshifting of galaxies (Lemaître, 1927).

Given that the Universe is expanding, it should have been in a denser and hotter state in the past. This motivated Lemaitre to propose a 'primaeval atom' view (Lemaître, 1931), which later evolved into the Big Bang model. This hypothesis had two key consequences, which were observationally confirmed over the following decades:

- **Nucleosynthesis**. No atomic nuclei could have existed during the first few minutes of the Universe, as extremely high temperatures prevented protons and neutrons from becoming bound together. As the Universe expanded, temperatures became sufficiently cool for nuclear reactions to occur during a brief time period until these were unable to be sustained by a low baryon density and temperatures (Gamow, 1946). This results in primordial elemental abundances that are sensitive to the expansion rate of the Universe and baryon density (Alpher et al., 1948; Wagoner et al., 1967).

- **Relic radiation**. The now-bound nuclei were ionised, and so the electron plasma interacted strongly with photons, resulting in a very short mean free path for the latter. Neutral atoms eventually formed, and the radiation propagated relatively unimpeded from this last scattering surface (Dicke et al., 1965). The relic radiation was serendipitously discovered by Penzias & Wilson (1965) in the microwave spectrum, which has a homogeneous black body emission of $T = 2.73$ K.

This was a tremendous success for the Big Bang model, but there were two glaring issues in cosmology at the time. Firstly, the Cosmic Microwave Background (CMB) was largely isotropic across the whole sky, suggesting it was casually connected when recombination

($z \sim 1100$) occurred. However, light only had a finite amount of time to casually connect regions that were much smaller in scale (*horizon problem*). Additionally, the density parameter was already known to be $0.1 \leq \Omega \leq 10$, and since any curvature quickly gets amplified with time, this suggested the Universe had to be extremely close to flat at early times (*flatness problem*).

The proposed solution was inflation, in which a small, casually connected region in space underwent a period of exponential expansion (Guth, 1981; Linde, 1982). This process smoothed out any curvature, removing the fine-tuning previously required, and explained why the CMB emission was in thermal equilibrium. It also provided a way to seed density fluctuations from quantum fluctuations prior to inflation (Hawking, 1982; Guth & Pi, 1982; Starobinsky, 1982)

Over the following decades, increasingly precise measurements cemented the expanding universe model but suggested that most matter was invisible ($\Omega_\mathrm{m} > \Omega_\mathrm{b}$) and that the Universe seemed to be far from being flat based on its matter content alone ($\Omega_\mathrm{m} \sim 0.3$). Given the (inflation-based) theoretical preference for $\Omega_\mathrm{tot} = 1$, some began to consider a non-zero cosmological constant as a possibility (e.g. Davis et al. 1985), further motivated by the observed large-scale clustering of galaxies (Efstathiou et al., 1990). A non-zero Ω_Λ was independently confirmed by measuring the accelerating expansion of the Universe using distant supernovae (Riess et al., 1998).

With the latest Cosmic Microwave Background results measured by the Plank satellite, our Universe is flat, consistent with inflation and has the following present-day values for density parameters in the preferred ΛCDM cosmology (Planck Collaboration et al., 2020b):

$$\Omega_{\mathrm{b},0} = 0.0493 \pm 0.0002, \quad \Omega_{\mathrm{m},0} = 0.3166 \pm 0.0084, \quad \Omega_{\Lambda,0} = 0.6847 \pm 0.0073\,.$$

1.1.3 The Need for Dark Matter

The term dark matter was coined over one hundred years ago by Kapteyn (1922), as he recognised that dynamical modelling probes the *total* mass, which may not necessarily be the luminous mass (e.g. dim stars). Although he found no evidence for substantial amounts

of dark matter based on the data available at the time, the advances in astronomical instrumentation and observations that facilitated the development of the Standard Cosmological Model also highlighted that most matter in the Universe is dark. Several independent avenues of research – all astronomical in nature – suggest its existence.

Dynamics

The first evidence for high mass-to-light ratios was provided in the context of the vertical acceleration of the Milky Way (Oort, 1932), and later more spectacularly in relation to the orbital velocity dispersion of the Coma Cluster members (Zwicky, 1933). The presence of undetected mass was later found to be prevalent across galaxies, based on flat rotation curves (Rubin & Ford, 1970; Roberts & Whitehurst, 1975), high velocity dispersion of dwarf spheroidals (Faber & Lin, 1983), Local Group timing arguments (Kahn & Woltjer, 1959; Lynden-Bell, 1981) and the stability of stellar disks (Ostriker & Peebles, 1973).

Intracluster gas

Most of the baryonic mass in clusters is *optically* dark, as it is in the form of hot gas that emits in X-rays. The high pressures resulting from temperatures in excess of $\sim 10^7$ K require a large amount of mass to prevent the hot corona from evaporating away, further supporting high mass-to-light ratios (Einasto et al., 1974; Mathews, 1978).

Gravitational lensing

Distortions in the shape and surface brightness of galaxies constitute a direct probe to infer the distribution of matter. Near the centre of clusters and massive galaxies, strong lensing effects help constrain the mass distribution (Tyson et al., 1998; Treu & Koopmans, 2004; Pointecouteau & Silk, 2005). Those undergoing mergers also provide constraints on how collisionless the dark matter is, based on the offsets between the baryonic and total centre of mass (Clowe et al., 2006; Harvey et al., 2015). On larger scales, weaker lensing effects imprint statistically measurable distortions in the shape of galaxies, allowing one to measure mass profiles of around

galaxies (Mandelbaum et al., 2006) and the matter density parameter (Abbott et al., 2022), suggesting $\Omega_m > \Omega_b$.

Big Bang Nucleosynthesis

The abundance of elements produced during Big Bang Nucleosynthesis is sensitive to the early Universe expansion rate and the baryon density (Gamow, 1946). In particular, the relative abundance of deuterium, He^3, He^4, and Li^7, measured using pristine environments (e.g. atmospheres of metal-poor stars; Asplund et al. 2006), place strong constraints on the baryon-to-photon number density and therefore the baryon density. This resulted in estimates suggesting $\Omega_b < \Omega_m < 1$ (Wagoner et al., 1967).

Baryon Acoustic Oscillations

Prior to recombination, baryons were ionised and, therefore, tightly coupled to photons. Primordial perturbations in this baryon-photon fluid propagated as sound waves until recombination, imprinting a characteristic scale when they dissipated (Peebles & Yu, 1970; Sunyaev & Zeldovich, 1970). This feature has been detected in the angular power spectrum of temperature anisotropies of the CMB (Miller et al., 1999; de Bernardis et al., 2000) and the distribution of galaxies (Cole et al., 2005; Eisenstein et al., 2005). Since the (neutral) dark matter is unaffected beyond gravitational attraction, this effect is suppressed compared to in a universe whose matter density is dominated by baryons (Holtzman, 1989).

The inference of the presence and existence of dark matter is based on the assumption we understand how gravity works on cosmological and galactic scales, but Newtonian gravity and General Relativity have been validated on gravitational fields that are stronger than those relevant to the aforementioned observations. This has motivated alternative models seeking to explain the above observations by invoking a change in the law of gravity, rather than the presence of an undetected matter component that outnumbers baryons six to one. The most studied of them, MOND (Milgrom, 1983), makes it so gravity behaves differently below an empirically motivated acceleration scale ($a_{\mathrm{MOND}} \sim 10^{-8}\,\mathrm{cm\,s^{-2}}$; Gentile et al.

2011). Despite its ability to reproduce some observations without the need of dark matter, e.g. flat rotation curves of galaxies (Milgrom, 1988; McGaugh et al., 2016) and the shape of the Tully-Fisher relation (McGaugh, 2012), it fails for others, such like the CMB power spectrum (Dodelson, 2011), present-day distribution of galaxies (Pardo & Spergel, 2020), merging clusters (Sanders, 2003), etc. Recent extensions have been able to circumvent some of these problems (e.g. relativistic MOND is able to fit the observed CMB and matter power spectrum; Skordis & Złośnik 2021), but dark matter still appears to be the simplest explanation we have to explain the present evidence.

In summary, the observational evidence indicates that **most matter in the Universe is dark and non-baryonic, is present in all galaxies and clusters, and behaves like a collisionless fluid on large scales**.

1.2 Cold Dark Matter

The mounting evidence underscoring the need for dark matter was accompanied by many advancements in the realm of particle physics, which culminated in the Standard Model of Particle Physics. These two fields worked in tandem to propose well-motivated particle candidates that could explain the aforementioned astronomical observations whilst also solving lingering challenges present in the latter. This resulted in Cold Dark Matter (CDM) emerging as the prevailing model for dark matter.

1.2.1 Theoretical motivations

Given the evidence suggesting that dark matter only interacts gravitationally with ordinary matter, any viable particle candidate should be massive and, at most, couple weakly with the Standard Model of particles. Indeed, if said particles are produced in thermal equilibrium during the early Universe, their final number density depends only on their mass and interaction cross-section. A value similar to that expected from the weak force yields the required energy density to account for the value of Ω_{DM}. This fact has come to be known as the Weakly Interacting Massive Particle (WIMP) miracle.

It is therefore sensible to consider the left-handed neutrino as a natural candidate for the dark matter (Cowsik & McClelland, 1973), due to their non-zero mass (Fukuda et al., 1998) and weak interactions. However, the power and scale of primordial density perturbations depend sensitively on the mass of such a particle, as perturbations smaller than its free-streaming length are smoothed out. The earliest numerical simulations of structure formation were already able to rule out the Standard Model neutrino as the dominant component of dark matter, as it represented an unrealistically 'hot' dark matter model that does not reproduce the observed large-scale distribution of galaxies (White et al., 1983).

Nonetheless, interest still remains in neutrino-like particles as dark matter candidates, especially in connection to extensions to the Standard Model of Particle Physics. In particular, the question of why left-handed neutrinos have any mass at all and why it is so small in comparison to other fundamental particles remains unanswered. Grand Unified Theories like the Pati-Salam model (Pati & Salam, 1974) predict right-handed neutrinos that obtain their mass through spontaneous symmetry breaking through a Higgs-like mechanism. In such models, the predicted mass of the right-handed neutrino becomes larger as its left-handed counterpart becomes less massive. This 'see-saw' mechanism provides an explanation as to why neutrinos have small masses (Ma, 1998) and predicts massive 'sterile' neutrinos that could be the cold (or warm) dark matter (Dodelson & Widrow, 1994).

Beyond neutrinos, popular extensions to the Standard Model also predict WIMP-like candidates. In supersymmetry (Wess & Zumino, 1974), the neutralino, which is the lightest stable particle, provides such a candidate (Ellis et al., 1984). Additionally, solutions intended for the the strong charge-parity problem also result in natural dark matter candidates beyond WIMPs (e.g. axions; Peccei & Quinn 1977)

1.2.2 Fundamental Predictions

The early Universe was extremely homogeneous, but any deviations from the background density were amplified through gravity, with overdense (underdense) regions resulting in

the formation of cosmic structures (voids). In an expanding Universe, sufficiently overdense regions eventually decouple from the Hubble flow, at which point they begin to contract and eventually collapse (Gunn & Gott, 1972).

In general, this can proceed in a top-down or hierarchical fashion. In the former, the largest scales are the first to collapse, which then undergo fragmentation to give rise to smaller scale objects (Zel'dovich, 1970). On the other hand, the hierarchical growth of structure begins at the smallest scales and proceeds in a bottom-up fashion (Peebles, 1971).

Given the negligible thermal velocity of Cold Dark Matter due to its large mass, there is no suppression of any astronomically relevant density perturbations. This results in a power spectrum of density perturbations that increases monotonically towards smaller scales, resulting in the smallest structures forming first. Larger ones then grow through a combination of smooth mass accretion and mergers with neighbouring structures.

The end result of the process is the formation of virialised dark matter halos with density profile shapes that are well-described by a Navarro-Frenk-White (Navarro et al., 1995):

$$\rho_{\mathrm{NFW}}(r) = \frac{\rho_0}{\frac{r}{r_\mathrm{s}}\left(1+\frac{r}{r_\mathrm{s}}\right)^2}\,, \tag{1.4}$$

and an Einasto (Einasto, 1965) profiles over 20 orders of magnitude in halo mass (Wang et al., 2020) and independent of cosmological parameters (Navarro et al., 1997). The concentration $c \equiv R_{\mathrm{vir}}/r_\mathrm{s}$ of the halo is itself related to the average density of the Universe when the object formed.

Contrary to baryons, the dark matter is neutral and hence does not couple to the photon field prior to recombination. This allows its overdensities to grow whilst baryonic ones remain frozen. This results in a two-stage galaxy formation mode (White & Rees, 1978), whereby the dark matter provides the gravitational potential wells where gas is accreted, shock-heated, and eventually cools down enough to form stars.

Simulations of structure formation in a ΛCDM model result in a remarkable agreement between predictions and the observations of the large-scale structure of the Universe, including galaxy correlation functions (Springel et al., 2005b), redshift-space distortions

(Guzzo et al., 2008), strong lensing arc statistics (Wambsganss et al., 2004) and Lyman-α clustering (Alam et al., 2021).

1.2.3 Small-Scale Challenges

Despite the success of the Cold Dark Matter model in predicting the large-scale distribution of the Universe, there have been several historical tensions between observations and predictions on small scales.

Galactic dark matter distribution - *Core-cusp & diversity of rotation curves*

Given the prediction of universal dark matter density profiles, measuring its distribution around galaxies constitutes an important test of its nature. This can be inferred through a variety of probes involving stellar kinematics (Kleyna et al., 2001; Amorisco & Evans, 2012), gas kinematics (de Blok et al., 2008; Read et al., 2017), globular cluster distributions (Goerdt et al., 2006; Read et al., 2006b) and gravitational lensing (Tyson et al., 1998; Lagattuta et al., 2023). Despite the expected density cusp at small radii ($\rho \propto r^{-1}$), many galaxies seem to have central cores with constant densities (Moore, 1994; Flores & Primack, 1994), the so-called core-cusp problem (de Blok, 2010). Additionally, the fact that some have inferred density cores and others cusps is difficult to reconcile in simulations, which do not predict such diverse density profile shapes (Oman et al., 2015).

Satellite abundances - *Missing satellites & Too-big-to-fail*

Low mass haloes are more abundant than higher mass ones in CDM, both in the field (Jenkins et al., 2001) and as substructure (Springel et al., 2008). For Milky Way-mass haloes, the number of predicted subhaloes is much larger than satellites observed around the actual Milky Way, suggesting there are 'missing' satellites (Kauffmann et al., 1993; Klypin et al., 1999; Moore et al., 1999). On the high mass end of the subhalo population, DMO simulations also predict a larger number of dense and massive satellites than those observed around the Milky Way (Boylan-Kolchin et al., 2011). These would be so massive that they should have been detected today. This

noticeable missing fraction is in tension with expectations that the most massive objects should host the most massive galaxies. This problem might also be present in field dwarfs (Papastergis et al., 2015).

Satellite distributions - *Planes of Satellites & Radial distributions*

A subset of the galaxies comprising the satellite systems around the Milky Way (Lynden-Bell, 1976; Kunkel & Demers, 1976; Kroupa et al., 2005; Metz et al., 2007; Pawlowski et al., 2012), Andromeda (Ibata et al., 2013; Conn et al., 2013) and other galaxies (Müller et al., 2017; Martínez-Delgado et al., 2021) appear to be spatially co-planar, with the MW one having relatively well-aligned orbital poles (Metz et al., 2008; Pawlowski & Kroupa, 2013). Simulations exploring how common this is in CDM reveal that the expectation of said structures is low (Kroupa et al., 2005; Libeskind et al., 2009). In addition, the satellites of several Local Group hosts appear to be more radially concentrated than those predicted in simulations (Carlsten et al., 2020). This suggests that very low mass haloes need to be luminous in order to reproduce this trend, in tension with standard galaxy formation theory (Kelley et al., 2019; Graus et al., 2019).

Nonetheless, the observational significance of these tensions is still being actively discussed (see Sales et al. 2022 for a recent review), with observational biases, small number statistics and limitations in predictions often identified as the cause behind these tensions.

In the context of the core-cusp and diversity of rotation curves problems, non-circular motions and finite thicknesses in gas disks can bias the inferred mass distribution, further exacerbated if they are out of equilibrium (Marasco et al., 2018; Oman et al., 2019; Roper et al., 2022; Downing & Oman, 2023). Similar issues arise when using stars as tracers, which typically requires assuming spherical symmetry for a pressure-supported system in equilibrium, which is not always valid for Local Group dwarfs (McConnachie, 2012). Additionally, not all studies agree on the density slope for the same dwarf (e.g. Walker & Peñarrubia, 2011; Amorisco & Evans, 2012; Breddels et al., 2013).

The discussion is more nuanced where the spatial distribution of satellites is concerned. For the planes of satellites, there are conflicting reports on how common or uncommon they are, based on which definition or statistical measure is used (Cautun et al., 2015). Additionally, the predicted satellite population is likely biased as a reflection of the limited resolution of simulations (van den Bosch & Ogiya, 2018; Errani & Navarro, 2021), an issue that plays an important role in planar configurations (Bahl & Baumgardt, 2014; Sawala et al., 2023), radial distributions (Newton et al., 2018), and even luminosity functions (Bose et al., 2020). These can also be affected by transient effects that are not always captured in the simulations used to compare to observations (Santos-Santos et al., 2021).

1.3 Beyond Cold Dark Matter

The aforementioned small-scale challenges, together with the lack of observational confirmation of new physics in the particle sector (Aprile et al., 2018; Canepa, 2019), has driven a resurgence in alternatives to CDM. They primarily differ in their predictions concerning small scales, providing an avenue towards ameliorating astronomical observational tensions.

1.3.1 Warm Dark Matter

As discussed in §1.2.1, the power spectrum of primordial density perturbations is sensitive to the velocity distribution of the dark matter. The large-scale cut-off of hot dark matter results in unrealistic galaxy clustering, whereas cold dark matter *seems* to predict too much structure at small scales. It is, therefore, natural to consider an alternative that suppresses small structures but still behaves like cold dark matter on large scales.

One such possibility is the warm dark matter model, which has particle masses of $m \sim O(\mathrm{keV})$ and therefore leads to structure suppression below $10^{10}\,\mathrm{M}_\odot$ for the lightest variants. This alters the predicted properties and abundances of the least massive galaxies, whilst more massive ones remain unaffected.

There are well-motivated particle candidates that can account for the bulk of the warm dark matter, like certain models of sterile neutrinos that have predicted masses in the 1 to 100 keV range. In these models, they decay into left-handed neutrinos and high energy photons ($E_\gamma = \frac{1}{2}mc^2$), leading to X-ray emission that depends on the local dark matter density.

Tentative evidence for such signal ($E_\gamma \sim 3.55 \pm 0.03$ keV) has been found in the centres of the Milky Way, Andromeda and clusters (Boyarsky et al., 2014; Bulbul et al., 2014; Boyarsky et al., 2015). However, it is still unclear whether the origin of this emission is associated with instrumental or atomic lines or sterile neutrino decay, although it is not detected in blank sky observations and hence the first two are disfavoured – on the other hand, authors like Roach et al. (2023) argue that ambient emission originating from the galactic halo of the Milky Way should result in blank sky detections and hence the sterile neutrino interpretation is inconsistent. Other studies have also failed to detecte emission from environments where DM is expected to be abundant, like the centres of dwarf galaxies (Jeltema & Profumo, 2016) or a large fraction of individual galaxy clusters (Bhargava et al., 2020). Finally, a favourable or disfavourable detection, and its interpretation, is highly dependent on the background subtraction method (Boyarsky et al., 2020; Dessert et al., 2023). The upcoming X-Ray Imaging and Spectroscopy Mission (XRISM) – launch window opening on the 26th Aug. 2023 – will provide an independent probe with higher spectral resolution that will shed light on these conflicting reports.(XRISM Science Team, 2020).

The cut-off in the power spectrum also results in a delay of structure formation, becoming more severe towards the low mass scale. This affects the internal properties of haloes that do form, lowering their concentrations as a reflection of the lower density of the Universe when they formed, compared to their CDM counterparts (Ludlow et al., 2016; Bose et al., 2017). This, in turn, makes them more susceptible to efficient tidal stripping (Stücker et al., 2023a).

Lastly, monolithic gravitational collapse is expected to occur near the cut-off scale. The result of this formation mechanism is a halo with a density profile significantly steeper

($\rho \propto r^{-1.5}$) than an NFW. In CDM, this results in a large population of very dense low mass (e.g. $M \sim 10^{-7}\,\mathrm{M}_{\odot}$; Hofmann et al. 2001) subhaloes that significantly contribute to the predicted annihilation radiation signal (Delos & White, 2022; Stücker et al., 2023b). In WDM, monolithic collapse could occur for haloes hosting visible galaxies and hence provide additional constraints on the nature of dark matter (Delos, 2023).

1.3.2 Self-Interacting Dark Matter

Originally proposed in the context of the core-cusp problem, self-interacting dark matter has become a promising alternative to cold dark matter (Spergel & Steinhardt, 2000). The main difference with respect to cold (or warm) dark matter is that particles can scatter off each other, mediated by a dark force. This results in significant changes in the spatial and velocity distribution of particles within the inner parts of dark matter haloes, were the high densities allow many scatterings to take place in a Hubble time. This drives a structural transformation from a cuspy density profile into a cored isothermal one (Robertson et al., 2021).

Beyond the core-cusp problem, SIDM is also able to address other small-scale tensions. For example, the destruction rate of subhaloes is enhanced in such models, both through interaction with the background halo ('evaporation'; Gnedin & Ostriker 2001) and more effective tidal stripping due to flat density cores (Peñarrubia et al., 2010; Errani et al., 2022), leading to fewer satellites. Additionally, the decrease in the central densities alleviates the issues raised by the too-big-to-fail problem (Elbert et al., 2015).

Despite its initially phenomenological motivations, particles independently proposed to explain observations in high-energy astrophysics (Adriani et al., 2009) naturally predict self-interacting dark matter (Arkani-Hamed et al., 2009; Buckley & Fox, 2010a). Even more, models based on astrophysically-motivated SIDM exist (Kusenko & Steinhardt, 2001; Blennow et al., 2012), with some exhibiting more exotic behaviour than simple self-scattering (Fan et al., 2014; Boddy et al., 2016; Cirelli et al., 2019). A subset predicts dark radiation-mediated interactions, which results in small-scale perturbations being

suppressed (Vogelsberger et al., 2016).

The strongest constraints on the allowed values of the self-interaction cross-section originate from measuring the offset between the centre of mass and stellar component within merging clusters of galaxies (e.g. the Bullet and Musket Ball clusters; Randall et al. 2008; Dawson et al. 2012), with upper limits of ~ 1 cm^{2}g^{-1}. Similarly, low values are obtained based on the central densities local dwarf galaxies (Read et al., 2018).

However, these constraints are derived from very different velocity regimes. A velocity-dependent cross-section, a possibility that arises naturally in many realistic scattering potentials (e.g. Yukawa and Coulomb), can simultaneously predict collisionless behaviour on large scales and flat density cores in dwarf galaxies. The least massive of the latter can undergo gravothermal collapse (Lynden-Bell & Wood, 1968), a process that reverts them to cuspier profiles (Balberg et al., 2002) and that can be accelerated to occur in under a Hubble time if they are under the influence of gravitational tides similar to those experienced by the densest dwarfs in our local neighbourhood (Nishikawa et al., 2020). This offers a solution to the diversity of rotation curves, with current constrains on the value of the self-interaction cross-section at low relative velocities to be $30\text{cm}^2\,\text{g}^{-1} \lesssim \sigma \lesssim 100\,\text{cm}^2\,\text{g}^{-1}$ (Correa, 2021).

1.4 The Importance of Galaxy Formation

Baryons comprise a small fraction of the overall matter content of the Universe, but their inclusion in simulations is paramount for making accurate predictions. One obvious reason is that we observe gas, stars and dust, not dark matter. The former cluster differently than the latter, leading to a biased sampling of the underlying matter distribution (e.g. Kaiser, 1984; Efstathiou et al., 1988), and so any realistic comparison should be based on the former components.

Another fundamental motivation for their inclusion is that the inflows and outflows driven by galaxy formation, like energetic feedback and gas cooling at the centre of halos, drive potential changes that are sufficiently strong to alter the surrounding distribution of dark

matter. The strength and scale of these effects relate to how efficient galaxy formation is, which itself depends on halo mass (Moster et al., 2010; Guo et al., 2010). It peaks for Milky Way-mass haloes, and sharply drops at higher and lower masses, suggesting that different baryonic processes regulate galaxy formation on either side of this characteristic mass scale.

On large scales, the gas outflows triggered by Active Galactic Nuclei (AGN) develop a hot and low-density gaseous halo that cannot cool effectively, suppressing further star formation. Additionally, this leads to an overall decrease in the $z = 0$ matter power spectrum on scales of $0.3 - 40$ Mpc that amounts to $\sim 20\%$ decrease in amplitude, similar to effects caused by massive neutrinos (Hannestad et al., 2020; Elbers et al., 2021) and suppressing differences in modified gravity predictions (Arnold et al., 2019).

The formation of a sufficiently massive stellar component at the centre of dark matter haloes induces contraction that steepens the profile beyond the DMO prediction of $\rho \propto r^{-1}$ (Blumenthal et al., 1986; Schaller et al., 2015). Together with the tidal field exerted by the galaxy itself, substructure disruption in the inner parts is greatly enhanced (Richings et al., 2020). If the galaxy is a massive-enough thin disk, it becomes susceptible to bar instabilities (Hohl, 1971; Ostriker & Peebles, 1973; Efstathiou et al., 1982). These common (Eskridge et al., 2000; Menéndez-Delmestre et al., 2007) non-axisymmetric features couple gas, stars and dark matter together, enabling an efficient transfer of angular momentum between the three (Lynden-Bell & Kalnajs, 1972; Combes & Gerin, 1985; Athanassoula, 2003).

These changes are not universal across galaxies, as the low stellar mass of dwarf galaxies is insufficient to cause the above. Nonetheless, the shallowness of the potential well means that supernova feedback is effective at driving gas outflows from the galaxy. The sudden removal of gas transfers energy to the surrounding dark matter particles (Navarro et al., 1996a), with a series of outbursts resulting in more effective structural changes (Read & Gilmore, 2005; Pontzen & Governato, 2012; El-Zant et al., 2016). As such, bursty star formation histories (SFH) are more likely to result in baryon-driven core formation (e.g. Teyssier et al., 2013), with mounting observational evidence hinting at bursty SFH in dwarfs (Glazebrook et al., 1999; Emami et al., 2019), and at a correlation between SFH

and DM deficiency (Read et al., 2019; Bouché et al., 2022). However, this requires an effective coupling between dark matter and gas, achievable only when gas is sufficiently dense (Governato et al., 2010; Benítez-Llambay et al., 2019). This generally results in an efficiency of core formation that is mass-dependent (Di Cintio et al., 2014b; Tollet et al., 2016), but as it will be discussed in §1.4.1, it depends on the details of how gas physics is modelled.

Beyond the properties of present-day galaxies, baryonic physics also plays an important role at high redshifts. For example, a strong ionising background, like that present during reionization, results in the evaporation of gas from the lowest mass haloes. This deprives them of the fuel required to form stars, and hence all field haloes with present-day masses of less than $\sim 10^8 - 10^9$ $M_\odot$ are expected to be dark (Hoeft et al., 2006; Okamoto & Frenk, 2009; Fitts et al., 2017; Benitez-Llambay & Frenk, 2020; Katz et al., 2020; Nadler et al., 2020). As such, the predicted number of subhaloes around the Milky Way is much larger than the expected number of those hosting stars (Newton et al., 2018; Nadler et al., 2019; Drlica-Wagner et al., 2020), alleviating the missing satellites problem (Bullock et al., 2000).

Another consequence of the reionisation and supernova-driven loss of baryons in low-mass haloes is shallower potential wells compared to DMO simulations. This affects the subsequent rate at which they accrete mass, which results in an overall less massive halo at $z = 0$. This results in a substantially reduced number of predicted Milky Way satellites with $V_{\rm max} > 30\,{\rm km\,s^{-1}}$ (Sawala et al., 2013; Schaller et al., 2015), providing a solution for the Too-big-to-fail problem (Sawala et al., 2016).

1.4.1 Subgrid Physics

The dynamical range required to individually resolve the processes involved in galaxy formation in a cosmologically representative volume is beyond current – and likely future – computational capabilities. The latest generation of hydrodynamical simulations intended for large-scale cosmology achieve mass resolutions of $m_* \sim 2\times10^7 - 10^8$ $M_\odot$ (Villaescusa-

Navarro et al., 2021; Pakmor et al., 2023; Schaye et al., 2023), and zoom-in simulations of individual Milky Way-mass haloes typically reach $m_* \sim 10^3 - 10^5$ M$_\odot$ (Wang et al., 2015; Fattahi et al., 2016; Sawala et al., 2016; Hopkins et al., 2018; Buck et al., 2020; Grand et al., 2021). Higher resolutions ($m_* \sim 3 \times 10^2$ M$_\odot$) are achievable for low mass galaxies forming in isolation (Agertz et al., 2020), with individually resolved stars only recently been done for the smallest objects able to host galaxies (Gutcke et al., 2021)

This underscores the need to include baryonic physics as a 'subgrid' prescription, where the effects driven by sub-resolution processes – e.g. individual star formation – on resolvable scales need to be adequately modelled. This is done by using physically motivated models that rely on several free parameters whose values are typically found by calibrating a subset of predictions to observed data, although some do so on theoretical grounds, like the FIRE (Hopkins et al., 2018) and EDGE (Agertz et al., 2020) simulation suites.

However, there is no unique answer as to how to best represent unresolved baryonic physics in simulations, resulting in a multitude of different models that roughly reproduce observed scaling relations. There are, of course, additional observables that could help distinguish one realistic model from another, like gas outflows (Kelly et al., 2022) or black hole occupation fractions (Haidar et al., 2022), but their associated observational constraints are uncertain. Additionally, the choice of what scaling relations should be used to calibrate differs across models and scientific purposes, e.g. stellar mass functions, cluster gas fractions, stellar-size *versus* stellar mass relation, etc.

This relative freedom in how to model baryons results in different predictions of how they affect the surrounding dark matter. This is exacerbated for small scales, where the lack of observational constraints results in substantially different predictions concerning galaxy formation and their effects, e.g. whether the stellar-mass-to-halo-mass is a power law (Garrison-Kimmel et al., 2014; Wheeler et al., 2015) or exponentially truncated (Fattahi et al., 2018), or if gas blowouts can turn a density cusp into a flat density core (Pontzen & Governato, 2012; Di Cintio et al., 2014b; Tollet et al., 2016; Read et al., 2016; Fitts et al., 2017) or not (Vogelsberger et al., 2014; Bose et al., 2019). Nonetheless, higher resolution simulations ($m_{\rm part} \leq 1000$ M$_\odot$) able to track cold ($T \sim 100$ K) gas up to high-densities

typically predict the formation of cores resulting from gas blowouts in dwarf galaxies. Given the lesser reliance on subgrid assumptions, and hence whether they can adequately capture large scale effects (gas blowouts) driven by small scale events (individual supernovae), their predictions are expected to be more robust than lower resolution simulations unable to follow the important evolution of the ISM.

As baryonic effects can mimic the effects of dark matter, such as SIDM creating flat-density cores, it is particularly important to consider the range of allowed baryonic physics before identifying an observational signature as definitive evidence for an alternative dark matter model.

1.5 Outline of this thesis

This thesis focuses on understanding how small-scale predictions concerning MW-mass haloes and their surrounding galactic environment differ across different dark matter models, whilst accounting for the effects of galaxy formation physics.

Chapter 2 examines how the galaxy hosted at the centre of Milky Way mass-haloes couples to the dark matter distribution that surrounds them. Beyond the contraction caused by the gravitational attraction of the galaxy, we study which internal processes, if any, can further alter the distribution. For this purpose, we examine how the central DM density evolves in time, in connection to the properties of the central galaxies.

Following this, Chapter 3 explores how the properties of the satellite systems of Milky Way mass galaxies change depending on the underlying dark matter model that is assumed. For this, we simulate a cosmological box using cold, warm and self-interacting dark matter models. We then present how the properties of field haloes change across these different choices, and how that influences the final satellite properties. To quantify the degeneracy caused by galaxy formation physics, which is relatively unconstrained at the dwarf galaxy regime, we also employ different galaxy formation models to see how predictions are altered.

Chapter 4 uses a subset of the simulations presented in the previous chapter to examine whether the properties of stellar haloes surrounding MW-mass galaxies are sensitive to the nature of dark matter. To do so, we identify the ex-situ component within the MW virial region, and examine whether its mass, spatial and velocity distributions changes between simulations. We then conclude by exploring the properties of the remnants of galaxies that contributed to the build up of stellar halo, and whether this can explain any differences in the present day stellar haloes.

Finally, in Chapter 5, we lay out concrete plans towards the creation of the highest resolution dark matter-only simulations of a Milky Way mass halo, devised to provide unbiased predictions concerning the ultra-faint population of satellites around the Milky Way in CDM and WDM. This project is motivated by our findings in Chapter 3, as well as the recent works highlighting the prevalence of numerical disruption of substructure in cosmological simulations. We discuss the relevant technical and output requirements, and which substructure finding algorithm is the best for our purposes. We also present a new substructure finder that we have implemented in the state-of-the-art cosmological code GADGET-4 that is able to run on the fly.

Second Chapter

Baryonic effects on Milky Way scales

2.1 Introduction

Structure formation in a cold dark matter (CDM) universe proceeds in a hierarchical bottom-up manner. Small-scale overdensities are the first to decouple from the Hubble flow and undergo gravitational collapse. Their subsequent growth is driven by mergers with neighbouring structures and diffuse, smooth mass accretion from the surroundings. The end result is a bound, virialised halo of dark matter (DM) that can host a galaxy at its centre if it is massive enough (White & Rees, 1978; Benitez-Llambay & Frenk, 2020). N-body simulations that model the dark matter and baryons as a single collisionless fluid predict DM density profiles with shapes that are roughly independent of halo mass, cosmological parameters and the primordial fluctuation power spectrum (Navarro et al., 1996b; Wang et al., 2020). These density profiles are well fitted by the two parameter Navarro-Frenk-White (Navarro et al., 1996b, 1997) profile:

$$\rho_{\rm NFW}(r) = \frac{\rho_0}{\frac{r}{r_s}\left(1+\frac{r}{r_s}\right)^2}\,, \tag{2.1}$$

although more recent, higher resolution simulations suggest that the three parameter Einasto (1965) profile provides an even better fit (Navarro et al., 2004). The two parameters of the NFW profile are related to the halo virial mass and its concentration, both of which are tightly correlated. This is a consequence of the mass dependence of the formation epoch of haloes, as a result of which less massive halos typically have greater concentrations than more massive ones, reflecting the fact that they undergo gravitational collapse earlier, when

the universe was correspondingly denser.

The ubiquitous prediction of centrally divergent halo density profiles in CDM offers a test of whether dark matter is cold or not. This has motivated numerous studies comparing observations of the inferred DM density profiles to theoretical predictions on a wide range of scales, from dwarf galaxies (e.g Burkert, 1995; Agnello & Evans, 2012; Oh et al., 2015; Walker & Peñarrubia, 2011; Strigari et al., 2010) to rich galaxy clusters (e.g. Sand et al., 2002; Umetsu & Diemer, 2017; He et al., 2020). The comparisons are largely based on predictions stemming from purely collisionless dark matter-only (DMO) N-body simulations, where non-linear effects produced by baryons are unaccounted for. Processes associated with the formation and evolution of galaxies can have measurable effects on the structure of the DM haloes hosting them, such as changing the distribution of dark matter or redistributing angular momentum (e.g. Zavala et al. 2008; Schaller et al. 2015; Chan et al. 2015). The increasing availability of hydrodynamical cosmological simulations able both to reproduce many measured galaxy population statistics and have sufficient resolution to probe the galaxy-scale distribution of DM enables a more meaningful comparison between theory and observations (for a review, see Somerville & Davé 2015). These simulations use subgrid prescriptions to model processes such as star formation, gas cooling, feedback due to supernovae and AGN. The interplay between these processes leads to a complex and rich phenomenology that is missing in DMO simulations.

Initially, gas near a growing DM halo is dragged in due to the deepening gravitational potential well, shock heated and, if it can cool efficiently, it will sink towards the centre where star formation can commence once the gas density is large enough (White & Rees, 1978). The dissipative collapse of gas and its assembly in the central regions of DM haloes enhances their central density and makes them rounder (Dubinski, 1994; Kazantzidis et al., 2004; Debattista et al., 2008) than their typically triaxial (Dubinski & Carlberg, 1991; Hopkins et al., 2005) DMO counterparts. The effectiveness of the former response depends on a number of properties, such as the mass of the central galaxy, the assembly history of the halo and the phase-space distribution of DM particles (Abadi et al., 2010; Dutton et al., 2016; Artale et al., 2019). The first analytical models used to estimate

this response assumed 'adiabatic contraction' and circular orbits (Blumenthal et al., 1986; Ryden & Gunn, 1987) but were later expanded to take into account the orbital eccentricities of typical dark matter particles (Gnedin et al., 2004). More recently, there have been a number of extensions based on empirical fits to the measured response in hydrodynamical N-body simulations (Cautun et al., 2020), as well as orbital phase space modelling using integrals of motion (Callingham et al., 2020).

The assembly of gas and stars has other effects that are in direct competition with the contraction of the halo. The sudden expulsion, driven by supernovae explosions, of gas that had previously accumulated slowly at the centre of a dwarf galaxy halo can cause the central regions of the halo to expand (Navarro et al., 1996a). This can occur in a single disruptive event or in a series of more moderate perturbations that drive oscillations in the gravitational potential (Read & Gilmore, 2005; Pontzen & Governato, 2014). On cluster scales a similar outcome can result from powerful AGN-driven outbursts (Martizzi et al., 2013). Similarly, dynamical friction exerted on infalling gas clumps by dwarf-scale haloes (El-Zant et al., 2001; Mashchenko et al., 2006) or merging galaxies in cluster-scale haloes (El-Zant et al., 2004; Laporte et al., 2012) could also lower the central dark matter density.

The details of how star formation is modelled determines the degree of gravitational coupling between the gas and the DM halo, and thus influences how effectively gas blowouts can alter the inner contents of dark matter haloes (Benítez-Llambay et al., 2019). This explains differences in the predicted density profiles of dwarf galaxies between simulations employing high density thresholds and those employing lower ones. Whilst the former are able to accumulate sufficient quantities of gas in the central regions of the halo prior to the gas being blown out, low density thresholds never reach this point. Another important aspect of gravitational perturbations is the timescale on which they operate. As discussed in the Appendix of Benítez-Llambay et al. (2019), perturbations that last longer, compared to the typical dynamical time of the shell, remove DM more effectively. If the perturbation timescale is sufficiently long, the effectiveness of each individual perturbation in heating the DM becomes maximal. This means that the integrated effect is solely dependent on the number of such perturbations

Finally, torques exerted by non-axisymmetric features are able to redistribute angular momentum between baryons and DM, as well as within the galaxy itself (Lynden-Bell & Kalnajs, 1972; Lynden-Bell, 1979). One example are stellar bars, which are present in a significant fraction of nearby spiral galaxies (Eskridge et al., 2000; Sheth et al., 2008; Skibba et al., 2012; Buta et al., 2015) and in our own Milky Way (MW) (Binney et al., 1991; Weiland et al., 1994; Dwek et al., 1995; Ness et al., 2016). The formation of a bar can be driven by an instability resulting from a kinematically cold and gravitationally important disc, as appreciated in early N-body simulations (e.g Miller et al. 1970; Hohl 1971). An alternative bar formation mechanism relies on external triggers such as tidal interactions caused by a close flyby or a merger (Noguchi, 1987; Łokas et al., 2016; Martinez-Valpuesta et al., 2017). These processes can also reconstitute previously existing bars (Berentzen et al., 2004).

The subsequent evolution of the bar is determined by exchange of angular momentum, which can lead to its strengthening and lengthening (Athanassoula, 2003). This exchange occurs near orbital resonances. While some authors argue that as many as 10^8 particles are required to model the resonances (e.g. Weinberg & Katz 2007a,b; Ceverino & Klypin 2007), others find less stringent conditions on the grounds that a time-evolving bar pattern speed broadens the resonant regions (e.g. Sellwood 2006). The net flow of angular momentum depends on the dynamical and spatial properties of the constituent components of the system (for a review, see Athanassoula 2013). The regions of the disc within the corotation radius of a bar lose it, whereas those beyond gain it. On the other hand, spheroidal components such as the DM halo and the stellar bulge are only able to acquire it. Consequently, bar driven changes in the distribution of angular momentum can change the structural properties of discs (Debattista et al., 2006), cause classical bulges to acquire net rotation (Saha et al., 2012; Kataria & Das, 2019) and alter the central density of DM haloes (Weinberg & Katz, 2002; Holley-Bockelmann et al., 2005; Sellwood, 2008; Dubinski et al., 2009; Algorry et al., 2017)

The efficiency with which all these different processes are able to alter the central density of dark matter depends largely on the mass scale under consideration. For example, the small

amount of baryons collected at the centre of very faint dwarfs cannot alter significantly the inner DM content of their host halo. On the other hand, if too many baryons end up locked in stars in larger haloes, the DM contracts in response to them. There is thus a narrow range in mass in which supernovae-driven gas blowouts are effective at driving DM mass out (e.g. Di Cintio et al., 2014a; Tollet et al., 2016). It is then common practice to assume that larger haloes, particularly those with mass comparable to that of our Milky Way, are only subject to the contraction caused by baryons, ignoring altogether the competing effects caused by other processes, such as AGN-driven outflows of gas, or the presence of a massive bar at the centre.

In this chapter we revisit these ideas using a high-resolution hydrodynamical simulation of the EAGLE project. In particular, we study in detail the time evolution of the inner DM content of a sample of Milky Way-mass haloes and search for events that alter it. Understanding the role of baryons in these haloes is important for a wide range of applications, from mass estimates of our Milky Way (Cautun et al., 2020) to informing direct and indirect searches for dark matter (Calore et al., 2015; Bozorgnia et al., 2016; Bozorgnia & Bertone, 2017; Schaller et al., 2016).

The chapter is structured as follows. Section 2 describes the simulations as well as our selection of a sample of galaxies for analysis. Section 3 presents our results, focusing first on gas blowouts and then on stellar bars, as well as on the resulting contraction and expansion of the central regions of the halo. Our conclusions are presented in Section 4.

2.2 Simulations

In this section we give an overview of the EAGLE simulations used in this work and describe the selection of our halo sample.

2.2.1 The code

The EAGLE project (Schaye et al., 2015; Crain et al., 2015) is a suite of hydrodynamical cosmological simulations that follow the formation and evolution of cosmic structure from ΛCDM initial conditions assuming the cosmological parameter values from Planck Collaboration et al. (2014). They were performed using a modified version of the P-Gadget3 code (Springel, 2005) that incorporates subgrid prescriptions for the physics relevant to galaxy formation and evolution: radiative cooling (Wiersma et al., 2009), photoheating, star formation and evolution (Schaye, 2004; Schaye & Dalla Vecchia, 2008), stellar feedback (Dalla Vecchia & Schaye, 2012), black hole seeding (Springel et al., 2005a; Booth & Schaye, 2009), its subsequent growth and stochastic, thermal AGN feedback. The values of the parameters used in modelling these processes were set by requiring a good match to the observed $z = 0.1$ galaxy stellar mass function, the distribution of galaxy sizes and the amplitude of the central black hole mass *vs* stellar mass relation. Once calibrated in this way, EAGLE reproduces a number of population statistics (Schaller et al., 2015; Ludlow et al., 2017).

In this work we use the higher mass resolution version of EAGLE (see Crain et al. 2015 for details), in which the subgrid physics parameters were recalibrated to account for the increased mass resolution. This simulation follows 2×752^3 particles in a volume 25 Mpc on a side. This resolution corresponds to dark matter and gas particle masses of 1.21×10^6 $M_\odot$ and 2.26×10^5 $M_\odot$, respectively. The maximum physical Plummer-equivalent gravitational softening length is 325 parsecs. There are a total of 405 temporal outputs between redshifts $z = 20$ and $z = 0$, corresponding to a time resolution of ∼60 Myrs. This provides adequate time resolution to study the processes of interest in this work.

To identify cosmic structures, we assign particles into distinct groups according to the friends-of-friends (FoF) percolation algorithm (Davis et al., 1985). Each group is made up of particles that are within 0.2 times the mean interparticle separation from one another. Gravitationally bound substructure is found with the SUBFIND algorithm (Springel et al., 2001), which, using particle velocity and position information, identifies self-bound struc-

tures within a larger FoF group. We follow the time evolution of the SUBFIND groups by identifying their main progenitor. This is achieved by cross-matching a subset of the most bound particles between consecutive time outputs.

2.2.2 Sample Selection

Since we are interested in the central parts of dark matter haloes similar to the Milky Way's, we restrict our analysis to haloes of mass M_{200}* at $z = 0$ in the range $0.5 - 2.5 \times 10^{12}$ $M_\odot$. This encompasses recent observational estimates of the Milky Way's halo mass (Callingham et al., 2019; Cautun et al., 2020). A total of 45 haloes satisfying this criterion were identified in the hydrodynamical simulation. Their stellar masses are shown in the top panel of Fig. 2.1. The central galaxies exhibit a wide range of masses; most are more massive than 10^{10} $M_\odot$, but they are typically less massive than the Milky Way. This is because the stellar mass to halo mass relation in EAGLE falls short in the halo mass range of interest, compared to abundance matching results (e.g. Moster et al. 2013). This is related to an underestimate of the galaxy stellar mass function around the knee (Schaye et al., 2015).

Their DMO counterparts were found using the particle ID information for a subset of the most bound particles in the hydrodynamical and DMO simulations. The halo centres were found using the shrinking-spheres algorithm (Power et al., 2003), run only on the dark matter particle distribution.

2.3 Results

We begin with an overview of the central DM mass evolution of the selected halo sample. This is followed by a qualitative assessment at the evolution of four different haloes that illustrate the variety of baryon processes that change their innermost DM and stellar content. Finally, we discuss and characterise each of these processes, namely, an initial halo

*M_{200} is defined as the mass contained within a sphere of mean density 200 times the critical density of the universe.

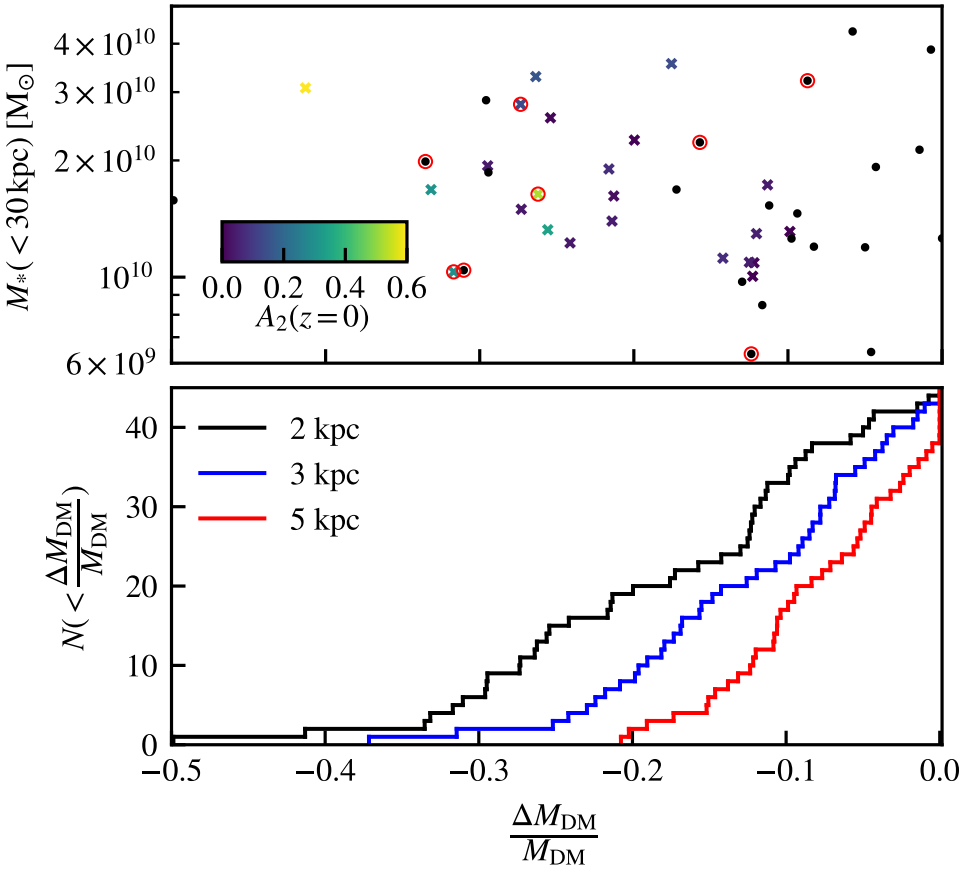

Figure 2.1: The top panel shows the stellar mass of the central galaxies in the selected halo sample, measured within a spherical aperture of 30 kpc, as a function of the fraction of DM mass loss within 2 kpc of the halo centre, $M_{\mathrm{DM}}(z=0)/M_{\mathrm{DM}}(z_{\mathrm{peak}})-1$. The crosses indicate haloes that exhibit a monotonic decrease in mass with time; the dots are the rest of the halo sample. The former are colour-coded according to how prominent their stellar bars are at $z=0$, measured using the method described in §3.3. Galaxies that experienced major AGN outbursts at least once during their evolution are highlighted by the red circles. Despite the mass losses shown here, all the haloes remain contracted relative to their DMO counterparts up to $z=0$. The bottom panel shows the cumulative distribution of the fractional mass loss in the same halo sample, measured within spherical apertures of 2 kpc (black), 3 kpc (blue) and 5 kpc (red). Note that fewer haloes experience a mass loss when considering larger apertures, hence why the y-axis intercept of the bottom panel changes.

contraction due to the accumulation of baryons at the centre, which can then be followed by an expansion caused by AGN-induced gas blowouts, stellar bars or a combination of both.

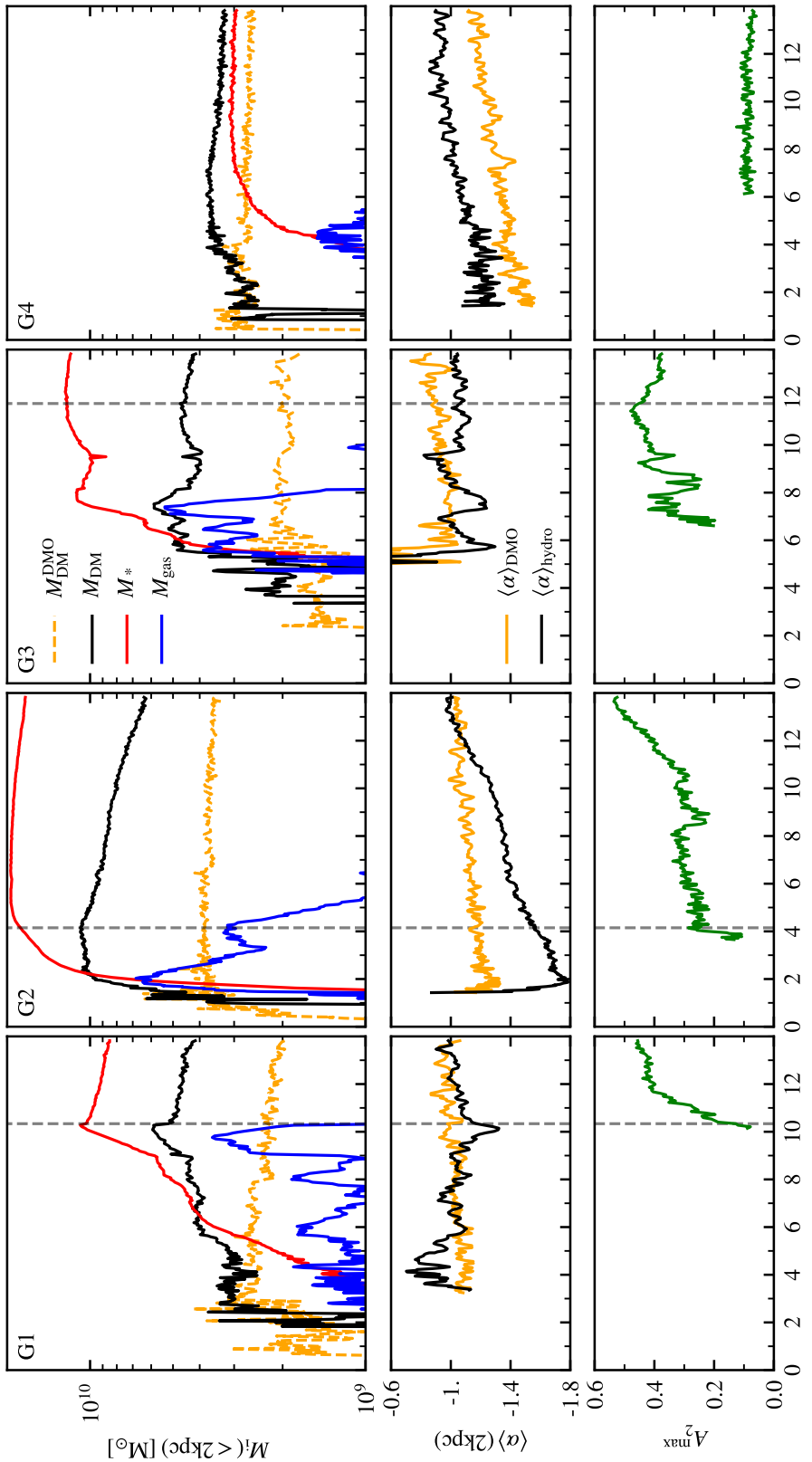

Figure 2.2: Time evolution of the central dark matter, gas and stellar content of four Milky Way mass haloes, together with the evolution of their measured bar strengths. Each column is for a different halo, with the top panels showing the enclosed DM (black), gas (blue) and stellar (red) masses within a 2 kpc spherical aperture. For comparison, the DM mass enclosed within 2 kpc in the DMO counterpart is shown by the dashed orange line. The middle panels show the (smoothed) evolution of the DM density profile slope at 2 kpc, both for the DMO (orange) and hydrodynamical (black) counterparts. The bottom panels show the time evolution of the bar strength of these galaxies. For haloes G1 and G2, this is only shown from times shortly before a visually recognisable bar had formed. Halo G3 had large values of $A_2^{\rm max}$ even before an established bar formed, which happened shortly before the observed peak in enclosed DM mass. Halo G4 never formed a bar, hence the low values of A_2. The vertical dashed lines indicate the times used to determine $M_{\rm DM}(z_{\rm peak})$.

2.3.1 Overview

To determine whether there has been a decrease in the central mass of DM over time, we follow its time evolution within several apertures. The evolution within a 2 kpc aperture is shown for a few examples in Fig. 2.2. We locate the time when the dark matter content peaks and compare it to the present-day value. To this end we define the fractional mass loss as $\Delta M_{\rm DM}/M_{\rm DM} \equiv M_{\rm DM}(z = 0)/M_{\rm DM}(z_{\rm peak}) - 1$. To prevent fluctuations caused by merger events, which can cause the DM mass to fluctuate for a short period of time, we apply a linear Sagvol-Kolmogorov convolution to smooth out the evolution. We only consider peaks that are not immediately followed by a local minimum. This helps prevent transient peaks caused by mergers with other halos, which would otherwise boost the value of $\Delta M_{\rm DM}/M_{\rm DM}$. In practice, this may underestimate the expansion for a subset of haloes, as illustrated by halo G3 in Fig. 2.2 for which the local maximum at $t_{\rm u} \sim 11$ Gyrs is used instead of the global maximum at $t_{\rm u} \sim 7.5$ Gyrs.

The bottom panel of Fig. 2.1 shows the cumulative number of simulated MW-mass haloes that have lost a fractional mass $< f$ within three different spherical apertures: 2 kpc, 3 kpc and 5 kpc. Clearly, the mass loss does not depend on the galaxy stellar mass, as demonstrated in the top panel of the same figure. Although there is a wide range of fractional mass loss values, no halo has lost more than 50% of its peak dark matter mass, even within 2 kpc from the centre. Nonetheless, half of all haloes have lost more than 16% of their peak dark matter mass within 2kpc, with only one reaching the peak at $z = 0$. The DM mass loss decreases when considering larger apertures: half of the haloes considered here lose more than 11% and 7% their peak dark matter mass within 3 kpc and 5 kpc, respectively. Nonetheless, there are still a number of haloes that exhibit a more significant decrease ($\sim 20\%$) of DM mass even at 5 kpc. To investigate the reason behind the expansion, we follow the evolution of the dark matter halo and its associated central baryonic content.

Four representative examples are shown in Fig. 2.2, where the time evolution of the halo dark matter, gas and stellar mass within 2 kpc are shown in the top panels by different

colour lines, as indicated in the legend. These examples are chosen to illustrate the diverse evolution of the mass content that characterises the haloes in our sample. Some exhibit only a secular decrease of DM mass over time (G2); others experience an additional, sudden mass loss event (G1). There are those that remain virtually unaltered throughout their lifetime (G4) and those which have a more complicated assembly history (G3). Their evolution is compared to their DMO counterparts, whose inner dark matter content, $M_{\rm DM}^{\rm DMO} = (1 - f_{\rm b}) M_{\rm tot}^{\rm DMO}$, is shown by the black dashed lines.

In all cases, the relative difference between the enclosed dark matter in the hydrodynamical and DMO versions of the same haloes evolves with time. Their values are similar at large redshifts, but start to diverge once gas and stars populate the inner regions of haloes. This is evidence for the contraction of the halo induced by baryons. By $z = 0$, all the haloes in the hydrodynamical simulation are more massive at the centre than their DMO twins. Nonetheless, it is evident from haloes G1, G2 and G3 that their central DM mass in the hydrodynamical simulation evolves non-monotonically, leading to a decontraction at late times. We measure the slope of the DM density profile by fitting a power law, $\rho \propto r^{\alpha}$, to its central distribution. The time evolution of this quantity is shown in the middle panels of Fig. 2.2. None of the haloes considered here show signs of a significant flattening at $\sim$ 2 kpc, indicating that neither AGN nor bars make cores on these scales in our simulations Moreover, there is very little difference in the slopes between the hydrodynamical and DMO versions of the same halo, despite large differences in the enclosed mass at 2 kpc. The local density slope is not an adequate metric for quantifying how contracted a halo is.

Although the physical mechanisms driving these mass changes will be discussed in detail in the following subsections, we present here a qualitative discussion on the evolution of the haloes shown in Fig. 2.2, which helps understand their relative importance. As shown in the leftmost panel, the central DM and stellar masses of halo G1 peak at $t_{\rm u} \sim 10.3$ Gyrs. This is followed by a sudden of 15% and 5% decrease in DM and stellar mass respectively, and a bar forms immediately after that. The bar is associated with the start of the secular DM and stellar mass loss from the central regions that lasts until the present day. Overall, this constitutes a total loss of 29% (21%) of the peak DM (stellar) mass, with the AGN

responsible for 50% (21%) of this decrease and the stellar bar for the remainder. Halo G3 also experiences a disruptive AGN-driven gas blowout, but contrary to halo G1, its bar forms before the blowout occurs. The only mechanism responsible for the DM loss in the hydrodynamical counterpart of halo G2 is the presence of the stellar bar. Similarly to the previous examples (G1 and G3), the formation of the bar in halo G2 at $t_{\rm u} \sim 4$ Gyrs is associated with the onset of the secular DM and stellar mass loss. Finally, halo G4 never forms a bar nor experiences a major gas blowout, and its inner DM mass remains roughly constant until redshift z=0.

2.3.2 AGN-driven gas blowouts

As we have shown in the previous section, strong gas blowouts caused by AGN activity are able to induce a substantial decrease in the central stellar and DM masses. Haloes G1 and G3 experience such blowouts, as evidenced by the sharp decrease in their enclosed stellar and dark matter masses shown in the top panels of Fig. 2.2. These occur at different times, with the blowout in halo G1 taking place at $t_{\rm u} \sim 10.3$ Gyrs and that in halo G3 at $t_{\rm u} \sim 8$ Gyrs.

In halo G1, we can see a steady decrease of $\sim 50\%$ of the gas mass in the central regions before the proper blowout that removes the remaining gas occurs (see vertical dashed line). This prior decrease is associated with star formation and stellar feedback, which, as we have verified visually, does not disrupt the gas disc. In fact, despite this decrease in gas mass, the gas disc becomes more compact and reaches a surface density comparable to that of the stellar disc just before it is disrupted. This 'compactification' could be caused by the torques exerted by the galaxy that flew by earlier (Blumenthal & Barnes, 2018). Finally, a significant amount of gas mass is fed into the central black hole, triggering an outburst of the AGN that destroys the gas disc and removes virtually all gas from the central regions. A similar process occurs in halo G3, although this galaxy is already strongly barred prior to the AGN-driven blowout event. The bar could provide another mechanism to facilitate the inflow of gas towards the centre of the galaxy (e.g. Sanders & Huntley, 1976; Fanali et al., 2015).

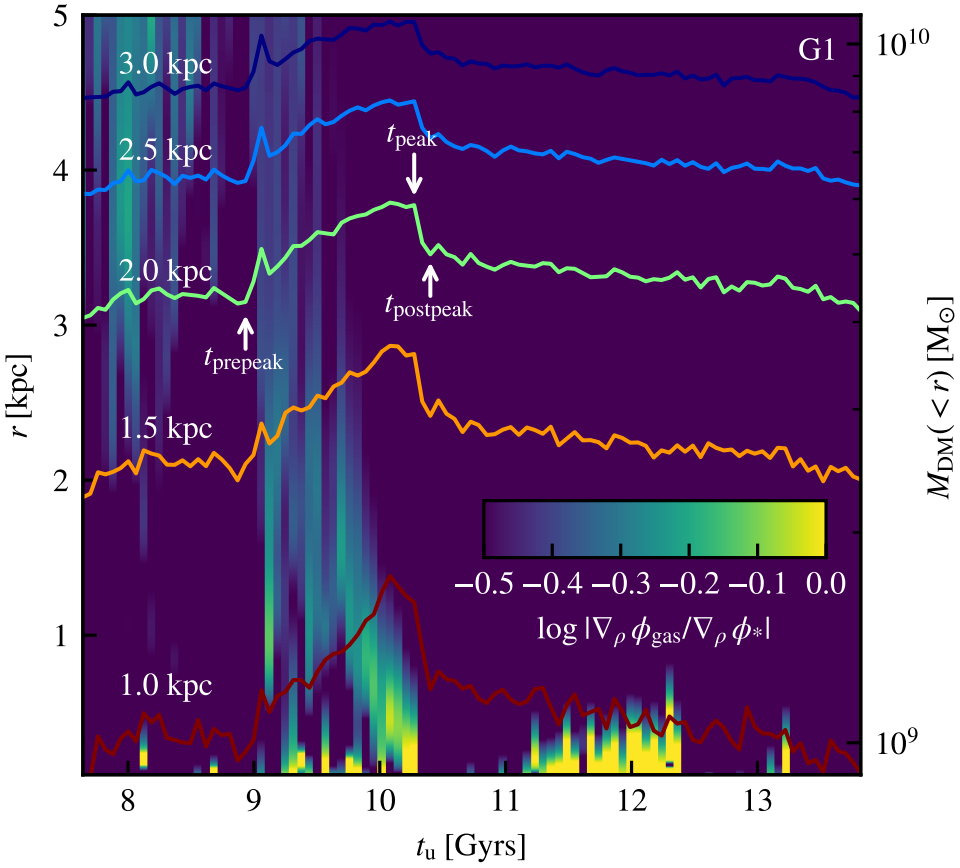

Figure 2.3: The colour scale indicates the ratio between the gravitational accelerations exerted by the gas relative to the stars, $\nabla_\rho \phi_{gas}/\nabla_\rho \phi_*$, along a random azimuthal direction contained within the midplane of the galaxy of halo G1. This is shown as a function of time (x-axis) and distance to the centre of the halo (y-axis). The solid lines show the evolution of the enclosed dark matter mass within spherical apertures ranging from 1 kpc to 3 kpc, in increments of 0.5 kpc, as indicated by the labels on the left hand side.The vertical white arrows indicate the visually determined times used to quantify the contraction and expansion of both the DM halo and the stellar component caused by changes in the gas disc.

A requirement for blowouts to be effective in altering the distribution of dark matter is that gas must be strongly gravitationally coupled to the dark matter prior to the blowouts (Benítez-Llambay et al., 2019). We have checked whether this is the case for halo G1 by comparing the gravitational force exerted by the gas and the stars along a random azimuthal direction contained within the midplane of the galaxy. The leftmost top panel of Fig 2.2 shows that baryons dominate the central regions of halo G1. Therefore, to asses the importance of gas for the gravitational force, we only need to determine the relative contribution between the gas and stellar components. We compute the force by taking

the gradient of the gravitational potential calculated by direct summation over all particles within 30 kpc from the centre of the halo. The choice of azimuthal direction has little effect on the estimated forces during the time of interest, given that there is no prominent non-axisymmetric feature prior to the blowout.

Fig. 2.3 shows the temporal evolution of the gravitational force exerted by the gas, relative to that of the stars, as a function of the distance to the centre. Focusing on the times prior to the blowout (9 Gyrs $\leq t_{\rm u} \leq$ 10.3 Gyrs), the gas makes a contribution similar to the stars in the innermost regions. This is not the case for most of the evolution at late times since there is very little gas left after the blowout. Initially, the gravitational contribution of the gas disc is significant (but not dominant) throughout the central 5 kpc of the halo. The gas becomes increasingly gravitationally important in the central regions over time. As mentioned before, this is due to the fact that the gas disc becomes more compact during this time. Just before the blowout occurs, the density of the gas disc and the enclosed dark matter and stellar masses peak, which indicates that the baryonic blowout is responsible for the accompanying mass loss in all the components.

We have explicitly checked that the large-scale winds are driven by AGN. Three images of the gas content of the galaxy before, during and after the outburst are shown in Fig. 2.4. Prior to the start of the event, most gas is concentrated in the centre of the halo, where the black hole resides. It has a net negative average radial velocity, corresponding to inflow that is manifest in the compactification of the gas component observed in Fig. 2.3. Once the outburst commences, most gas is quickly evacuated from the centre in just ∼120 Myrs, with outflow velocities that are in excess of 100 km s^{-1} during the later stages.

Although the gas disc is gravitationally dominant only in the very central regions prior to being blown out, the sudden gas blowout has a measurable effect even at radii several times larger, well beyond where the gravitational contribution of the gas is significant. The solid lines in Fig. 2.3 show the evolution in time of the enclosed DM mass within apertures ranging from 1 to 3 kpc. Although the decrease in DM mass is larger at smaller radii, where the gravitationally coupling between the dark matter and the gas was larger, it is still detectable at larger radii. This also underlines the importance of the timescale over which

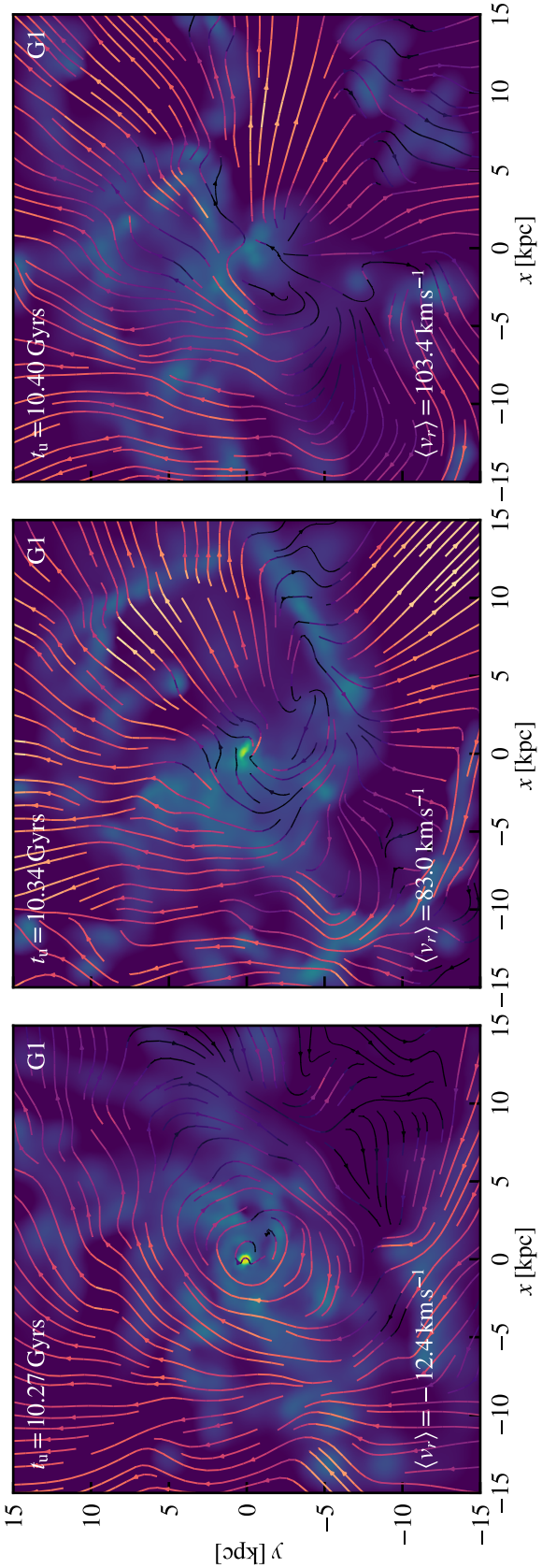

Figure 2.4: Surface density (colour scale) of the face-on gas content of halo G1, with each panel from left to right showing its distribution before, during and after the AGN outburst, respectively. Streamlines indicate the gas velocity with a colour intensity that is proportional to its magnitude. The average radial velocity of gas within a sphere of 30 kpc from the centre of halo G1 is shown in the lower left corner. The times at which the galaxy was imaged are indicated in the top left corners of each panel.

gravitational perturbations act. The long timescale that it takes for the perturbation to grow ensures that the removal of the gas causes a maximal effect at larger distances from the centre.

To understand why this is the case, consider a system in which all particles are on circular orbits. When a central perturbation is exerted, the orbits of particles become elliptical and are able to come closer to the centre (contraction). When the perturbation is removed, particles that have descended down the perturbed potential well will have gained energy, allowing them to reach radii further beyond their original radius (expansion). Evidently, the picture is more nuanced in a more realistic scenario in which particles are not necessarily on circular orbits nor in the same orbital phase. Nonetheless, this example helps illustrate the consequences of such perturbations.

Our interpretation implies that the degree of initial contraction and subsequent expansion must be related: a shell that responds strongly to the addition of a perturbation will initially contract and subsequently expand more than one with a weaker response. Thus, the amplitude of the expansion will, in part, be determined by how strong the initial contraction was. Secondly, the timescale of the perturbation determines its effectiveness in altering the kinematics of a radial shell: if the duration of the perturbation is short compared to the dynamical timescale of a given radial shell, particles do not have enough time to deviate significantly from their original orbits and change their energy. On the other hand, if the timescale is sufficiently long, its effect becomes maximal.

To illustrate this we investigate whether there is a correlation between the expansion and contraction of different radial shells of halo G1, as well as the dependence of their amplitude with distance from the centre of the halo. We identify the times at which the gravitational perturbation sourced by the gas disc starts ($t_{\rm prepeak}$) and ends ($t_{\rm postpeak}$). We can thus measure the enclosed masses at these times relative to the time when they peaked ($t_{\rm peak}$), and thus estimate the degree of contraction and expansion of each shell. Although identifying $t_{\rm peak}$ and $t_{\rm postpeak}$ is straightforward, locating the time at which the perturbation starts is less so. By visually inspecting the evolution of the enclosed masses of DM (Fig. 2.3), we can estimate the time at which the halo starts contracting ($t_{\rm u} \sim 9$Gyrs). This coincides with the

time when gas was being delivered to the central regions.

Once these times have been measured, the degree of expansion and contraction of each shell is estimated by taking the ratio of enclosed masses at different apertures, ranging from 1 to 20 kpc. This is shown in Fig. 2.5, which demonstrates that the degree of expansion is indeed related to the degree of contraction, as expected from our previous arguments. Furthermore, the amplitude increases towards the centre of the halo, with the DM component losing $\sim 25\%$ and $\sim 10\%$ within 1 and 3 kpc respectively. Similarly, the expansion of the stellar component correlates well with the degree of contraction, although in a different manner compared to the DM component. Also worth noting is the offset from unity along the x-axis, likely caused by the growth of both the halo and the galaxy. This is a consequence of our definition of the degree of contraction, which includes the *total* mass increase. Their relative offset is explained by the fact that the galaxy grows more than the DM halo during the timescale under consideration. Finally, differences between the dynamical properties of the DM and stars might affect the degree of contraction caused by the gas, since circular orbits respond more strongly.

To ascertain how common AGN-fueled blowouts are, we inspect the mass evolution of the gas, DM and stars within 2 kpc from the centre of all MW-mass haloes. We then identify the times when the galaxy loses a large amount of gas in a short timescale (less than 100 Myrs, which corresponds to the time resolution of our data outputs) and inspect whether there is an associated decrease in the stellar and DM masses. To rule out a localised blowout that is not sufficiently strong to disrupt the gas disc, the gas content within 5 kpc should have also significantly decreased. Seven haloes out of the 45 studied here show definite evidence supporting that they experience such events at least once during their lifetime, with two others showing strong hints that they did. This comprises roughly 15% to 20% of the sample studied here, with the rest not experiencing such an event or having a complicated evolution that prevents us from making a definite statement on whether they have experienced one or not.

These findings are applicable to the real universe as long as strong AGN outbursts are able to completely remove the central gas content of galaxies. The parameters modulating

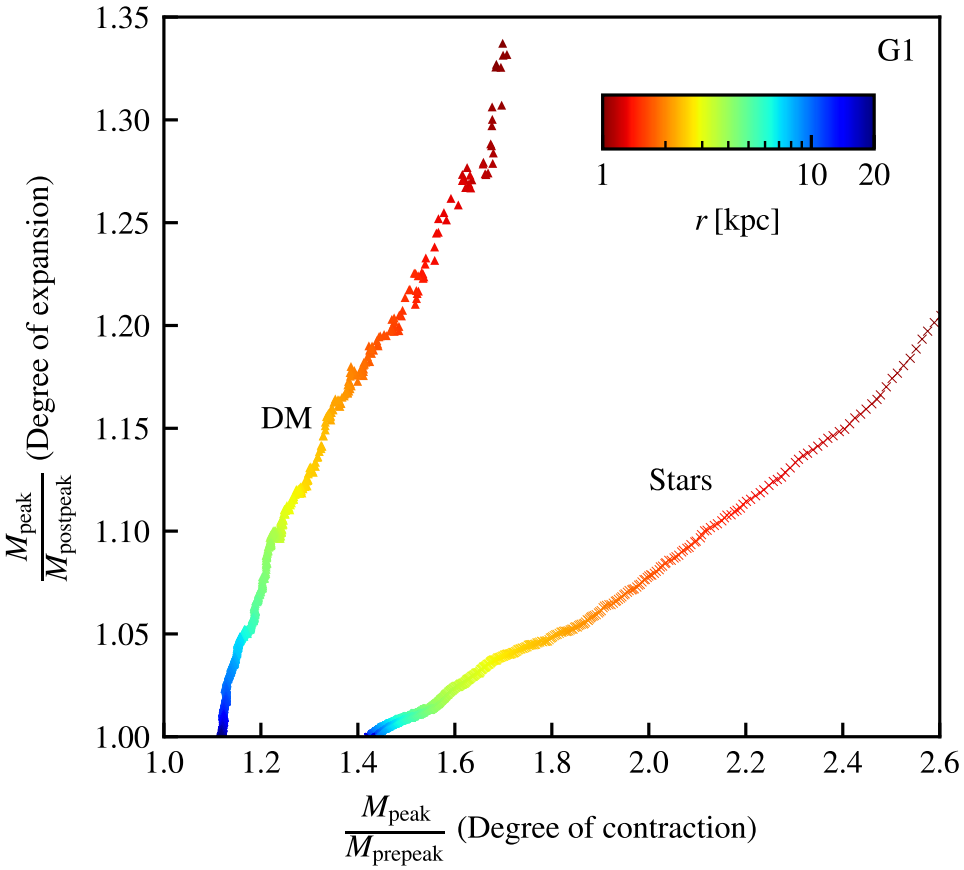

Figure 2.5: Degree of expansion (vertical axis) as a function of degree of contraction (horizontal axis), for different radial shells in the radius range, $1.0 \leq r/\mathrm{kpc} \leq 20.0$, for halo G1. We estimate the quantities by identifying the time at which the dark matter peaks and measure the mass prior to the peak, $M_{\rm prepeak}$ ($t_{\rm u} \sim 9$Gyr), and after the peak, $M_{\rm postpeak}$ ($t_{\rm u} \sim 10.3$Gyr). These times are indicated in Fig. 2.3. The colour of each marker indicates the value of the spherical aperture.

their efficiency in EAGLE were calibrated by requiring that the model should reproduce a number of population statistics and scaling relations. Nonetheless, this is not the only prescription that meets these requirements. An example is the IllustrisTNG model, which includes a kinetic feedback mode at low mass accretion rates instead of the purely thermal implementation used in EAGLE. These modelling differences lead to different predictions for poorly constrained relations, such as how gas-rich the circumgalactic medium is as a function of halo mass below $\sim 10^{12}$ $\mathrm{M}_{\odot}$ (Kelly et al., 2021; Davies et al., 2020). This suggests the EAGLE AGN model is more effective at removing baryons on the MW mass scale than other similarly realistic simulations. It would be interesting to examine whether AGN outbursts similar to the ones discussed above are also present in other simulations

using different ways to model AGN feedback.

2.3.3 Stellar bars

In a number of Milky Way mass halos we observe a decrease in the central mass of dark matter and stars taking place over several Gyrs, as opposed to the AGN-induced gas blowouts, which correspond to Myrs timescales. This decrease occurs in haloes whose central regions are dominated by stars, with the largest decreases associated to strongly barred galaxies. The top panels of Fig. 2.2 show three such examples. Halos G1 and G2 have a global maximum in the enclosed DM mass followed by a monotonic decrease such that by $z = 0$, they have lost $\sim 20\%$ and $\sim 40\%$ of the peak DM mass within 2 kpc respectively. This number excludes the initial, blowout-induced mass decrease observed in halo G1. By contrast, halo G3 shows a non-monotonic evolution of the central mass of DM and stars. This reflects the nature of its past evolutionary history, which is much more turbulent than for haloes G1 and G2. In contrast to these, which remained relatively undisturbed once the peak mass had been reached, halo G3 underwent several mergers and flybys by surrounding galaxies.

The development of a stellar bar in our simulations is associated with the outward transfer of stellar and DM mass. The evolution of bars is driven by the exchange of angular momentum with the surrounding components of the system (Athanassoula, 2003). To measure the strength of the bar, we first orient the galaxy so that it is viewed face-on. This is achieved by aligning the spin of the stellar component, computed by measuring the total angular momentum of all stars within 5 kpc from the centre, along the z-axis. The galaxy is then split into several concentric cylindrical annuli of 4 kpc in height and of variable width, such that each encloses 500 stellar particles. This choice provides better spatial resolution than bins of constant width in the barred regions, which contain more stellar particles than the outer regions. For each bin we measure the strength of the quadrupole moment of the azimuthal distribution of stellar particles, relative to their monopole strength:

$$A_2 \equiv \frac{\sqrt{a_2^2 + b_2^2}}{a_0}\,, \tag{2.2}$$

where:

$$a_m = \sum_i^N M_i \cos m\phi_i \,, \tag{2.3}$$

$$b_m = \sum_i^N M_i \sin m\phi_i \,. \tag{2.4}$$

The sums are taken over all stellar particles in the bin, with M_i and ϕ_i their masses and azimuthal angles, respectively. Additionally, we also measure the quadrupole moment phase angle via $\phi_2 = 0.5 \arctan(b_2/a_2)$.

Finally, a Savitzky-Golay filter is used to smooth the radial variation of $A_2(r)$, with the length of the smoothing window set to 5% of the total number of annuli. The right panels of Fig. 2.6 show the $A_2(r)$ profile and the quadrupole moment phase angle for halo G2 at $z = 0$. The former has a prominent peak within 4 kpc associated with the presence of a strong bar, which shows a consistent orientation out to 4 kpc. We use the peak value, $A_2^{\max}$, to estimate the strength of the bar for each galaxy as a function of time. In this work we use a threshold of $A_2^{\max} = 0.15$ to estimate when a bar forms, with the choice behind this value being strictly operational. Given that features and artifacts not related to bars can also boost the quadrupole moment in complicated cosmological simulations such as this one, we visually inspect the stellar distribution of galaxies with $A_2^{\max} \geq 0.15$ to confirm the presence of a bar.

Two other important properties of the bar are its length and pattern speed. To measure the length, we employ the definition adopted by Algorry et al. (2017): the radius at which $A_2(r)$ first drops below 0.15 after it has reached $A_2^{\max}$. The dashed black circle in the left panel of Fig. 2.6 shows the extent of the bar determined in this way.

We measure the bar pattern speed directly by computing the change in the orientation of the bar between consecutive temporal outputs, i.e. $\Omega_p = \Delta\theta_p/\Delta t$. The angle of the bar, θ_p, is measured from the phase of the quadrupole moment at the radius where $A_2(r)$ peaks.

The bottom panels of Fig. 2.2 show the time evolution of the strength of the stellar bars in the galaxies illustrated on the top panels. The bars in both halo G1 and G2 form at around the time when the central DM mass begins to decrease. Once formed, the bars

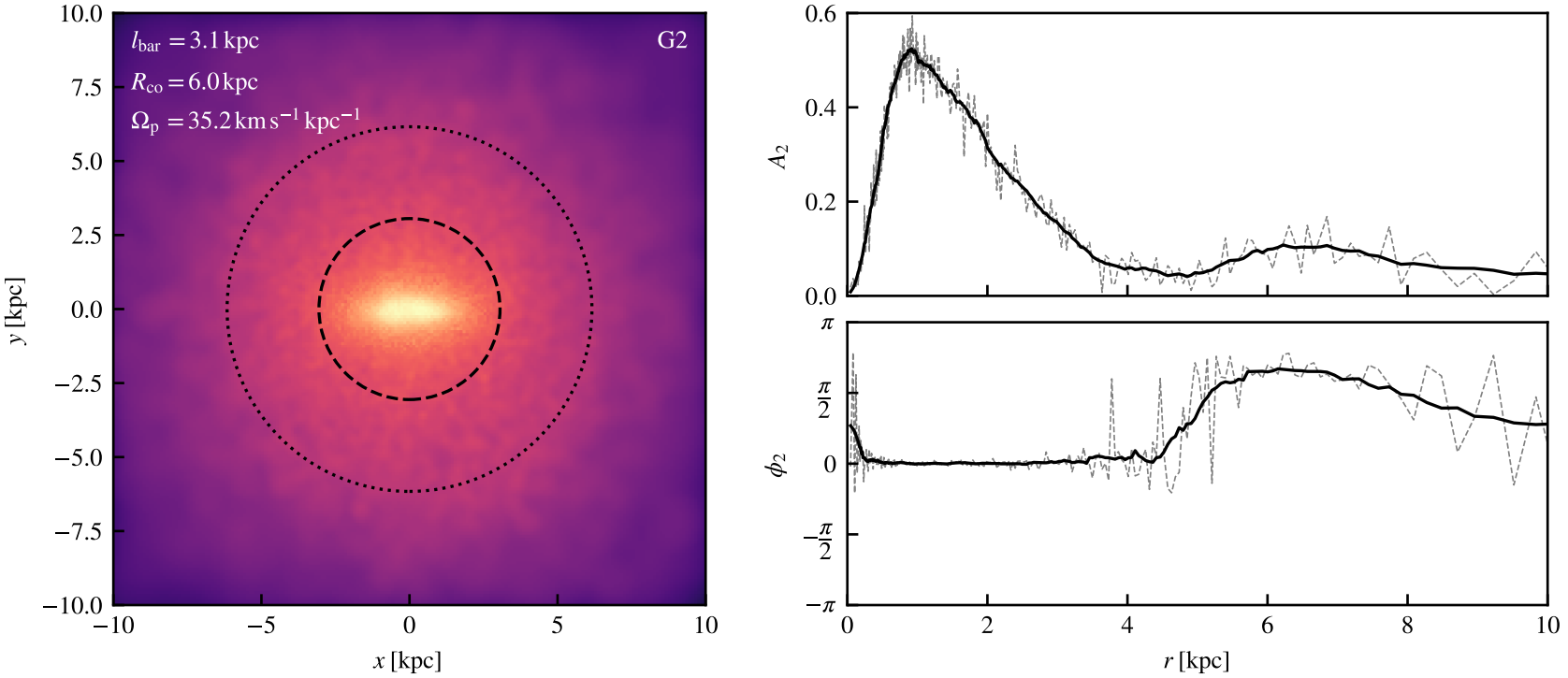

Figure 2.6: *Left panel*: logarithmic surface density (colour scale) of the face-on view of the stellar component of halo G2. The face-on orientation is chosen such that the bar is aligned along the x-axis. The values of the surface density range from $10^{10}\,{\rm M_\odot\,kpc^{-2}}$ to $10^{5}\,{\rm M_\odot\,kpc^{-2}}$. The values of the bar length, pattern speed and corotation radius are shown in the top left corner. Its extent and corotation radius are also indicated by the dashed and dotted circles, respectively. *Top right panel*: radial variation of the $A_2(r)$ metric for halo G2 at $z = 0$. We use the peak value to characterize the strength of the bar. The dashed lines show the raw values obtained using cylindrical annuli 4 kpc in height, each enclosing 500 stellar particles. These values are smoothed using a Savitzky-Golay filter (black solid line). *Bottom right panel*: Same as the panel above, but for the quadrupole moment phase angle.

generally increase in strength monotonically. The evolutionary story of halo G3 is less trivial and the bar goes through periods of strengthening and weakening. At early times ($t_u \leq 7 - 7.5$ Gyrs), the value of A_2 is large but in spite of this, we do not visually recognise a bar. The large value of A_2 is caused by mergers occurring along the line-of-sight, and by the fact that the centre becomes ill-defined during this period. The end result is that the projected stellar distribution exhibits a large quadrupole moment. Additionally, transient elongations of the stellar distribution influence the values of $A_2^{\rm max}$, as seen in the variations of its value in the bottom panel of Fig. 2.2. The newly formed bar weakened significantly probably as a result of the rapid increase in the density of the central gas that preceded the AGN blowout. Interestingly, most of this gas was distributed along a bar-like feature aligned with the stellar bar. After increasing in strength again, there is an additional weakening episode that is likely caused by a merger event (Ghosh et al., 2021). In all three cases, the bars have significantly slowed down by $z = 0$, with the ratio of corotation radius to bar length equal to 2.1, 1.9 and 2.0 respectively.

For halos G1 and G2 the secular decrease in the central DM mass is clearly associated with the formation and subsequent evolution of the bar. Nonetheless, even though both have strong bars of similar strengths at $z = 0$, each lost different amounts of mass from the central regions. This is due to the fact that the bars formed at different times and evolved by different amounts. To investigate further the connection between the decrease in central DM mass and the prominence of the stellar bar, the age of the bar should be taken into account. The metric we use is the average mass loss rate between $z_{\rm peak}$ and $z = 0$, normalised by the peak DM mass within 2 kpc. We consider only those examples that exhibit a monotonic decrease in the central DM mass, e.g. haloes G1 and G2, but not G3. This selection was done by visually inspecting the central mass evolution of all the MW mass haloes in the simulation. Twenty-three out of the initial 45 haloes satisfy this criterion, which preferentially selects galaxies that have undergone relatively undisturbed evolution after the peak in central DM mass was reached. Finally, we exclude sudden DM mass decreases associated with the gas blowouts discussed in the previous section, since here we are interested in the bar-driven secular decrease.

Fig. 2.7 shows the variation of the average fractional mass loss rate between $z_{\rm peak}$ and $z = 0$ of each monotonically expanding halo as a function of their time-averaged bar strength, $\langle A_2^{\rm max} \rangle$*. This value was computed by averaging $A_2^{\rm max}$ from the time at which the enclosed DM peaked up to $z = 0$. The horizontal error bars indicate the variation of $A_2^{\rm max}(t)$, with low values corresponding to galaxies whose quadrupole moment strength remained relatively unchanged (e.g. if the stellar disc was axisymmetric throughout the simulation or the bar did not weaken or strengthen). We further classify galaxies into barred or unbarred depending on whether they had a value of $A_2^{\rm max}$ greater than 0.15 during at least 1 Gyrs. This ensures that even galaxies that were barred in the past but are not at $z = 0$ are correctly identified, whilst excluding high, transient values of $A_2^{\rm max}$.

Broadly speaking, Fig. 2.7 suggests that the stronger the time-averaged bar strength of a galaxy is, the greater its secular DM mass loss rate. To quantify this, we calculate Pearson's correlation coefficient $\mathcal{R}$ between $\langle A_2^{\rm max} \rangle$ and the (average) fractional mass loss rate for both populations. The median value for the barred sample is $\mathcal{R} = -0.7^{+0.2}_{-0.2}$, giving support to our previous claim. On the other hand, the unbarred sample has a median of $\mathcal{R} = 0.2^{+0.3}_{-0.3}$, which is consistent with no correlation. It is worth noting that the strongest correlation is found between how much the bar evolved over time and the time-averaged fractional mass loss rate. The correlation coefficient between these two variables is $\mathcal{R} = -0.83 \pm 0.07$. The quoted uncertainties were obtained using a bootstrap technique.

Fig. 2.7 shows several other interesting features. Firstly, a number of haloes with very low values of $\langle A_2^{\rm max} \rangle$ have a wide range of mass loss rates. These galaxies were never barred, and thus the expansion could not have been caused by a bar. We find that these galaxies were gas rich in the past, which caused the haloes to contract. As time progressed, star formation locked some of baryons in stars but the resulting supernovae feedback expelled gas from the central regions. As a result, the overall baryon mass decreased over time, leading to a slightly less contracted halo at later times. This reduction in the central baryon content takes place on much longer timescales than the AGN phase. Secondly, the

*The reason behind using the average bar strength instead of the $z = 0$ strength is that some of the galaxies had (weak) bars in the past that later dissolved.

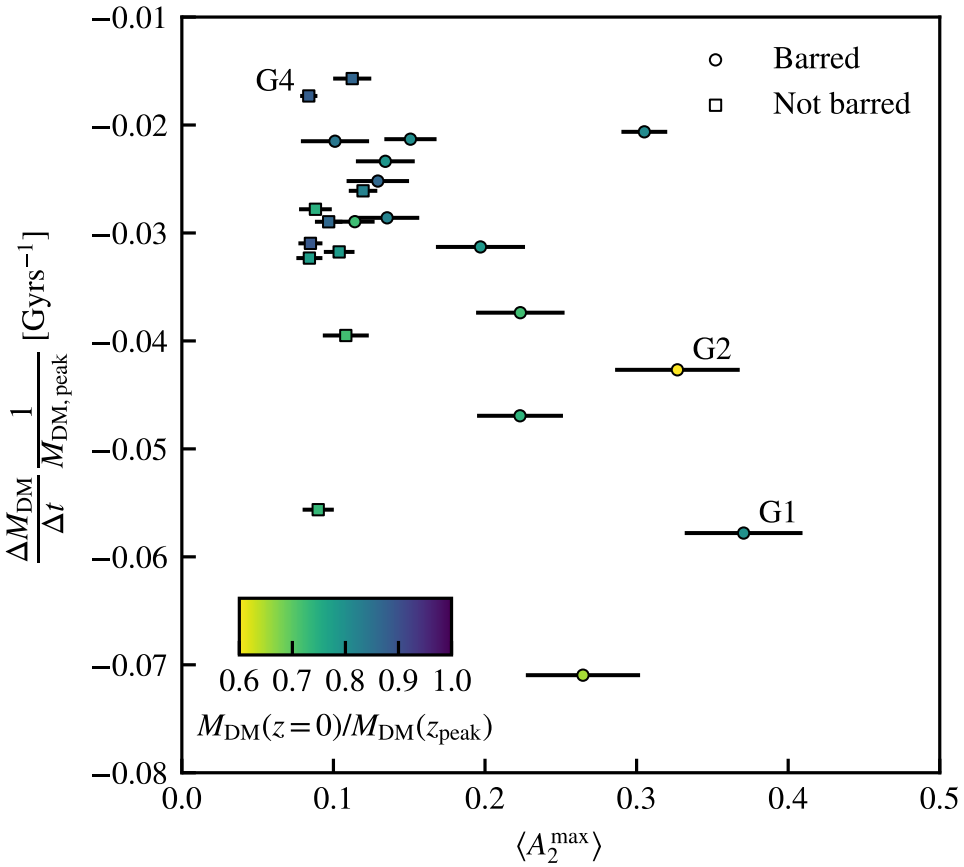

Figure 2.7: The time-averaged fractional mass loss rate of haloes that exhibit a monotonically decreasing central DM mass as a function of their average bar strength. The average bar strength is computed from $z = 0$ until the time when the enclosed dark matter peaks. The circles show galaxies that have values of $A_2^{\rm max} \geq 0.15$ for longer than 1 Gyrs. These are assigned to the sample of barred galaxies. Galaxies that do not satisfy this criterion are assigned to the unbarred population. The horizontal error bars show the spread in values of $A_2^{\rm max}(t)$ for each galaxy since $t_{\rm peak}$, and indicate how much the quadrupole moment strength has evolved since then. Finally, each dot is coloured according to present-day to peak mass ratio, as indicated in the legend.

moderately barred galaxy above the G2 data point has a very low central mass loss rate given its bar strength. As indicated by the horizontal error bars, there was very little change in $A_2^{\rm max}$ which remained roughly constant at $A_2^{\rm max} \sim 0.3$ since its formation. This hints at the need for evolution in the strength of a bar for effective transfer of central DM mass outwards. Finally, to reiterate the importance of the timescale over which the stellar bar acts, halo G1 experienced a greater mass loss rate than halo G2 but lost less central DM mass. This is because G1 had a bar for ~ 4 Gyrs, whereas G2 had it for ~ 10 Gyrs.

Finally, many of the barred galaxies considered here also exhibit a decrease in the central

mass of stars, although to a lesser extent than their DM content. This is observed in all three barred examples shown in the top panels of Fig. 2.2. The presence of a bar is expected to not only affect the dark matter, but also the stellar distribution. Whether particles near resonances are able to emit or absorb angular momentum is dependent on their dynamical properties. Spheroid components such as a dark matter halo or a stellar bulge are net absorbers of angular momentum, so one might expect the stellar bulge to be similarly affected. We have checked whether this is the case for halo G2 by classifying its $z = 2$ stars into bulge and disc components based on their circularities, $\epsilon_{\rm circ} \equiv j_{\rm z}/j_{\rm z,circ}(E)$. By tracking a subset of the most bound particles of each component, we found that the stellar mass loss within 2 kpc is dominated by expansion of the stellar bulge. The net effect is in line with the 'smoothing' effect that non-axisymmetric features have on the rotation and mass distribution curves of disc galaxies (Berrier & Sellwood, 2015). Indeed, the rotation curves of these galaxies are strongly peaked at small radii when the bar initially formed but are less so as time progresses.

These findings are in qualitative agreement with those of Algorry et al. (2017), although there are differences between these studies. Firstly, we analyse a higher resolution version of the EAGLE simulation, with an increase of almost one order of magnitude in the particle mass resolution. This allows us to study the evolution of the inner regions of haloes more confidently. On the other hand, the smaller volume reduces the number of barred galaxies that we can study. Nonetheless, we are able to have a more detailed look at the evolution of the central regions of these haloes. This reveals the importance of the age of the bar, which is primarily determined by the assembly history of its halo. Even for galaxies with similar bar strength at $z = 0$, substantial differences in formation time alter how much the halo de-contracts. Moreover, we also note that the expansion of the dark matter halo is often accompanied by an expansion of the stellar component. Lastly, Algorry et al. (2017) used a stellar mass criterion to select their sample, whereas we select ours based on the virial mass of the dark matter halo. In practice, this results in the stellar component of the haloes in our study being less massive than those in Algorry et al. (2017). This follows from the fact that in EAGLE the stellar mass function is underestimated (Schaye et al., 2015), so

one has to consider more massive haloes to find sufficiently massive galaxies.

2.3.4 Halo contraction

All the haloes considered in this study end up having a higher central density compared to their DMO counterparts. This is a consequence of the accumulation of baryonic mass resulting from the dissipational collapse of gas during the assembly of the galaxy, the so-called 'adiabatic contraction' (Barnes & White, 1984; Blumenthal et al., 1986; Cautun et al., 2020). This trend is opposed by the processes we have discussed here which reduce the central DM density. We now consider how the bar-driven secular evolution of a galaxy alters the degree of contraction of its host halo, bearing in mind that the degree of contraction depends on the halo assembly history (Abadi et al., 2010).

An illustrative example is halo G2, which had the strongest and longest-lived bar in our sample. This galaxy formed 50% of its stars by $z = 2.6$ and was left largely undisturbed for a large fraction of the age of the universe. Changes to its density profile are solely driven by internal, secular processes such as the influence of its stellar bar. To estimate how contracted the halo is relative to its DM counterpart, we follow the procedure described by Abadi et al. (2010). Firstly, we define a shell of radius, R_i, in the DMO simulation that encloses a given amount of dark matter, rescaling the particle masses: $M_\mathrm{DM}^\mathrm{DMO}(< R_\mathrm{i}) = (1-f_\mathrm{b})M_\mathrm{tot}^\mathrm{DMO}(< R_\mathrm{i})$. We then find the corresponding radius, R_f, in the hydrodynamical simulation that encloses the same amount of dark matter, i.e. $M_\mathrm{DM}^\mathrm{hydro}(< R_\mathrm{f}) = M_\mathrm{DM}^\mathrm{DMO}(< R_\mathrm{i})$. In practice, this amounts to enclosing equal numbers of DM particles for each shell. Once these two radii have been found, we measure the total enclosed masses, $M_\mathrm{tot} = M_\mathrm{DM} + M_\mathrm{b}$, for each, where M_b is the mass of baryons. The ratio $R_\mathrm{f}/R_\mathrm{i}$ measures the degree of contraction ($R_\mathrm{f}/R_\mathrm{i} < 1$) or expansion ($R_\mathrm{f}/R_\mathrm{i} > 1$) of a radial shell as a function of the increase ($M_\mathrm{tot}^\mathrm{i}/M_\mathrm{tot}^\mathrm{f} < 1$) or decrease ($M_\mathrm{tot}^\mathrm{i}/M_\mathrm{tot}^\mathrm{f} > 1$) of total mass contained within it. This allows a straightforward comparison to the predictions of the simple adiabatic contraction model, for which $R_\mathrm{i}M_\mathrm{tot}^\mathrm{i} = R_\mathrm{f}M_\mathrm{tot}^\mathrm{f}$.

Fig. 2.8 shows how these ratios vary as a function of time for halo G2, as well as for an

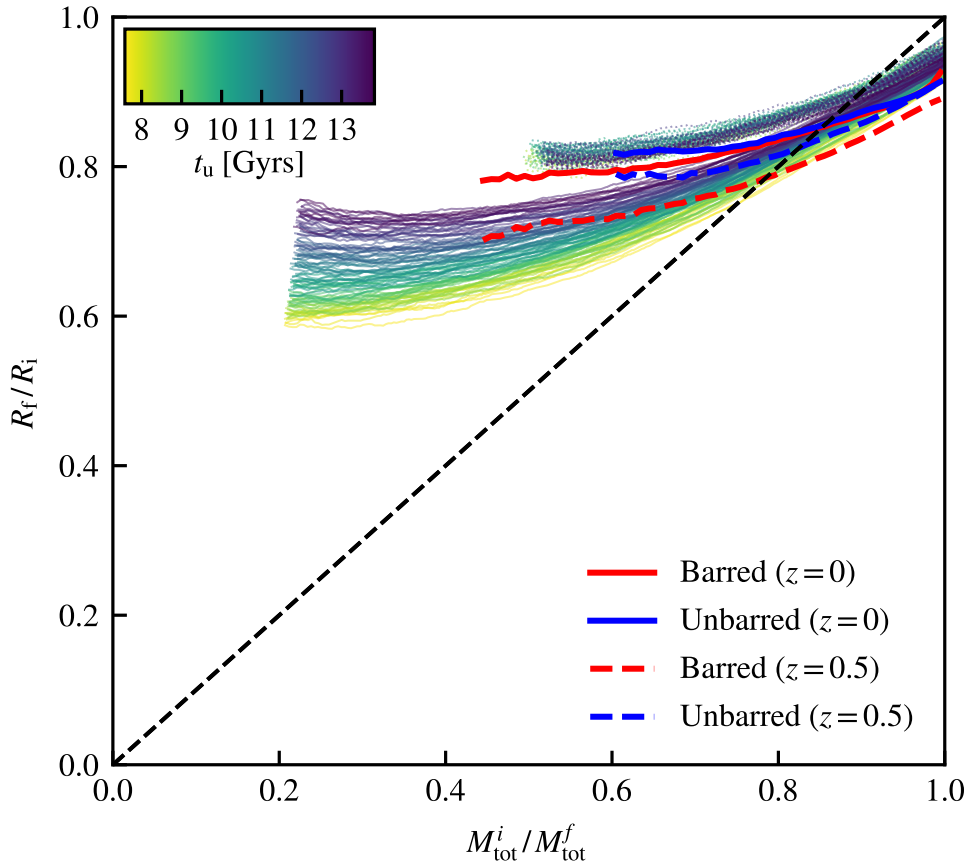

Figure 2.8: Response of the dark matter halo to the assembly of the galaxy at its centre. The ratio R_f/R_i is shown as a function of the change in enclosed total mass $M^{\rm i}_{\rm tot}/M^{\rm f}_{\rm tot}$ at several times for halo G2 (solid coloured lines) and a halo hosting an unbarred galaxy (similar to G4; dotted coloured lines). The values are only shown for radial shells with radii larger than the convergence radius defined by (Power et al., 2003), which is different for each halo. For a consistent comparison, we show only values measured at $t_{\rm u} \geq 7.5$Gyrs. The solid and dashed lines show the $z = 0$ and $z = 0.5$ average values for the barred (red) and unbarred (blue) sample of haloes shown in Fig. 2.7, respectively. The average only includes haloes that are relaxed. We do not show the average value for $M^{\rm i}_{\rm tot}/M^{\rm f}_{\rm tot} \leq 0.45$ (0.60) because only a small number of haloes hosting barred (unbarred) galaxies reach these low values. The diagonal dashed line shows the prediction of the adiabatic contraction model.

unbarred galaxy with a very small reduction in its central DM content. The values are only shown for shells with radii larger than the Power et al. (2003) convergence radius of the DMO halo, with each shell containing 100 more DM particles than the previous one. For consistency when comparing the evolution between the chosen haloes, only the last ~ 6 Gyrs of the simulation outputs are shown. Consequently, the evolution of halo G2 is larger than shown in here, since its expansion began at $t_{\rm u} \sim 4$ Gyrs. Nonetheless, it is evident that its contraction evolves strongly with time. This is in contrast to the unbarred

halo, which remains virtually unchanged over the plotted time period.

As discussed in other studies (e.g. Abadi et al., 2010; Cautun et al., 2020), the adiabatic contraction model overestimates the degree of contraction in the central regions. We find that it also underpredicts it at larger radii as a result of baryonic outflows. Consider a radial shell at the virial radius of the halo, R_{200}. At such large distances, contraction should be negligible and thus $R_{\rm f}/R_{\rm i} \sim 1$. Under the assumption of no DM shell mixing, the values of $M_{\rm tot}^{\rm DMO}(< R_{\rm i})$ and $M_{\rm tot}^{\rm hydro}(< R_{\rm f})$ only depend on the enclosed baryonic mass. For the collisionless case, this is simply $M_{\rm b}^{\rm DMO}(< R_{\rm i}) = f_{\rm b} M_{\rm tot}^{\rm DMO}(< R_{\rm i})$. However, if feedback expels baryons beyond the virial radius, then the baryon fraction at such a distance is less than the cosmic baryon fraction. In other words, $M_{\rm b}^{\rm DMO}(< R_{\rm i}) \geq M_{\rm b}^{\rm hydro}(< R_{\rm f})$ and thus $M_{\rm tot}^{\rm DMO}(< R_{\rm i})/M_{\rm tot}^{\rm hydro}(< R_{\rm f}) \geq 1$. Evidently, this is violated if there is a reduction in the enclosed DM mass at a fixed physical aperture caused by the reduced growth of the halo associated with the loss of baryons at early times, as discussed by Sawala et al. (2013). However, this is not the case for MW-mass halos in the EAGLE simulations (Schaller et al., 2015).

Focusing on the sample of monotonically expanding haloes, Fig. 2.8 also shows how the average values of the two ratios plotted change between $z = 0.5$ (red) and $z = 0$ (black). When computing the averages, only relaxed halos are included. To identify relaxed halos we adopt the most restrictive condition proposed by Neto et al. (2007): the centre of mass should be offset from the centre of potential by less than $0.07 R_{\rm vir}$. We only show the averages for $M_{\rm tot}^{\rm i}/M_{\rm tot}^{\rm f} \geq 0.45$ (0.60) for the barred (unbarred) sample, since very few haloes reach smaller values. The barred sample is, on average, more contracted than the unbarred one as a consequence of their more massive stellar components. The average contraction of each population has decreased over time; the evolution of the unbarred sample is less than that of the barred one.

The systematic shift in the average contraction of the haloes in our sample is due to the secular processes discussed earlier. Since one of the driving effects is stellar bars, which transfer angular momentum from the stars to the dark matter particles, this process could lead to different dark matter particle distribution functions in halos whose central

galaxies have a bar compared to those which do not. These differences may be relevant for distribution function-based models of halo contraction (e.g. Callingham et al. 2020).

Finally, there is considerable halo-to-halo scatter introduced by several factors such as the mass of the central galaxy, the assembly history, the orbital distribution of DM particles, etc. Among these, AGN-driven blowouts could also play a role due to their stochastic nature. Given the small size of our halo sample, we can only note this trend which needs to be confirmed by larger simulations.

2.4 Discussion and conclusions

In this work we have studied the evolution of the central distribution of dark matter in simulated Milk Way mass halos, drawn from a ΛCDM cosmological hydrodynamics simulation. Specifically, we have investigated how the mass within the inner 2 - 5 kpc is affected by processes associated with the growth of the central galaxy in the halo. We analysed 45 haloes taken from the high resolution version of the EAGLE simulation, selected by requiring that their final mass, M_{200}, be similar to that of the Milky Way at $z = 0$.

As in previous studies, we find that, at the present day, the halos are more centrally concentrated than their counterparts in a DMO simulation. However, the degree of contraction is significantly less than expected in the simple adiabatic contraction model (Blumenthal et al., 1986), as well as the refinement of Gnedin et al. (2004), which relaxes the assumption of spherical orbits. Although not explicitly shown here, it follows the same asymptotic behaviour of Blumenthal et al. (1986) in the outskirts of haloes ($M^i_{tot}/M^f_{tot} \sim 1$), predicting an expansion of the halo in the hydrodynamical case to account for the expulsion of baryons from the virial region. As discussed in the previous section, this is not observed in these simulations, which remain largely unchanged near the virial radius despite the loss of enclosed baryonic mass. Near the region where the influence of the stellar component becomes important, it has been shown to under predict the value of R_f/R_i compared to what we measure here (e.g. Fig. 8 of Abadi et al. 2010). The empirical model of Cautun et al.

(2020), which was fitted to MW-mass haloes using a suite of simulations that include the one used in this study, results in good agreement with the median contraction the population they use to calibrate it. There is however scatter at the $\sim 20\%$ level, which we believe to be reflective of the different assembly histories that galaxies have experienced. The inclusion of information concerning the assembly history of galaxies and other morphological properties – e.g. presence and age of a stellar bar – could help reduce the halo-to-halo scatter in future contraction models. We also find that there are times during the evolution of a halo when its central dark matter mass decreases, although it always remains more massive than its DMO twin. We have identified two main processes responsible for lowering the central dark matter mass.

The first is AGN-induced gas blowouts. These events involve gas that had slowly become so dense so as to become gravitationally dominant in the central regions. As the gas is violently expelled, the central regions of the halos expand in a process analogous to that discussed by Navarro et al. (1996a). Both dark matter and stars participate in the expansion. Interestingly, we find that these blowouts can reduce the enclosed dark matter and stellar mass at radii much larger than those in which the gas is gravitationally dominant. Although it is clear that the effect of the blowouts fades away at larger distance, we hypothesize that the very long timescales of the gravitational perturbations caused by the gas before being blown out are responsible of this effect. In all cases, the initial inflow of gas occurs during or shortly after an interaction with a nearby galaxy.

The second process that causes the central halo regions to expand is a bar-mediated transfer of angular momentum. This transfer reduces the central DM density at a rate that is likely set by the time-averaged stellar bar strength. The net change in the central dark matter density depends on the length of time since the bar formed.

The effects of AGN-driven gas blowouts and bar-driven angular momentum transfer that we have investigated in this work are not confined to the central regions of the halos and can be seen out to at least 5 kpc from the centre. Here we have focused attention on the inner 2 kpc since this radius lies in the well-converged region as judged by the Power et al. (2003) criterion ($r_{\rm power} \sim 1.5{\rm kpc} - 1.75{\rm kpc}$).

Not all the galaxies in our sample undergo the two processes just described. As Fig. 2.2 shows, there is significant halo-to-halo scatter due to a variety of factors including differences in the assembly history of the halo, the central mass of the galaxy and likely the orbital distribution of dark matter particles. Roughly 30% of the studied sample host bars. About 15% to 20% of our MW-mass haloes have experienced at least one AGN blowout capable of reducing their central stellar and dark matter densities. This is likely to be a lower limit, as we focus on haloes with well defined evolutionary histories. At high redshifts, when the haloes and galaxies are assembled, it is difficult to assess the importance of the AGN blowouts.

While the reduction in central dark matter mass due to the presence of stellar bars similar to those that form in EAGLE is likely to be generic, the reduction caused by AGN-driven blowouts is expected to be specific to the EAGLE subgrid model. It would be interesting to explore if similar effects are present in other hydrodynamics simulations.

The processes discussed in our work indicate that the assembly of baryons in Milky Way-size haloes induces a complicated reaction in the DM halo. The degree of DM contraction in these haloes cannot be solely characterised by the present-day baryonic distribution, but by their complicated past evolutionary history. Our own Milky Way contains two of the ingredients that source the complexity highlighted in our study: a stellar bar and a supermassive black hole at the centre. Our results suggest that unless the baryonic effects described in our work are taken into account, studies that rely on contraction-based models, such as mass estimates of the Milky Way, or direct or indirect searches of dark matter, could contain biases that are very difficult to account for.

Third Chapter

The effect of baryons and alternative dark matter models on dwarf scales

3.1 Introduction

The precise nature of the dark matter (DM) is as-yet unknown, despite making up the largest fraction of the universal matter energy-density budget (Planck Collaboration et al., 2020a). This is because its existence has only been inferred through astrophysical tests relying on gravitational probes, such as the rotation curves of galaxies (Rubin & Ford, 1970), strong gravitational lensing (Wambsganss et al., 2004) or X-ray emission from galaxy clusters (Voigt & Fabian, 2006). Despite ongoing searches for a particle counterpart that could account for most of the dark matter, none have yet made a conclusive detection, directly (Marrodán Undagoitia & Rauch, 2016) or indirectly (Gaskins, 2016).

Nonetheless, assuming dark matter is a heavy particle whose distribution on large scales is solely dictated by gravity results in a remarkable agreement between predictions and observations on large cosmological scales (Davis et al., 1985). These range from the distribution of galaxies at the present-day (Cole et al., 2005; Springel et al., 2006; Rodríguez-Torres et al., 2016), to the anisotropies imprinted in the Cosmic Microwave Background, back when the Universe was only 300,000 years old (Planck Collaboration et al., 2020a).

A natural particle candidate satisfying these criteria are weakly-interacting massive particles (WIMPs; Ellis et al. 1984). These are hypothetical particles which arise on electroweak

scales – O(GeV – TeV) – and whose predicted relic abundance is similar to the one required by the inferred DM density. Within the WIMP landscape, an exciting prospect is the lightest neutralino, a particle predicted from well-motivated minimal super-symmetric extensions to the Standard Model. These considerations make cold dark matter (CDM) the *de facto* DM model. However, no direct evidence for supersymmetry (Canepa, 2019) or WIMP-like dark matter candidates (Aprile et al., 2018) has been detected yet. As more of the plausible parameter space is excluded, we may need to re-visit our expectations on what the particle nature of the DM is.

Nonetheless, there are other well-motivated models which have not yet been ruled out. One such example is warm dark matter (WDM), a lighter particle than CDM with masses in the keV range. A promising WDM particle is the sterile neutrino, which is a hypothetical right-handed equivalent of the Standard Model (SM) neutrino. These arise naturally in many Grand Unified Theories (e.g. Pati & Salam 1974) and could provide a natural explanation for the small mass of SM neutrinos via the see-saw mechanism (King, 2015). Cosmologically, its lighter nature entails its free-streaming length – the spatial scale over which primordial density perturbations are erased – is larger than in CDM. Consequently, its power spectrum is suppressed at small spatial scales relative to CDM. This has a number of interesting consequences, from a decrease in the number of low mass haloes to a delay in their formation time. The latter effect also results in structural changes in the distribution of dark matter haloes, such as lower concentrations. Thus, WDM is able to reproduce the success of CDM on large scales, whilst modifying the predictions on smaller scales.

Another alternative is a particle that is able to scatter elastically with itself, self-interacting dark matter (SIDM). Although initially proposed to solve the so-called missing satellites and cusp *versus* core 'problems' (Spergel & Steinhardt, 2000), there are several particle physics models that naturally result in self-interactions between DM particles (e.g. McDonald 2002; Buckley & Fox 2010b). This leads to changes in the velocity and density profiles of the central regions of haloes, turning their cuspy NFW-like distributions to cored isothermal ones. Moreover, if the cross-section is large enough, core-collapse can be triggered and revert the flat density core to a super-cusp. Although the largest velocity-independent

cross-sections are likely ruled out based on cluster-mass constraints (Peter et al., 2013; Rocha et al., 2013), there is still the possibility of large cross-sections at low masses via velocity-dependent cross-sections. Nonetheless, it is worth noting that many of the previous constraints have been overstated to some degree, because off simplifying assumptions, limited cluster statistics, or a lack of baryons in the simulations from which the constraints are derived (Robertson et al., 2018).

The above changes to the DM model thus primarily alter predictions on small scales, either in the abundance of low mass structure or the distribution of DM in the centre of haloes. Consequently, we need to test these models in an appropriate environment where these changes are observationally accessible. An excellent test bench for this is the Local Group. This is because surveys such as SDSS, DES and ATLAS have made possible the discovery of low-surface brightness objects that probe the edge of galaxy formation (Torrealba et al., 2016). Moreover, GAIA offers a unique view into the kinematics of some of these objects, leading to the discovery of the 'feeble-giants' Antlia II (Torrealba et al., 2019), whose properties are difficult to explain in a Universe dominated by collisionless dark matter (Caldwell et al., 2017; Fu et al., 2019; Borukhovetskaya et al., 2022).

Objects orbiting around larger, more massive ones are subject to gravitational tides, which strip dark matter from their haloes. At fixed orbital parameters, the efficiency of this process depends sensitively on the internal structure of the DM haloes (Peñarrubia et al., 2010). Thus, differences in the satellite's underlying inner dark matter distribution are amplified, leading to very different satellite populations based on their survivability. Thus, this suggests that in principle, we may indirectly probe the nature of dark matter by comparing the properties of the present-day population of satellites around the Milky Way (MW) to the results of hydrodynamical simulations.

For the purposes of this study, the inclusion of baryons is paramount for reliable predictions. Firstly, it allows a more meaningful comparison to observations, since not all DM halos host galaxies. Secondly, the processes associated with galaxy formation and evolution can alter the global properties of haloes and how dark matter is distributed within. These effects are mass dependent and could, in principle, be degenerate with changes to the DM model

(Khimey et al., 2021; Burger et al., 2022), e.g. core formation driven by supernovae-driven gas blowouts (Navarro et al., 1996b; Read & Gilmore, 2005) *vs* self-interacting dark matter. Moreover, the presence of a disc, and subsequent contraction of the DM halo, can greatly enhance the destruction of subhaloes (Sawala et al., 2017; Garrison-Kimmel et al., 2017; Richings et al., 2020).

Limits on available computational power means we need to resort to subgrid implementations to model baryonic physics when simulating galaxy formation in a cosmological setting. Although they are able to make realistic predictions once calibrated (Genel et al., 2014; Schaller et al., 2015; Ludlow et al., 2017; Hopkins et al., 2018), there are different parametrisation choices and many of their free parameters can be degenerate with others. This can result in different predictions on yet unconstrained relations, such as the properties of the IGM (Kelly et al., 2021).

One such example particularly relevant to stripping is whether supernovae-driven gas blowouts are able to form cores in dwarf galaxies. Depending on the choice of subgrid parameters, simulations produce dwarfs with central density cores (FIRE, Oñorbe et al. 2015; NIHAO, Tollet et al. 2016) or not (EAGLE and AURIGA, Bose et al. 2019). The definitive or insufficient evidence for the existence of cores in dwarf galaxies is hotly debated, with some attributing their inferred presence to difficulties in the kinematic modelling (Oman et al., 2019; Roper et al., 2022). Nonetheless, it is important to consider both possibilities, especially from the point of view of disentangling baryonic effects from different DM models.

Given the all of the above, this chapter sets out to study how the properties of the satellite systems of haloes with masses similar to our MW – within a factor of two – change when the DM is neither cold nor collisionless. Given the importance of baryons, and that they may affect the inner dark matter distribution in satellites, we also consider different values for the subgrid parameters to explore variations in the population of satellites associated to this. To this end, we simulate cosmic structure formation in CDM, WDM and a range of SIDM cross-sections in the same $(12\ \mathrm{Mpc})^3$ periodic volume. This allows us to focus on the same haloes in this suite of thirteen different simulations and study how the properties

of their satellite systems change.

This chapter is structured as follows. Section 2 introduces the different models we use to simulate structure formation, from N-body to full-hydrodynamical realisations. Section 3 presents the methods used to measure and compare the properties of interest and the sample selection. This is followed by an overview of the changes in the properties of field haloes driven by different models. Subsequently, we shift our analysis to our sample of mass-selected haloes to investigate how their satellite populations are affected under different models. Finally, we investigate the cause behind the differences that these changes have had on the their satellite stripping and survivability.

3.2 Simulations

In this section we give an overview of the EAGLE subgrid physics used in this work and describe how we model the changes in the dark matter and baryon models.

3.2.1 The code

The EAGLE project (Schaye et al., 2015; Crain et al., 2015) is a suite of hydrodynamical cosmological simulations that follow the formation and evolution of cosmic structure from ΛCDM initial conditions assuming the cosmological parameter values from Planck Collaboration et al. (2014). They were performed using a modified version of the P-Gadget3 code (Springel, 2005) that incorporates subgrid prescriptions for the physics relevant to galaxy formation and evolution: radiative cooling and photoheating (Wiersma et al., 2009), star formation and evolution (Schaye, 2004; Schaye & Dalla Vecchia, 2008), stellar feedback (Dalla Vecchia & Schaye, 2012), black hole seeding (Springel et al., 2005a; Booth & Schaye, 2009), its subsequent growth and stochastic, thermal AGN feedback.

The values of the parameters used in modelling these processes were set by requiring a good match to the observed $z = 0.1$ galaxy stellar mass function, the distribution of galaxy sizes and the amplitude of the central black hole mass *vs* stellar mass relation. Once calibrated

in this way, EAGLE reproduces a number of population statistics (Schaller et al., 2015; Ludlow et al., 2017).

We use the calibration made for the higher mass resolution version of EAGLE to simulate structure formation in a periodic volume of $(12\ \mathrm{Mpc})^3$. We populate it with 2×512^3 particles, half of which are dark matter and the rest gas particles. This corresponds to a particle mass resolution of $\sim 4\times10^5$ and $\sim 8\times10^4\ \mathrm{M}_\odot$, respectively. The initial conditions were generated using MUSIC (Hahn & Abel, 2011).

3.2.2 Baryonic physics

An important parameter determining whether gas blowouts can flatten the density profiles of dark matter haloes in hydrodynamical simulations is the star formation density threshold (Benítez-Llambay et al., 2019). This parameter sets the minimum density required for a gas particle to be eligible to become a star particle. The EAGLE subgrid physics uses a metallicity (Z) dependent term given by (Schaye, 2004):

$$\rho_{\mathrm{th}} = n_{\mathrm{th},0}\left(\frac{Z}{0.04}\right)^{\alpha}, \tag{3.1}$$

where $n_{\mathrm{th},0} = 10^{-1}\ \mathrm{cm}^{-3}$ and $\alpha = 0.64$. These values result in thresholds that are comparatively lower than other hydrodynamical simulations, e.g. $10^2\ \mathrm{cm}^{-3}$ in GASOLINE (Zolotov et al., 2012) or $10^3\ \mathrm{cm}^{-3}$ in FIRE-2 (Fitts et al., 2017). Consequently, gas cannot accumulate in sufficient quantities at the centres of haloes to become gravitationally relevant before being blown out via supernovae feedback resulting from star formation. As a result, the EAGLE model cannot form cores through baryonic blowouts (Navarro et al., 1996a).

Nonetheless, ρ_{th} is a free parameter of the subgrid physics. Indeed, star forming gas clouds in the real universe reach gas densities in excess of $10^4\ \mathrm{cm}^{-3}$ (Lada et al., 2009). Despite the dichotomy between these densities, the value ρ_{th} employed by the simulations used in this work should be regarded as a numerical parameter, rather than a physical one. This is because, for the temperature floor ($T = 4000\ K$) and mass resolution we use ($m_{\mathrm{baryon}} \sim 8 \times 10^4\ \mathrm{M}_\odot$), the maximum density at which Jean's collapse is resolved corresponds to $\sim 20\ \mathrm{cm}^{-3}$.

Given the possibility that internal structural changes that occur in the real Universe are not captured by the low values of star formation threshold used in the fiducial subgrid parameters of EAGLE. Thus, we explore how baryon-induced cores affect the satellite population of the objects with masses similar to our Milky Way by running models with higher density thresholds, setting $\rho_{\rm th}$ to a constant value of $10\,{\rm cm}^{-3}$, lower than the aforementioned density limit for our simulation parameters. Although this is still comparatively low than other simulations, it is large enough for gas blowouts to turn cusps into cores at the dwarf galaxy scale in EAGLE (Benítez-Llambay et al., 2019). We refrain from using larger density thresholds as this would drastically reduce the efficiency of the thermal supernova feedback implemented in our simulations. This would make dwarf galaxies unrealistically baryon-dominated in their centres at all times (Benítez-Llambay et al., 2019), unless other subgrid model parameters are re-calibrated. We have checked that basic galaxy properties, such as the stellar-to-halo-mass relation, do not change significantly across the models used in this work.

To distinguish between both baryonic physics models, we henceforth refer to the fiducial, low density threshold value as LT and the higher value as HT from here on. Simulations without baryons are referred to as dark matter only (DMO).

3.2.3 Warm dark matter

We obtain the power spectrum of WDM, $P_{\rm WDM}(k) = T^2(k)P_{\rm CDM}(k)$, using the transfer function of Bode et al. (2001):

$$T^2(k) = [1 + (\alpha k)^{2\nu}]^{-5/\nu}\,. \tag{3.2}$$

Here, ν is a fitting constant equal to 1.2 and the parameter α depends on the assumed mass of the WDM particle:

$$\alpha = 0.049\left[\frac{m_{\rm th}}{\rm keV}\right]^{-1.11}\left[\frac{\Omega_{\rm WDM}}{0.25}\right]^{0.11}\left[\frac{h}{0.7}\right]^{1.22} h^{-1}\,{\rm Mpc}\,. \tag{3.3}$$

For this work we assume $m_{\rm th} = 2.5\,{\rm keV}$. This is lighter than the equivalent thermal relic mass of a 7 KeV sterile neutrino model associated with the unidentified 3.5 KeV X-ray line

(Boyarsky et al., 2014). Nonetheless, we choose this value to enhance the differences with respect to CDM to allow for an easier comparison. We can estimate the mass scale where the differences with respect to CDM are noticeable, $m_{1/2}$. It corresponds to the Jean's mass of a perturbation with a wavelength equal to the one where the WDM power spectrum is half of the CDM one. For the values used in this work, $m_{1/2} = 1.4 \times 10^9\,\mathrm{M}_\odot$.

3.2.4 Self-interacting dark matter

Self-interactions are modelled using the Monte-Carlo implementation described in Robertson et al. (2017). Dark matter particles can scatter each other when they are closer than the Plummer-equivalent softening length of the simulations. The probability of any two neighbouring particles scattering is a function of their relative velocity and the assumed cross-section.

In this study, we use three different cross-sections; two velocity-independent, isotropic cross-sections of 1 and 10 $\mathrm{cm}^2\mathrm{g}^{-1}$ and an anisotropic, velocity-dependent one given by:

$$\frac{\mathrm{d}\sigma}{\mathrm{d}\Omega} = \frac{\sigma_{T,0}}{4\pi\left(1 + \frac{v^2}{w^2}\sin^2\frac{\theta}{2}\right)^2}\,, \tag{3.4}$$

where v is the relative velocity magnitude between particles in their centre of mass frame and θ the scattering angle relative to their incoming direction. The above expression results from assuming that the particles scatter in a Yukawa potential under the Borne approximation (Ibe & Yu, 2010).

The parameters w and $\sigma_{T,0}$ correspond to the velocity scale below which the cross-section is roughly constant and its asymptotic, low-velocity value, respectively. We use $w = 560\,\mathrm{kms}^{-1}$ and $\sigma_{T,0} = 3.04\,\mathrm{cm}^2\,\mathrm{g}^{-1}$ to reproduce the best-fitting mass-dependent cross-section of Kaplinghat et al. (2016), which is derived from constraints on the inferred cross-section from dwarf to cluster scale haloes. In practice, these values yield an approximately constant cross-section of $\sim 3\ \mathrm{cm}^2\mathrm{g}^{-1}$ on dwarf galaxy scales.

3.3 Methods

Here we discuss how we find cosmic structure and link subhaloes across snapshots to build their merger trees. We also show how we remove WDM spurious groups, select our sample of haloes and their satellites and correct for orphan galaxies. The former are satellite galaxies whose host dark matter halo has been lost from the halo catalogues. Their omission leads to underestimates of the satellite radial distributions in the central regions of haloes, where they are the dominant population.

3.3.1 Structure finding and merger trees

To identify cosmic structures, we assign particles into distinct groups according to the friends-of-friends (FoF) percolation algorithm (Davis et al., 1985). Each group is made up of particles that are within 0.2 times the mean interparticle separation from one another. Gravitationally bound substructures are found with the SUBFIND algorithm (Springel et al., 2001), which, using particle velocity and position information, identifies self-bound structures within a larger FoF group.

We follow the time evolution of all SUBFIND groups using their merger trees, which are built by cross-matching a subset of the most bound particles between consecutive time outputs (Jiang et al., 2014). This implementation is able to link SUBFIND groups that have temporarily disappeared from the catalogues (e.g. due to insufficient density contrast near centres of more massive haloes) for five consecutive data outputs or less. The main progenitor branch is then found by identifying the progenitor branch with the largest integrated mass (De Lucia & Blaizot, 2007). This reduces the influence that halo switching, prone to occur during major mergers, has on the identification of the main progenitor at high redshifts.

3.3.2 WDM spurious group removal

Particle-based simulations starting from a density perturbation power spectrum with a resolved cut-off produce spurious structure along filaments. This is a consequence of the discrete representation of the underlying density field (Wang & White, 2007). Consequently, this results in an artificially high number of objects below the mass scale where no structure is expected to form.

In this study, we remove them from the WDM simulations using the two criteria of Lovell et al. (2014). Firstly, we remove all groups whose peak bound mass is below the mass scale at which the number of spurious groups is equal to genuine ones, $M_{\rm lim}$. This is related to the mass resolution of the simulation and the assumed power spectrum via:

$$M_{\rm lim} = 5.05\,\bar{\rho}\,d\,k_{\rm peak}^{-2}, \tag{3.5}$$

where d is the mean interparticle separation, $k_{\rm peak}$ the wavelength at which the dimensionless power spectrum, $\Delta^2(k)$, peaks and $\bar{\rho}$ the mean density of the universe. For the simulations and WDM model used in this study, $M_{\rm lim} = 1.4 \times 10^8$ M$_\odot$.

Finally, we select the particles bound to the group when it first reached half of its peak bound mass. We then compute the inertia tensor of those particles in the initial conditions and define the sphericity as the ratio between the smallest and largest eigenvalue of their inertia tensor, $s \equiv c/a$. All groups with $s \leq 0.16$ are removed, since the Lagrangian regions associated to spurious groups are significantly more flattened than those in which genuine haloes form.

To investigate whether our analysis concerning the visible population of galaxies (and hence galactic satellite systems) could be affected by spurious haloes, we examined the resulting stellar mass functions of all $z = 0$ subhaloes. We found no spurious haloes hosting visible galaxies, which reflects the fact that the cut derived from equation (3.5) is at an order of magnitude lower than the mass scale at which galaxy formation can occur in EAGLE-based models (see Benitez-Llambay & Frenk 2020). The mass threshold for galaxy formation in WDM is itself raised to a higher mass due to the delay in structure formation, as it will

be discussed in §3.4.1. Our results are therefore not sensitive to the presence of spurious WDM haloes.

3.3.3 Halo and subhalo matching across simulations

We match the main SUBFIND group of each FoF group across simulations by selecting their 100 most bound particles as identified by SUBFIND. We then select a candidate match by identifying which group the majority of the particles belong to in the other simulations. The process is then repeated in reverse, and if this bijective process is successful, we confirm the match.

Matching substructure is less trivial owing to the fact that the same object may have followed different paths and have been stripped to varying degrees once it entered the virial region of a larger object. To minimise the effect of these differences, we perform the bijective match at the time when their bound mass peaked.

3.3.4 Sample Selection

As we are interested in studying the satellite system of haloes similar to that of our own Milky Way, we restrict our analysis to haloes of mass M_{200}* at $z = 0$ in the range $0.5 - 2.5 \times 10^{12}$ $M_\odot$. This is within a factor of two from recent observational estimates of the Milky Way's halo mass (Callingham et al., 2019; Cautun et al., 2020). Eight haloes satisfying this criterion were identified in each version of the simulations. However, one is undergoing a merger at $z = 0$, which we remove from further consideration.

Their resolved satellite systems are defined by identifying all SUBFIND groups that are within 300 kpc from the centre of their host halo and have one or more bound stellar particle at $z = 0$. We also enforce that the identified structures are heavily dark matter dominated, namely, $M^{\rm DM}_{\rm SUB}/M^{\rm tot}_{\rm SUB} > 0.8$. This additional condition stems from the fact that dense clumps of gas in the HT versions are identified as self-bound structures by SUBFIND.

*M_{200} is defined as the mass contained within a sphere of mean density 200 times the critical density of the universe.

Their inclusion in the satellite population would lead to biased radial distribution functions, as they form in the inner few kiloparsecs of the dark matter halo, where the gaseous disc is located. Some gas clumps are also present in the low threshold versions, but are far less common than in the higher density threshold counterparts.

3.3.5 Orphan galaxies

In simulations of structure formation with limited resolution, substructure can be artificially disrupted. Substructure is lost whenever its mass drops below the 20 particle threshold limit imposed by SUBFIND on bound structures. The decrease in the bound number of particles can occur, for example, when a subhalo has been tidally stripped or the density contrast is insufficiently high for it to be detected near the central regions of a more massive neighbour. This does not necessarily imply that they have been disrupted, since increasing the particle mass resolution would lead to their ongoing survival for a longer time. This is both due to an increased capability in tracking objects to lower masses, as $m_{\rm limit} \sim 20 m_{\rm dm}$, and due to a reduction in the effect of tides resulting from smaller artificial cores.

Thus, accounting for these 'disrupted' objects improves the convergence of the predicted radial distribution function of satellites around Milky Ways (Newton et al., 2018). Moreover, they are required to correctly predict the satellite luminosity functions at stellar masses below 10^5 $M_\odot$, even in high resolution simulations (Bose et al., 2020).

In this study, we tag as orphans all dark matter haloes that had at least one bound stellar particle before being lost from the merger trees. We then use their most bound DM particle – identified during the last data output when they were resolved – as a proxy for the position and velocity of the orphan galaxy. A small subset of orphans end up sharing the same tracer particle ID. In such cases, we discard the higher redshift counterparts and keep the one orphaned at a later time.

Once the orphan population is identified, we track their positions until one of the two conditions given in Simha & Cole (2017) are fulfilled. The first one is that they have

existed for longer than the time for their orbit to decay due to dynamical friction:

$$\frac{T_{\rm df}}{\tau_{\rm dyn}} = \left(\frac{r}{r_{\rm circ}}\right)^{-1.8}\left(\frac{J}{J_{\rm circ}}\right)^{0.85}\frac{M_{\rm FoF}(<r)/M_{\rm sub}}{2B(1)\ln\Lambda}\,, \tag{3.6}$$

where r and J are the orbital radius and angular momentum of the orphan, and the corresponding values for a circular orbit of the same binding energy are $r_{\rm circ}$ and $J_{\rm circ}$, respectively. The Coulomb logarithm is taken to be $\ln\Lambda = \ln M_{\rm vir}/M_{\rm sub}$ and $B(x) \equiv \mathrm{erf}(x) - 2xe^{-x^2}/\sqrt{\pi}$. The dynamical timescale of the halo, $\tau_{\rm dyn}$, is estimated as:

$$\tau_{\rm dyn}(z) = \frac{1}{\sqrt{4\pi G\Delta_{\rm vir}(z)\rho_{\rm crit}(z)}}\,, \tag{3.7}$$

where $\rho_{\rm crit}$ is the critical density of the universe and $\Delta_{\rm vir}$ is the overdensity of a just-collapsed spherical top hat density perturbation (Bryan & Norman, 1998; Eke et al., 1996):

$$\Delta_{\rm vir}(z) = 18\pi^2 + 82[\Omega_{\rm m}(z) - 1] + 39[\Omega_{\rm m}(z) - 1]^2\,. \tag{3.8}$$

The dynamical friction timescale is first calculated immediately after the galaxies are orphaned. If the orphan subsequently enters the virial region of a more massive FoF group, we re-calculate and update its value.

The second condition is to stop tracking orphans once they come within a radius that encloses a mean density equal to the mean density of the orphan, $\bar{\rho}_{\rm FoF}(<R_{\rm tid}) = \bar{\rho}_{\rm sub}(<R_{\rm sub})$. For the spatial scale of the subhalo, $R_{\rm sub}$, one may chose $R_{\rm max}$ or the half-light radius of the galaxy it hosts, R_{50}. Here we use the latter, since we are interested in modelling when the luminous component of the galaxy is affected by tides. A subset of orphans have no associated R_{50}, e.g those with only one bound stellar particle. In such cases, we compute the median of $\rho(<R_{50})/\rho(<R_{\rm max})$ for orphans with known R_{50} and multiply $\rho(<R_{\rm max})$ by this correction factor to estimate $\rho(<R_{50})$.

3.3.6 Orbit integration

The typical time resolution between consecutive data outputs for our simulations ($\sim$ 300 Myr) is much larger that the dynamical timescales of the central regions of the haloes in the mass range we study here. This means that outputs are unlikely to 'catch' satellites

near pericentre, potentially leading to an underestimate in their numbers in the central regions. This can affect estimates for the central radial distribution of satellites, as well as whether the tidal disruption criterion is fulfilled.

We interpolate the orbits of satellites between consecutive data outputs. Here we use the method described in Richings et al. (2020), with a few notable differences. Firstly, we use the AGAMA package (Vasiliev, 2019) instead of GALPY (Bovy, 2015). Secondly, we align the z-axis of the coordinate system with the $z = 0$ angular momentum of the galaxy's stellar component, if present. Finally, we use an axisymmetric multipole expansion for the potential sourced by the DM and a cylindrical one (Cohl & Tohline, 1999) for that of the baryons. The latter choice is made to model more accurately a flattened potential.

3.4 Field haloes

Here we discuss how the global and internal properties of field haloes differ among different DM models, as well the choice of subgrid physics. We begin by comparing the abundance and global properties of all haloes, luminous or dark, across our simulations. We discuss changes in the galaxy formation efficiency, namely, the fraction of luminous haloes in a given mass range. Finally, we study how the dark matter distribution differs between matched pairs of DM haloes across all simulations.

3.4.1 Halo mass functions

In Fig. 3.1 we show the halo mass function as measured in all simulations available for this volume. We have defined the virial mass as the mass contained within a sphere whose mean density is 200 times $\rho_{\rm crit}$. Focusing on the CDM DMO version, we show the expected power law dependence on M_{200} in the mass range $10^8 - 10^{11}\,{\rm M}_\odot$. At higher masses, we observe a deviation from this behaviour. This is driven by Poisson fluctuations that arise as a consequence of the small number of massive objects in our simulations. Indeed, within a volume of $(12\,{\rm Mpc})^3$, we expect less than 10 MW-mass haloes to form.

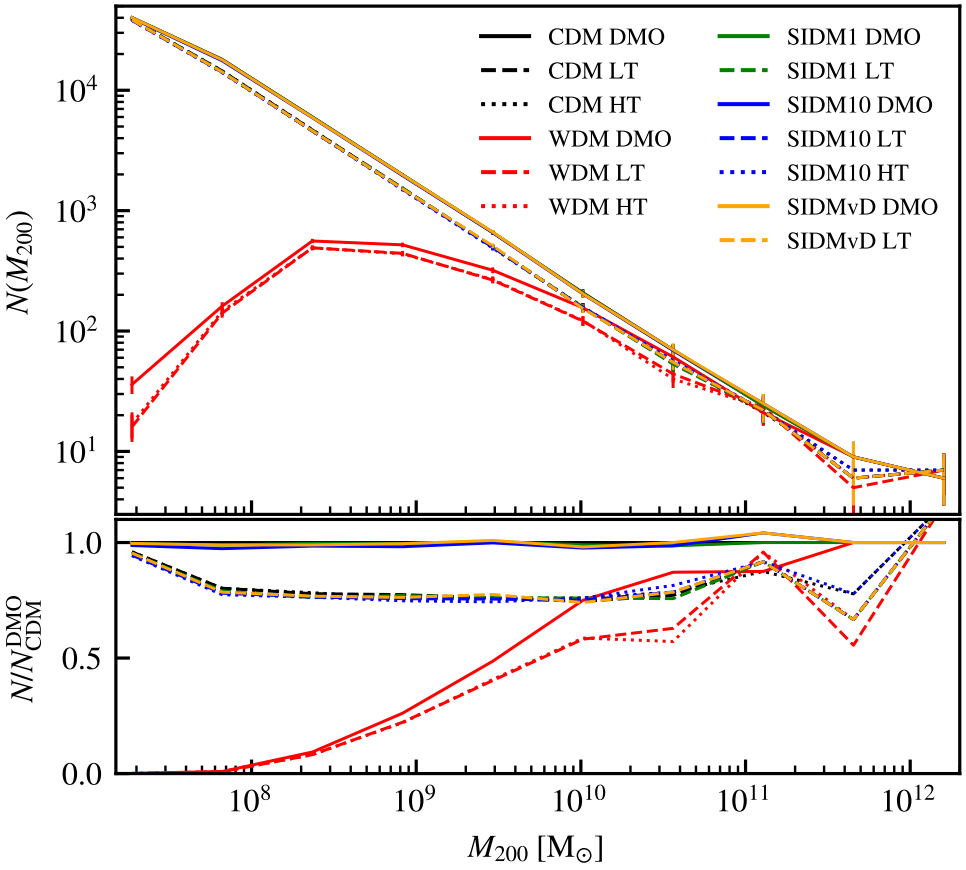

Figure 3.1: *Top panel*: halo mass functions for the CDM (black), WDM (red) and SIDM (green, blue and orange) versions of the simulation box used in this work. The line styles show whether they are measured in the DMO (solid), reference hydrodynamical (dashed) or high threshold hydrodynamical versions (dotted). The error bars correspond to the Poisson noise in each mass bin, which is largest at high masses. *Bottom panel*: ratio of the halo mass function of each version relative to that measured in the CDM DMO version.

The corresponding SIDM DMO simulations show no appreciable differences relative to the CDM versions in the sampled mass range, regardless of the cross-section value. This is because the primordial density fluctuation power spectrum was assumed to be the same across these two models. The addition of self-interactions primarily affects the central regions of DM haloes, where higher densities allow for more frequent interactions between particles. There are no significant differences in the distribution of dark matter near the virial radius nor in the number of objects that form, and hence there are no changes in the halo mass functions relative to CDM.

On the other hand, the WDM DMO simulation shows large differences with respect to the

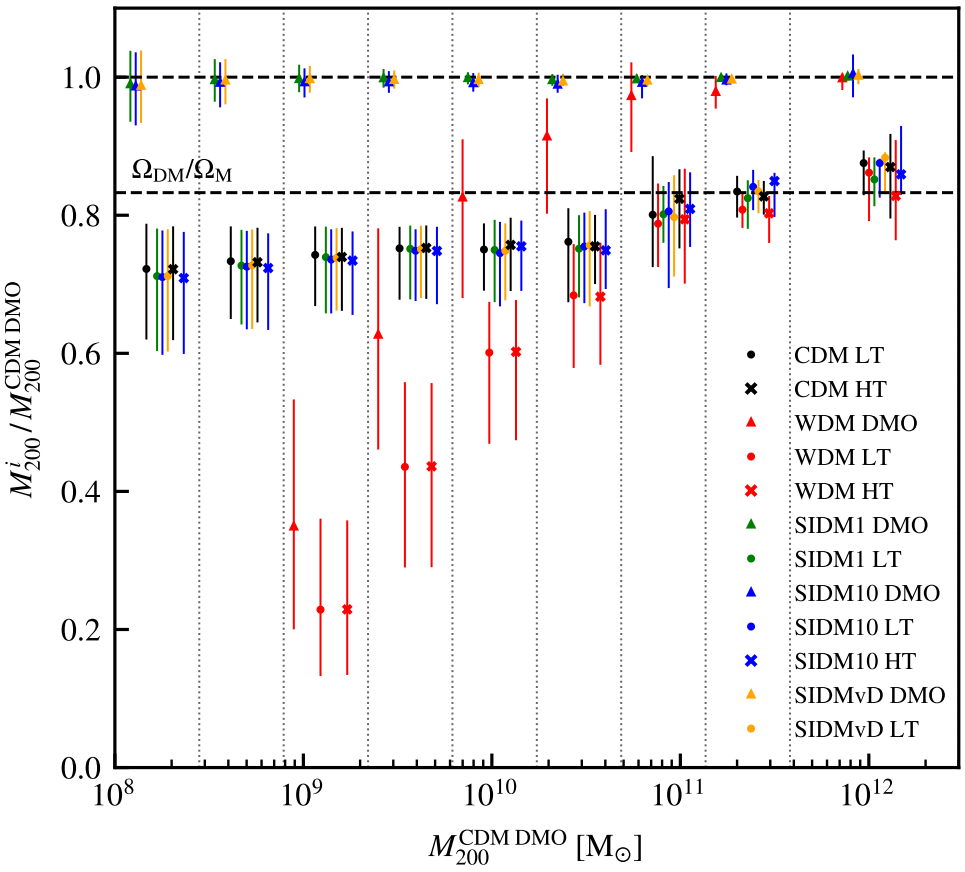

Figure 3.2: Median virial mass ratio of all field haloes relative to their CDM DMO counterparts, measured at $z = 0$ and binned as a function of the M_{200} of the CDM DMO counterpart. This is shown for the CDM (black), WDM (red) and SIDM (green, blue and orange) models, as indicated by the legend. The symbols indicate whether the simulation is DMO (triangle), LT (circle) or HT (cross). The error bars show the 16th and 84th percentiles, with the symbols being offset with respect to each other for clarity. The vertical dotted lines indicate the mass ranges used to bin haloes and the horizontal lines the unity ratio and the universal dark matter fraction.

CDM and SIDM models. Although at higher masses these are negligible, they become significant close to and below the half-mass mode of our WDM model. This is evident as a reduction in the number of haloes at a fixed M_{200} on those mass scales. This is due to the suppression of small spatial scale density perturbations, which results in fewer low-mass objects forming compared to the CDM and SIDM models. However, we point out that the systems that do form are less massive than their CDM counterparts, as shown in Fig. 3.2.

In this mass range, the hydrodynamical versions of all models exhibit a systematic suppression with respect to their DMO counterparts. This is a consequence of the loss of baryons

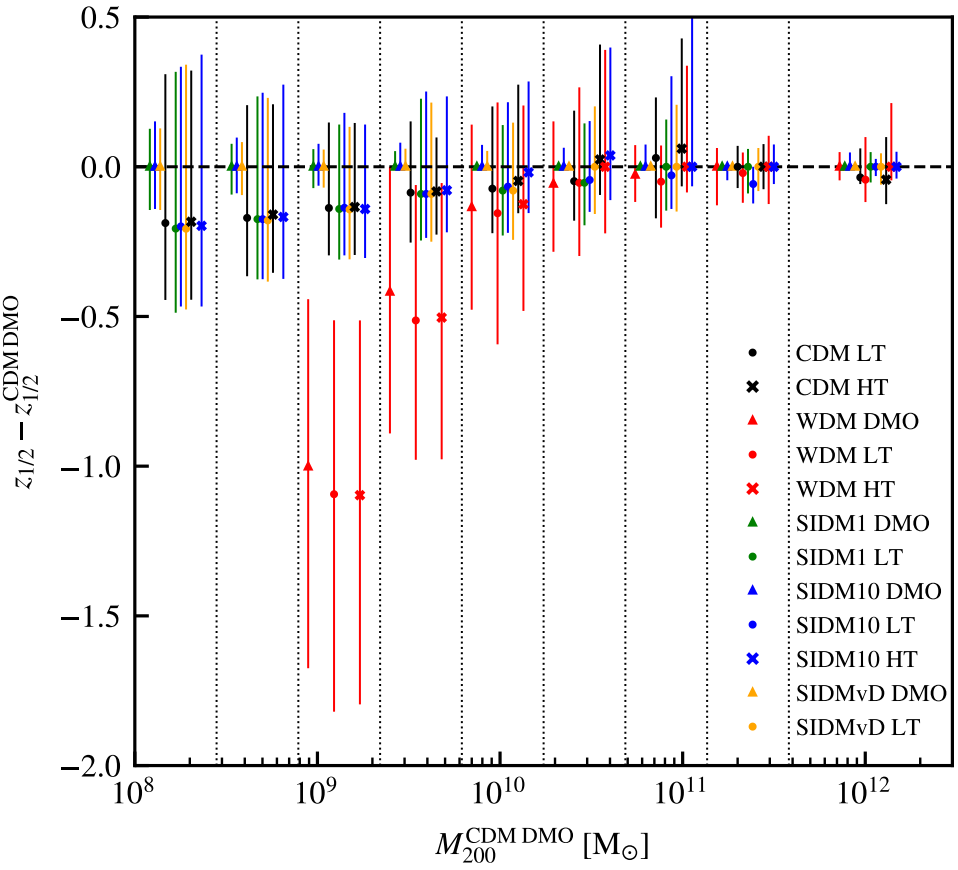

Figure 3.3: Difference in the formation time of haloes relative to their CDM DMO counterparts, quantified by the redshift at which the halo reached half of its $z = 0$ virial mass. This is shown for the CDM (black), WDM (red) and SIDM (green, blue and orange) models, as indicated by the legend. The symbols indicate whether the simulation is DMO (circle), LT (cross) or HT (triangle). The error bars show the 16th and 84th percentiles of the distribution in each mass bin, with the symbols being offset with respect to each other for clarity.

within the virial region of haloes at early times, which induces a shift in the halo mass functions towards lower masses. As shown in Fig. 3.2, all models in the largest mass bins have ratios close to the universal dark matter mass fraction. The mass loss is entirely explained by the removal of a large fraction of the baryons by feedback at early times. Focusing on lower masses, we see that the ratio for the CDM and SIDM models approaches a constant fraction that is lower than $\Omega_{\rm DM}/\Omega_{\rm m}$. This because the loss of baryons at early times hinders subsequent mass growth due to the resulting shallower gravitational potential well, leading to overall less massive haloes (Sawala et al., 2013). The case of WDM is the combination of the above together with a mass decrease arising from the cut-off in the power spectrum.

3.4.2 Halo formation times

The epoch at which haloes form determines the shape and normalisation of their DM density profiles. This is because the formation time reflects the density of the Universe when the density perturbation decoupled from the Hubble flow. As discussed above, the early loss of baryons can slow down the mass growth of DM haloes. Moreover, a cut-off in the power spectrum can also delay the formation of haloes.

To explore how the differences made to our models alter the formation time of haloes, we compare how formation times vary across matched pairs, relative to their CDM DMO counterparts. For this purpose, we identify the formation time with the redshift at which the main progenitor first reached half of its $z = 0$ virial mass, $z_{1/2}$. We compare how the median and scatter of this ratio varies as a function of mass in Fig 3.3.

We first note the similarities between the DMO versions of SIDM and CDM across the mass range studied here. Again, this is because the power spectra of inital density perturbations were the same in both models. On the other hand, the WDM DMO counterparts exhibit a formation delay that increases towards lower masses. This means that they form when the Universe is less dense compared to haloes that collapse earlier. Thus, their concentrations are expected to be lower in WDM than in their CDM and SIDM counterparts.

The hydrodynamical versions of all simulations have equal formation times for larger mass haloes, but begin to form slightly later at lower masses. This is caused by the loss of baryons at early times, which results in a measurable slow down in the growth rate of the halo due to the shallower potential well. This leads to lower virial masses at $z = 0$ relative to their DMO counterparts, as discussed previously.

The above changes in the formation times of haloes have important implications on the fraction that host galaxies. This is because the interplay between their mass accretion histories and the mass required to trigger the gravitational collapse of gas largely determines whether a halo is luminous or not at $z = 0$. Thus, delayed formation times and slower growth – indirectly probed by our $z_{1/2}$ metric – can reduce the amount of luminous haloes in a given mass range.

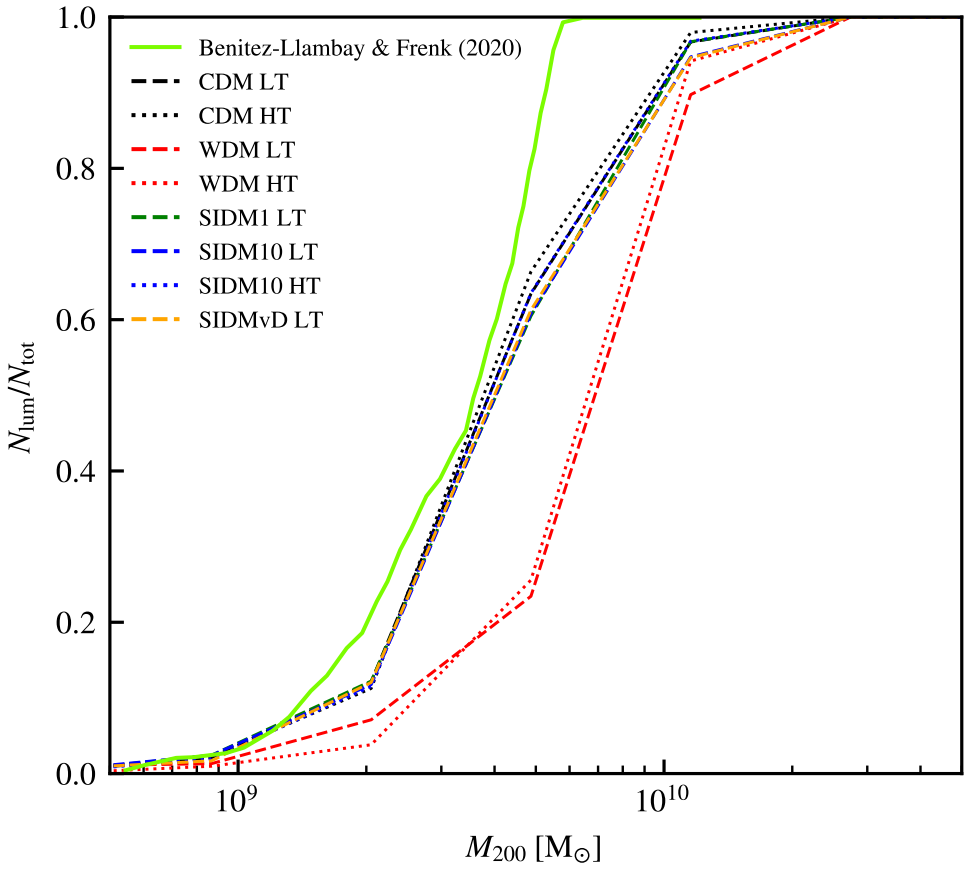

Figure 3.4: Fraction of field haloes that host a luminous component at $z = 0$, as a function of their virial mass. This is shown for the CDM (black), WDM (red) and SIDM (green, blue and orange) models, as indicated by legend. The linestyles indicate whether the simulation assumes a low (dashed) or high threshold (dotted) for star formation. The predicted halo occupation fraction of Benitez-Llambay & Frenk (2020) is shown as a green line.

We explore this in Fig 3.4, which shows how the halo occupation fraction (HOF) varies across different models. First, focusing on the CDM LT version, we observe three distinct regimes. At masses below $\sim 10^9\,M_\odot$, no haloes host luminous components, whereas all haloes are luminous above $\sim 10^{10}\,M_\odot$. The mass range between both limits is populated both by luminous and starless haloes.

The shape of the HOF is well understood from simple assumptions about when galaxy formation is triggered (Benitez-Llambay & Frenk, 2020). Essentially, any halo more massive than a redshift-dependent mass threshold, defined by the scale at which gas is unstable to gravitational collapse, will host a galaxy by $z = 0.$. Before reionisation, this threshold is determined by atomic hydrogen cooling; after reionisation it is determined by

the thermal state of the intergalactic gas. At high masses, all have crossed this threshold, hence all are luminous. Those at intermediate masses will cross it (or not) depending on their mass assembly histories, which vary across haloes. At lower masses, objects have not been able to trigger the gravitational collapse of gas and thus remain starless.

The predicted (CDM) HOF of Benitez-Llambay & Frenk (2020) is shown in Fig 3.4; its midpoint agrees well with our simulations. Nonetheless, there are some differences on the high and low mass ends. These are largely driven by the binning scheme we require to measure the HOF in our simulations, which is not fine enough to capture the sharp transition. However, all haloes above 6×10^9 $M_\odot$ should host a galaxy, but we find some that remain starless in our simulations. We attribute this to resolution effects: the limited resolution of our simulations (a factor of 8 coarser than that in the simulations of Benitez-Llambay & Frenk 2020) is not enough to follow accurately the rate at which the gas becomes denser as it approaches the threshold for star formation.

Turning back to the HOF measured in our simulations, we can understand the differences between all models. For the SIDM and CDM cases, regardless of the hydrodynamical model, no significant differences exist in the assembly of matched counterparts. Thus, haloes that form galaxies in one simulation always do so in the alternative models. On the other hand, the WDM simulations show a clear difference with respect to the latter two. This is connected to their delayed formation.

To understand why this is the case, consider a CDM halo that only just crosses the mass threshold for galaxy formation. Its WDM counterpart will, at a fixed redshift, be less massive due to its delayed formation. Consequently, it will not be massive enough to trigger the gravitational collapse of gas and will remain starless.

Evidently, the details of this simplified explanation change once a more realistic picture is considered. For example, lower concentrations of low mass haloes alter the hydrostatic equilibrium profile of gas, although this effect is minor. Moreover, the properties of reionisation also change as a reflection of the suppression of low-mass structure (Yue & Chen, 2012; Dayal et al., 2017). Finally, we note that the properties of the subset of starless

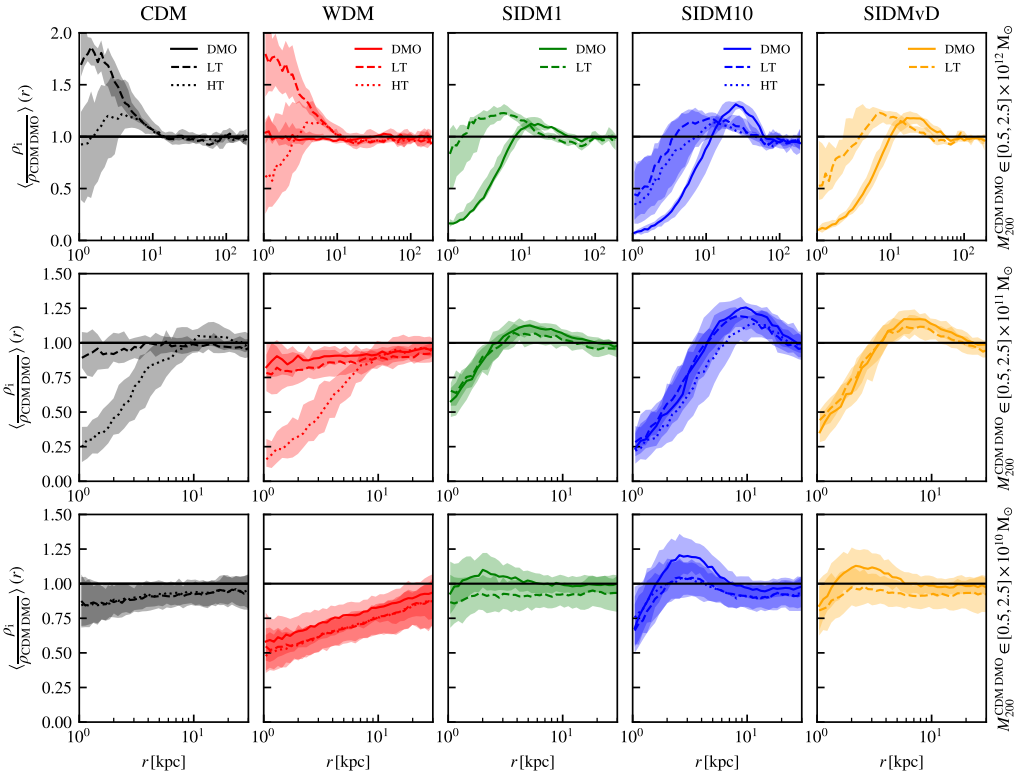

Figure 3.5: Median dark matter density profiles of field haloes as function of physical radius, relative to their matched CDM DMO counterparts. We use physical distances in kpc instead of R_{200} to prevent the location of overdensities due to substructure changing their positions between hydrodynamical and DMO counterparts. This would occur because the virial radii of haloes change across simulations, e.g Fig. 3.2, despite substructure being located at the same physical distance from the centre. The shaded areas around each line correspond to the 16th and 84th percentiles of the distributions. These were calculated for different mass bins in $M_{200}^{\rm CDM\,DMO}$, with each row corresponding to the range indicated on the right hand side. Note the change in the x-axis radial scale between the top and bottom rows. Different dark matter models are shown in each column, with line styles indicating whether they were measured in a DMO (solid), LT (dashed) or HT (dotted) simulations.

haloes which retain their gas content after reionisation (reionisation limited HI clouds, Benítez-Llambay et al. 2017a), remain as of yet, unexplored. It would be interesting to contrast how their properties and abundance compare to those formed in CDM, potentially yielding additional constraints on the nature of DM.

3.4.3 Density profiles

An important prediction of simulations of cosmic structure formation is the spherically-averaged radial density profile of DM haloes. Their profiles in CDM DMO simulations

are quasi-universal over 20 orders of magnitude in halo mass (Wang et al., 2020) and well described by the NFW (Navarro et al., 1996b) and Einasto (Einasto, 1965) formulas, which predict centrally divergent cusps. However, we expect significant changes to the the internal structure of DM haloes in the different models we study. Examining how they differ is an important step in understanding differences in the predicted $z = 0$ satellite system, since it influences how strongly they are tidally stripped (Peñarrubia et al., 2010).

Firstly, low-mass WDM haloes are likely to be less concentrated resulting from the delay in their formation relative to CDM. Scattering due to self-interactions will drive the centre of an initially cuspy profile to an isothermal, constant density core (Rocha et al., 2013; Robertson et al., 2021). Finally, the inclusion of baryons and different subgrid prescriptions may cause additional differences such as cores in CDM and WDM haloes, contraction of high mass haloes and an overall reduction in the DM density due to delayed growth.

We study in Fig. 3.5 how different choices for the DM model and baryonic physics alter the density profiles in three different mass bins, $\mathrm{M}_{200} \in [0.5, 2.5] \times 10^{12}\,\mathrm{M}_{\odot}$, $\mathrm{M}_{200} \in [0.5, 2.5] \times 10^{11}\,\mathrm{M}_{\odot}$, and $\mathrm{M}_{200} \in [0.5, 2.5] \times 10^{10}\,\mathrm{M}_{\odot}$. The latter corresponds roughly to the least massive haloes still able to form galaxies (see Fig. 3.4).

We have matched all central haloes in these bins to their CDM DMO counterparts. We then estimate their densities using logarithmically spaced spherical shells in physical distance and express them relative to the density of their CDM DMO counterparts. Finally, we average across all haloes in these mass bins that satisfy all three relaxation criteria of Neto et al. (2007):

- The virial ratio $|2K/U|$ should be less than 1.35.
- The centre of mass, measured using all DM particles within the virial region of the halo, should be within $0.07R_{\mathrm{vir}}$ from the centre of potential.
- The substructure mass fraction should be less than 10%.

Focusing first on the high mass haloes, we see large differences across different DM and baryonic physics models. For CDM, the addition of baryons has no effect on the DM

density at large radii. At smaller radii, there is an $\sim 80\%$ enhancement in the DM density in the LT version. The origin of this is the contraction of the halo in response to the formation of the galaxy at its centre. The HT simulation shows differences in the central parts, most notably a lower median density ratio. Nonetheless, it is still consistent with the LT one beyond ~ 2 kpc within the 1σ scatter. We have examined the profiles individually and note some of the lowest mass HT haloes within this mass bin have cores, whereas more massive ones have similar (or greater) contractions relative to their LT counterparts. These differences arise because the properties of the stellar component have changed across simulations, e.g. their masses, sizes and if they form a bar, its dipole moment strength. This affects how much the bar torques the surrounding dark matter.

The differences in SIDM relative to CDM depend on the assumed cross-section, although they all have lower central densities. No structures have undergone gravothermal collapse by $z = 0$, similar to what is found in other simulation-based studies with comparable low-velocity SIDM cross-sections (e.g. Vogelsberger et al., 2012; Turner et al., 2021): 10 and 3 $\mathrm{cm^2\,g^{-1}}$ for our velocity independent and dependent models, respectively. The largest of both values roughly corresponds to the boundary above which collapse can occur within a Hubble time. In contrast, SIDM models devised to fit the observed range of central DM densities – which require gravothermal collapse at the lowest mass scales under the effect of gravitational tides – typically require $\sigma \geq 30\ \mathrm{cm^2\,g^{-1}}$. Identifying the core radius with the radius at which the density ratio first crosses unity, we see it increases monotonically with the particle cross-section. This occurs because the radius at which the profiles become approximately isothermal depends on the scattering rate of particles, and thus on their cross-sections. The removal of DM from the centre to intermediate radii causes a localised enhancement whose magnitude and location sensitive to the assumed SIDM cross-section. Thus, parametric density profiles fitted to the central density, such as the generalised NFW (Zhao, 1996), do not fit these haloes well.

The addition of baryons in SIDM reduces the differences in the central regions of haloes compared to CDM DMO. For example, the median core radius decreases from 8 and 13 kpc to 1.5 and 4 kpc, for SIDM1 and SIDM10, respectively. The enhancement in density at

intermediate radii becomes more similar across SIDM models. Both are a consequence of the interplay between two competing effects: self-interactions driving a decrease in density and halo contraction counteracting it.

Focusing on the lower masses, the CDM hydrodynamical simulations produce profiles that are consistently less dense than their DMO counterparts. Although the offset relative to CDM remains constant throughout the radial ranges shown, there is a slight dependence on radius. We attribute both differences to the early loss of baryons and subsequent delay in formation time, which leads to lower densities and concentrations. The similarity between the LT and HT simulations is due to the baryonic component of these galaxies being small. Thus, baryonic blowouts are not able to perturb the inner dark matter distribution.

Both the DMO and hydrodynamical WDM simulations show a much stronger radial offset relative to CDM. This is because they are significantly less concentrated than their CDM counterparts. Thus, their shapes are very different.

Finally, low-mass SIDM DMO haloes show differences relative to CDM DMO similar to their more massive counterparts: a decrease in the central density and an enhancement at intermediate radii. Although it might seem as if the density suppression is less severe than for the high mass haloes, this is because the radial scale (relative to the virial radius), is not the same in the bottom and top panels. Once again, the inclusion of baryons reduces the differences relative to CDM. In fact, the lowest cross-section of 1 $\mathrm{cm}^2\mathrm{g}^{-1}$ shows no significant changes within the radial range shown. At large radii, we have the same constant density observed in CDM and WDM.

3.5 Satellite systems

As discussed in the previous section, changes to the DM model and baryonic physics lead to differences in the overall number of haloes that form, their internal structure and the fraction that host galaxies. We now focus on how these changes propagate to the satellite population of haloes. We begin with a comparison of the $z = 0$ properties, followed by a detailed analysis of the main causes for the differences. Finally, we also consider

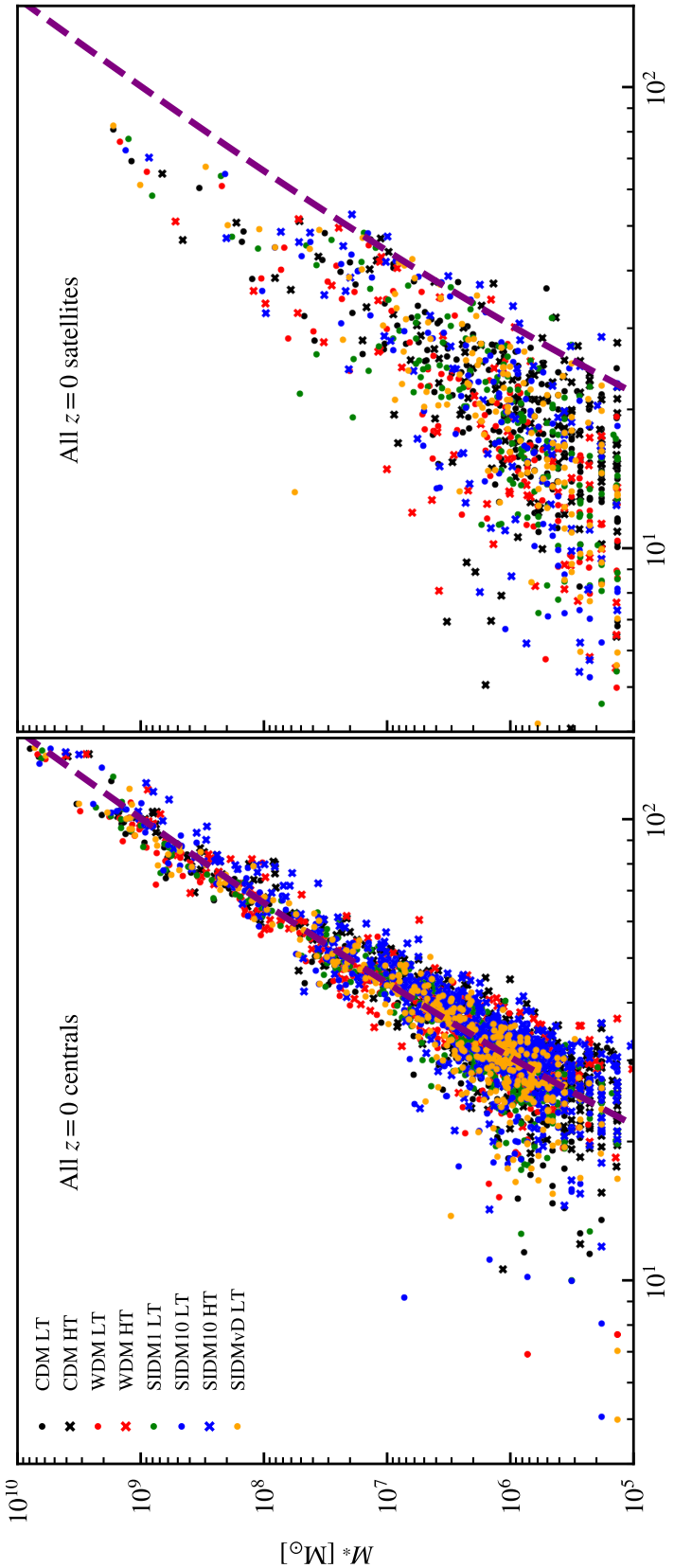

Figure 3.6: *Left panel:* relation between the stellar mass – within a spherical aperture of 30 kpc – and $V_{\rm max}$ of all central galaxies, with each marker corresponding to different DM and baryonic physics versions, as per the legend. The purple dashed line is the best-fit relation of the form $M_* \propto V_{\rm max}^{\gamma} \exp\{-V_{\rm max}^{\nu}\}$ to the CDM LT distribution, which is similar across all simulations considered in this work. *Right panel:* bound stellar mass of all $z = 0$ satellites of the studied halo sample across all simulations, as a function of their maximum circular velocity. The purple line corresponds to the same as in the left panel.

corrections to account for orphaned galaxies, which are the dominant population in the central tens of kiloparsecs and belong to the ultra-faint regime.

3.5.1 A first look at the effect of tides

The left panel of Fig. 3.6 shows the stellar mass to $V_{\rm max}$ relation measured for all central galaxies at $z = 0$. We see no systematic differences between models within the scatter, although the stellar components in HT can be slightly less massive than those in LT. Nonetheless, the best fit power law model with an exponential truncation, $M_* \propto V_{\rm max}^{\gamma} \exp\{-V_{\rm max}^{\nu}\}$, is similar in all of them. This fit was done using galaxies with $V_{\rm max} > 30 {\rm km\,s^{-1}}$ and $M_* > 10^6\,{\rm M}_\odot$ to exclude heavily-stripped backsplash haloes, which are significantly offset from the mean relation, and galaxies with less than ten stellar particles.

The equivalent relation for all the $z = 0$ satellites is shown in the right panel of the same figure. The observed offset at fixed stellar mass with respect to the relation for the centrals reflects the effects of tidal stripping. These remove mass as the satellites orbit more massive objects, decreasing their $V_{\rm max}$ over time. This primarily affects the DM, which occupies the less bound outskirts of the halo. The stellar component remains undisturbed for much longer than the DM, since it is more centrally concentrated.

3.5.2 Stellar mass functions

In Fig 3.7 we show the cumulative distribution of stellar mass for our sample of haloes. These were measured by selecting all satellites, using their SUBFIND bound stellar mass and averaging across all haloes each simulation. We only show the mass regime resolved by our simulations, which corresponds to masses larger than those of the ultra-faint satellite population. Nonetheless, it is clear that the number of $z = 0$ satellites above $M_* = 10^5\,{\rm M}_\odot$ is strongly dependent on the assumed DM and baryonic physics model.

The most numerous populations occur in the CDM LT simulation, as expected. This is because their haloes are cuspy and more concentrated than in all of the other hydrodynamical models. Thus, they are more resilient to tides. When the density threshold for star

formation increases (HT) – and gas blowouts are able to carve cores – the number of satellites decreases by about a third. This is evidence for increased stripping in the profiles with profiles.

The SIDM simulations also show a reduction in numbers that increases monotonically with the cross-section. As we saw in the previous section, SIDM models form the same number of haloes and galaxies as CDM. The only difference is the number of satellites that survive to $z = 0$. Therefore, the lack of satellites relative to CDM indicates an stronger stripping and destruction due to central cores. As we saw in the previous section, the cores driven by the DM self-interactions become larger when the cross-section is larger.

Finally, the WDM satellite population is less numerous than in CDM. Contrary to SIDM, a simple interpretation on what causes the suppression is less trivial. WDM forms fewer haloes and galaxies, but lower concentrations may also play a role in exacerbating the suppression (Bose et al., 2017). We discuss this in more detail in the following section, where we estimate how important each of these effects are. As in CDM, the increase in the density threshold for star formation leads to enhanced suppression relative to their LT counterparts.

The shape of the stellar mass functions are similar in all models at the higher stellar mass end, but there are large differences at lower stellar masses. Nonetheless, the most similar models to CDM LT (SIDM1 and SIDMvD) only show significant differences at $\sim 10^6$ $M_\odot$ whereas the other models already exhibit them at $\sim 10^7$ to 10^8 $M_\odot$

We show the observed stellar mass functions for the MW satellite population as a grey stepped line in Fig . 3.7. It is worth noting that the MW satellite population beyond the eleven classical satellites is incomplete. This is because surveys used for most discoveries below the classical satellite mass regime – SDSS (Alam et al., 2015) and DES (Bechtol et al., 2015; Drlica-Wagner et al., 2015) – are limited to certain regions of the sky and are flux-limited. Thus, the observational data should be considered a lower bound to the number of satellites. Nonetheless, the correction for incompleteness, based on the assumption of a CDM-like radial distribution, amounts to just a few satellites in the range

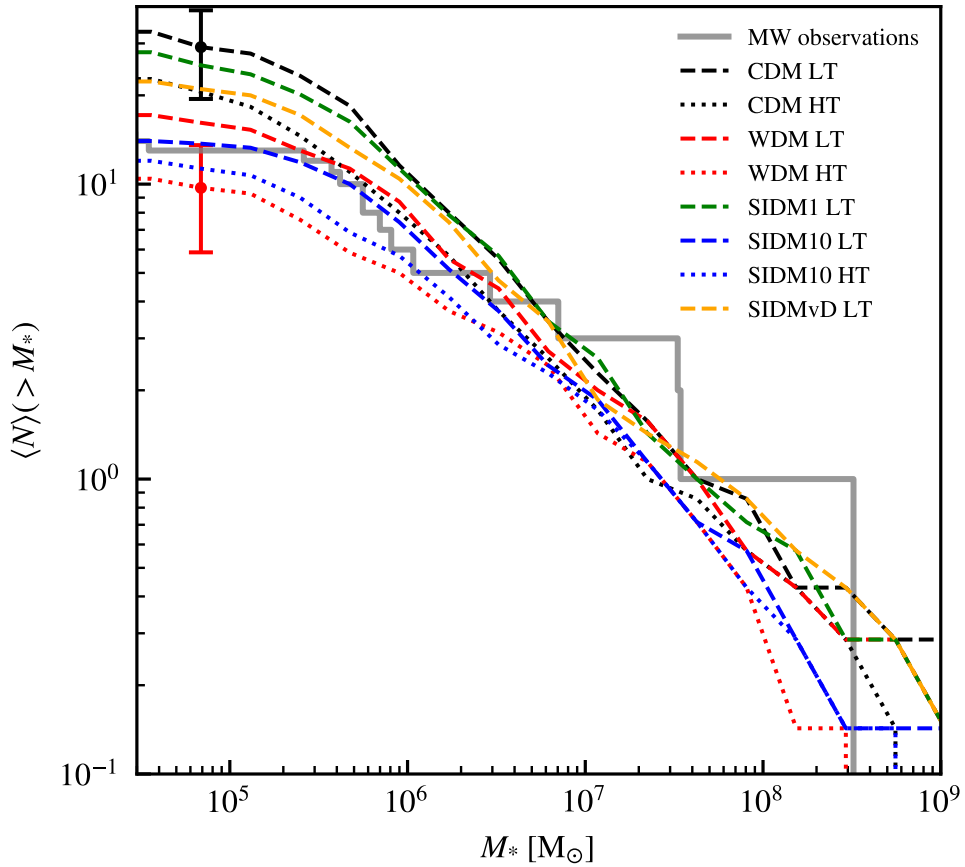

Figure 3.7: Stellar mass functions of the $z = 0$ resolved satellites, averaged across all our sample in a given simulation. The colours encode the dark matter model used, with the line styles showing the baryonic physics employed, as indicated in the legend. The error bars indicate the standard deviation of the CDM LT and WDM HT distributions at $M_* \sim 10^5\,\mathrm{M}_\odot$, which is roughly 35% of their values. This is also true for all other models in this mass range. The inferred stellar mass function based on observations is shown by the grey stepped line. These were calculated by taking the L_V of McConnachie (2012) and applying a mass-to-light ratio correction of 1.6 to all satellites except for the LMC (for which we use $M_*/L_V = 0.7$; Woo et al. 2008).

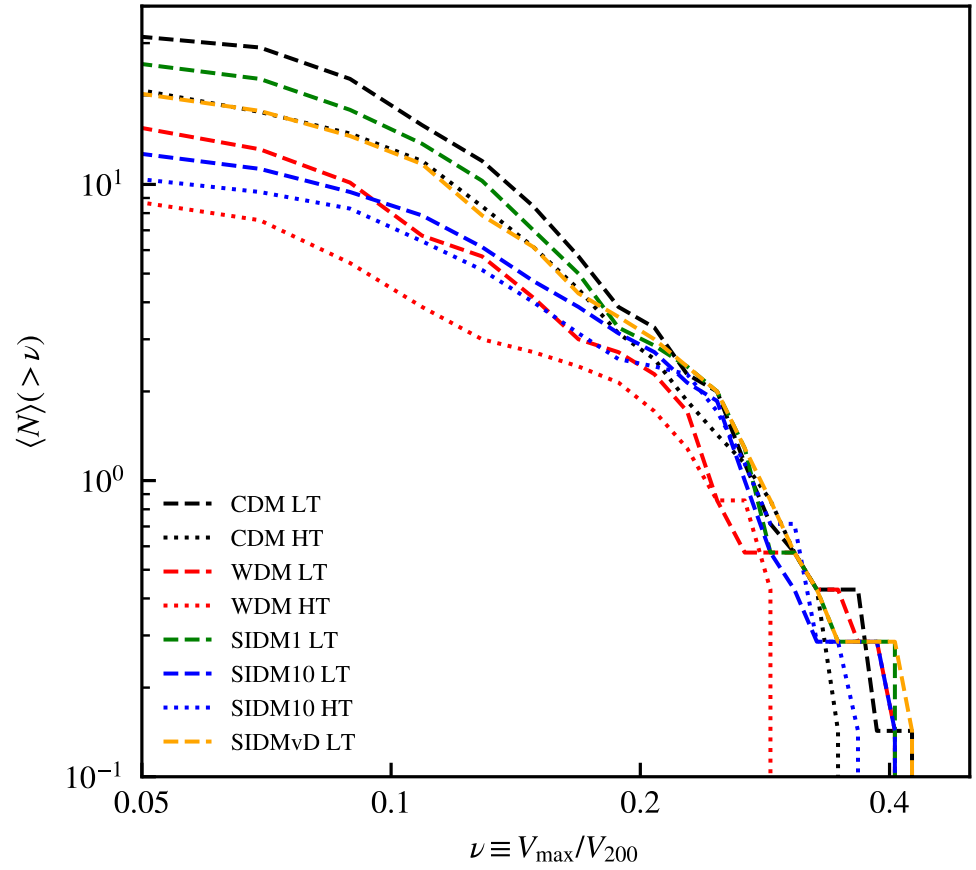

Figure 3.8: Distribution of the maximum circular velocities for all resolved satellites at $z = 0$, relative to the V_{200} of their host halo. The colours encode the dark matter model used, with the line styles the baryonic physics employed, as the legend indicates.

shown here (Newton et al., 2018).

When compared to observations, the *average* satellite stellar mass functions of our haloes predict more or fewer low-mass satellites above $M_* = 10^5\,\mathrm{M}_\odot$ than observed, depending on the model. However, the total number of satellites depends on the mass of the host halo, generally increasing in more massive haloes. Thus, one may in principle choose a more massive one to increase the total number of satellites. This scatter driven by the variation in the host halo mass in our sample limits the constraining power of our comparison to the real MW. However, even if we had chosen haloes in a narrower mass bin, there would still be an intrinsic scatter due to different assembly histories. As shown by the error bars in Fig. 3.7, which are representative of the scatter across all models, we find no significant inconsistencies with observations in the studied stellar mass range. Hence, we cannot

rule out any based on stellar mass functions alone. Finally, we are not able to find LMC and SMC analogues around any of the studied haloes. This is likely because they are uncommon in isolated systems (Santos-Santos et al., 2021).

3.5.3 Maximum circular velocities

An alternative way to examine how strongly the satellites have been stripped is through their $V_{\rm max}$ distributions. $V_{\rm max}$ decreases faster than the stellar mass of satellites, because the latter is more concentrated than the DM, which is stripped from the outskirts. We show the $V_{\rm max}$ distributions of the resolved $z = 0$ satellites in Fig. 3.8, averaged across all haloes in a given simulation.

We do not compare to observations since the maximum circular velocity of the halo is uncertain. Other quantities accessible to observations, such as the circular velocity at the half light radius, cannot be reliably measured in these simulations given their spatial resolution.

Similarly to the stellar mass functions, the CDM LT case represents an upper bound for all models, as it is the most resilient to tides. Although most models are similar at $\nu \geq 0.2$, noticeable differences start to appear below that. Interestingly, the distributions for CDM HT and SIDMvD are almost exactly the same below that scale, illustrating the potentially degenerate effects that baryons and different dark matter models can have.

3.5.4 Radial distributions

Another important prediction of our simulations is the radial distribution of satellites. We explore this in Fig. 3.9, where we show this distribution for different stellar mass bins. They were measured by integrating the satellite orbits for each halo during the last 300 Myr of the simulation, as described in Section 3. We then computed the time average and the average across the seven haloes of our sample in each simulation. The observed MW satellite radial distribution is also shown for comparison..

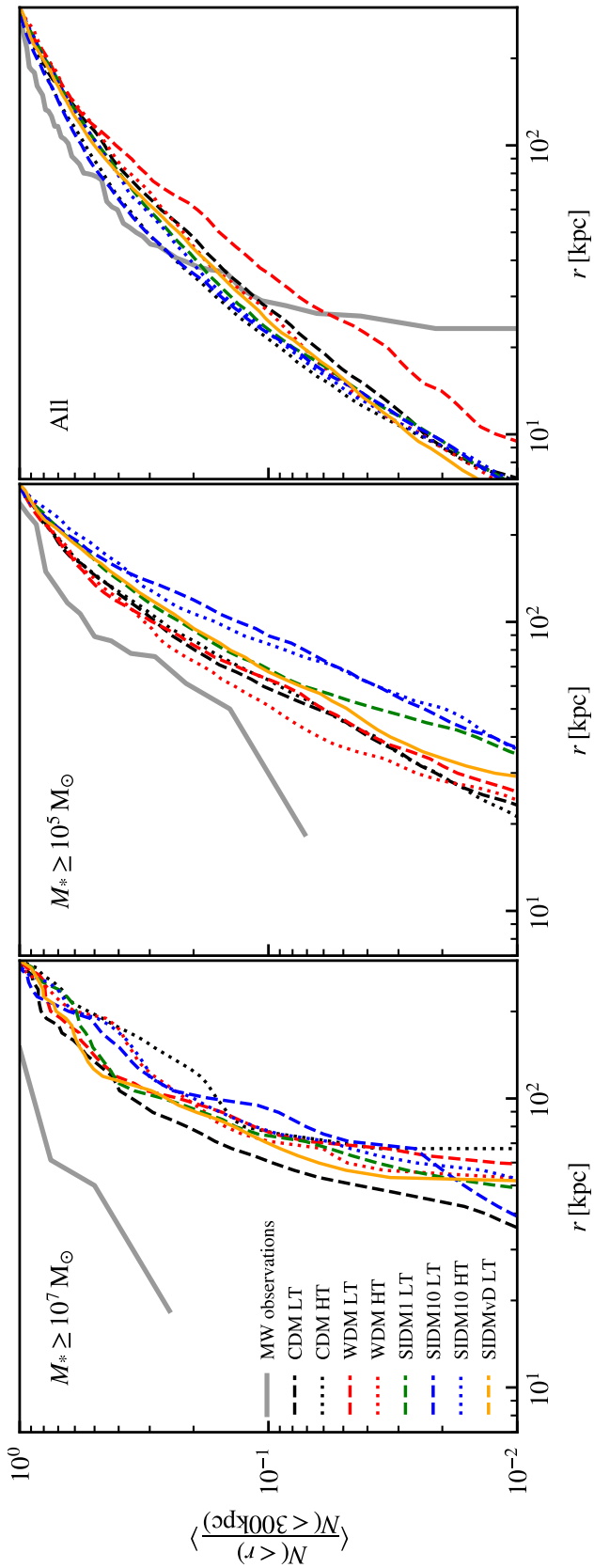

Figure 3.9: Radial distribution of $z = 0$ satellites, averaged over all haloes in our sample over the last 300 Myr of the simulation. This is shown across different mass bins, as indicated in the top left corner of each panel. The simulated sample for each bin corresponds to $M_* \geq 10^7$, all resolved, and all resolved plus orphans. The colours encode the dark matter model used, with the line styles the baryonic physics employed, as the legend indicates. The observed radial distribution of MW satellites is shown by the grey line. These values were calculated from McConnachie (2012), assuming $R_\odot = 8.29$kpc.

We see that the shape of the radial distributions depends strongly on the mass range. At high end, satellites occupy the outer regions of the halo, whereas lower mass satellites are closer to the centre. In the former, CDM LT is the most concentrated of all the models, although the distributions are noisy because of the low number of objects of these masses.

Once we start considering all the resolved satellite population (middle panel), we note that the radius enclosing half the total population – a measure of how concentrated these systems are – is smallest for the WDM models. This is closely followed by the CDM variations. The least concentrated satellite systems are the SIDM ones, with their concentration decreasing with increasing cross-section. In other words, even though WDM might have fewer satellites above a certain mass compared to SIDM, they are more concentrated. Increasing the density threshold for star formation leads to resolved satellite distributions that are somewhat less concentrated than their LT counterparts. The relative increase is similar for CDM, WDM and SIDM10, about 6%.

Correcting for orphans yields radial distribution functions that are much more centrally concentrated than the resolved satellite population. This is unsurprising, since orphans correspond to ultra-faints and populate the central regions. Generally, the inclusion of orphans makes the shapes of the radial distributions more alike across simulations and similar to that of the MW at large radii. Nonetheless, there is evidence that the MW satellite system may be more concentrated than in the simulations, perhaps due to the presence of Magellanic systems in the real MW (Santos-Santos et al., 2021). We note that the orphan population only includes galaxies whose resolved progenitors had peak stellar masses above the baryonic particle mass of the simulations. Haloes which would have had a total stellar mass less than one particle are not counted. Thus, the orphan populations here are only a partial census of the low-mass satellites. Finally, the fraction of orphans relative to the total satellite population increases with the extent of tidal disruption of satellites.

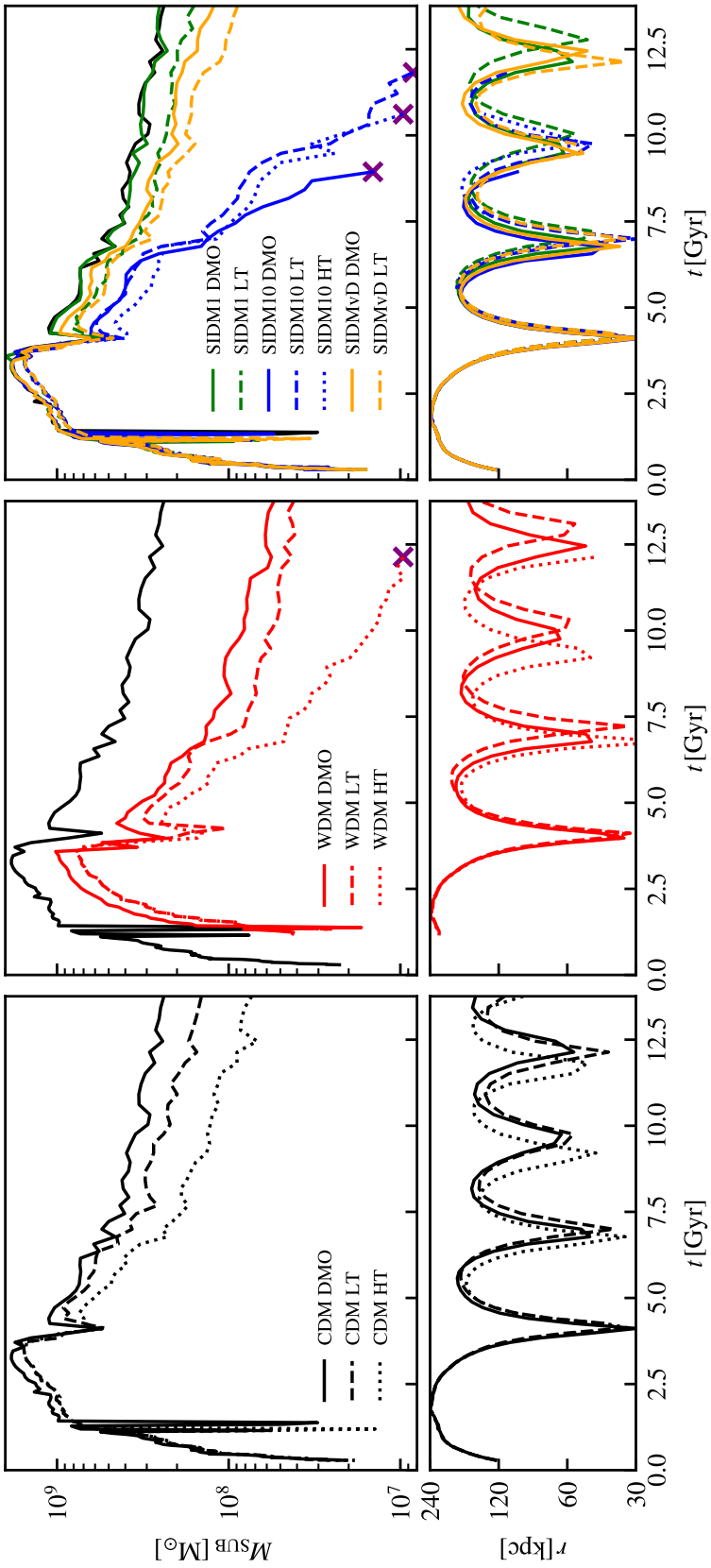

Figure 3.10: Time evolution of the total bound mass (top) and galactocentric distance (bottom) of a $z = 0$ satellite identified in the CDM LT simulation, matched across all simulations. Each column shows the evolution in different DM models: CDM (left), WDM (centre) and SIDM (right), with the colour-coding in the latter indicating the cross-section value, as per the legend. The choice of subgrid physics is represented by the different line-styles. We show the evolution of the CDM DMO satellite in all panels to allow for an easier comparison across models. The counterparts not surviving until $z = 0$ are highlighted by a purple cross at the time when they were last resolved.

3.6 The reason behind the suppression of satellite numbers

We have given a broad overview of how the overall population properties of the $z = 0$ surviving satellies differ across models. In summary, these were variations in the number of satellites and different radial and $V_{\rm max}$ distributions. To investigate the underlying causes for these changes, we now turn to a more detailed comparison of how differences in the dark matter and baryon physics affect stripping, and thus satellite survivability.

For this, we select all satellites in the CDM LT model that are resolved at $z = 0$ and identify their counterparts in the other simulations. We base our selection on this model because it has the largest surviving satellite population at $z = 0$. The matching is done bijectively, as described in Section 3. In short, we identify the time at which the satellite progenitors attained their largest bound mass and cross match the 100 most bound DM particle at that time. This minimises the effects of tidal stripping and potentially diverging evolutionary paths. Moreover, this method is also able to identify counterparts that have been disrupted before $z = 0$.

We are able to find counterparts in the CDM HT and SIDM simulations for $\sim 99\%$ of the $z = 0$ surviving CDM LT satellites. The number of identified counterparts in the WDM simulation is $\sim 88\%$, because the population size is smaller due to the cut-off in the power spectrum.

3.6.1 Different fates for the same satellite

We start by considering the evolution of a single example of a satellite identified in the CDM LT simulation, whose matched counterparts retain similar orbital parameters throughout their existence. This is an important condition when comparing the evolution of a single object across simulations, as small differences in position and velocity near pericentre may lead to very different subsequent orbits and thus the tides they experience. We aim to exclude differences in stripping that are caused by changes to the orbits.

The evolution in galactocentric distance of the chosen satellite is shown in the bottom panel of Fig. 3.10. As expected, we see no differences prior to the first pericentric passage. Afterwards, we observe some minor changes to the orbital phase, but all the counterparts that survived up to $z = 0$ have experienced four pericentric passages since they first entered the virial region of the halo.

Focusing on the evolution of total bound mass, there are very few differences prior to infall. At early times there are transient decreases associated with ongoing mergers, during which SUBFIND switches the subhalo it identifies as the most massive within a FoF group. We see that the peak bound mass for a fixed DM model changes between their hydrodynamical and DMO counterparts. As explained in Section 4, this is caused by the early loss of baryons and subsequent decrease in halo growth due this reduction in mass. Finally, we note the significant delay in the formation of the WDM counterparts, which lowers their peak bound mass relative to their CDM and SIDM equivalents.

The bound mass of satellites decreases continuously after infall into the virial region, with periods of intense stripping occurring near pericentre. These are often accompanied by a peak-trough-peak pattern, caused by a decrease in the tidal radius of these objects near pericentre (and thus the bound mass assigned by SUBFIND). The resulting bound mass is lowered between consecutive apocentres. A measure of how stripped these objects were by any given pericentric passage can be estimated by taking the bound mass ratio of the peaks immediately before and after a pericentric passage.

We do this for the first pericentre, which is when the orbits are most similar across simulations. The CDM DMO, LT and HT versions lost 28%, 41% and 54% of their total mass, respectively. For the WDM we note a similar ordering – but differing magnitude – of stripping: 56%, 63% and 67%. The SIDM counterparts are stripped to varying degrees depending on the cross-section. The lowest value, $1\,\mathrm{cm}^2\,\mathrm{g}^{-1}$, exhibits little difference to CDM, as expected since the structural changes at this mass scale are minimal (see bottom panel of Fig 3.5). All of the SIDM10 versions lose a large fraction of mass, ranging from 60% to 70%. As expected, the stripped mass fraction in SIDMvD lies between the cases for the lowest and highest cross-sections.

The cumulative effect of subsequent pericentres and continuous stripping leads to different subhalo masses at $z = 0$. In come cases, like WDM HT or all of the SIDM10 counterparts, the mass loss causes the subhalo to be disrupted before $z = 0$. For those that survive, we see a clear separation between different cross-section values and whether baryons are present or when cores form due to a high density threshold for star formation.

To check whether the differences of $z = 0$ mass between DMO and hydrodynamic counterparts is due to enhanced stripping or simply caused by a lower peak bound mass, we compute the relative loss of mass, $1 - M(z = 0)/M_{\rm peak}$. For CDM, we measure 84%, 91% and 95% for the DMO, LT and HT versions, respectively. There are no differences for the WDM cases, with both the DMO and LT cases losing 94% of their mass. The SIDM cases do show some differences, but less pronounced than in the CDM case; about a 3 percent increase in the mass loss rate in the hydrodynamical simulation. Note that this comparison does not attribute the increase of stripping in the hydrodynamical simulations to any single origin. Indeed, it can be caused by a combination of the presence of a massive stellar disc, the contraction of the host halo or changes in the satellite density profiles.

3.6.2 Disruption rates

Based on the previous example, as well as on the decrease in satellite numbers in some models even when the number of progenitors is the same, we expect many more satellites to be disrupted before $z = 0$ in the non-CDM LT counterparts. We explore this in Fig 3.11, where we show the cumulative fraction of CDM LT counterparts in other simulations are disrupted before z = 0, as a function of the redshift when they were last resolved. This is only computed for the luminous subset of the matched populations; this does not significantly alter the SIDM and CDM HT numbers, since $\sim$ 96% and $\sim$ 91% of matched satellites are luminous, respectively. The difference in the SIDM case is likely caused by slight differences in the evolutionary histories, since whether or not a halo contains a single bound star particle becomes a stochastic process. In the case of CDM HT the difference stems from a combination of this and the fact that the onset of star formation will occur at later times due to the increase in the density threshold for star formation. Finally, the WDM

luminous matched fractions in the LT and HT versions are 66% and 55%, respectively. This results from the delay in the formation time of the satellite progenitors, which decreases the number of would-be satellites that cross the mass-threshold to trigger the gravitational collapse of gas (as shown by the halo occupation fraction shown in Fig 3.4).

Focusing on the total fraction of disrupted satellites, we observe that more than half of all satellite progenitors in the LT and HT SIDM10 simulations are disrupted before $z = 0$. The lack of a significant difference between the two is likely that the gas density threshold for star formation does not alter the internal structure of these SIDM haloes significantly, unlike models where it is able to turn a cusp into a core. As the cross-section value is lowered, so is the fraction of disrupted satellites: 31% and 18% for the SIDMvD and SIDM1 models, respectively. About a third of all satellites in the CDM HT are disrupted before $z = 0$, likely due to the structural changes caused by gas blowouts. Finally, the low threshold version of WDM loses only a small fraction of the luminous population ($\sim$ 13%). The high threshold version, as in the other cases, exhibits a slight enhancement in disruption rates. We conclude that the decrease in the number of satellites in the WDM cosmologies, compared to SIDM, is largely due to the suppression in the number of galaxies that are able to form.

3.7 Discussion

There are clear differences in the internal structure of dark matter haloes amongst CDM, WDM and SIDM models in DM-only simulations. However, these differences are greatly reduced by the effects of baryons. Depending on the halo mass range, choices regarding the subgrid physics may lead to comparable halo density profiles, as shown in the middle row of Fig. 3.5. The similarity in the density profiles, in turn, leads to similar stripping histories. This results in degeneracies in the way in which baryon effects and the nature of the DM affect the properties of the satellite population. For example, the satellite $V_{\rm max}$ functions in SIDM with velocity-dependent cross-section and in CDM with a high density threshold for star formation are very similar (see Fig. 3.8).

Our analysis thus indicates that the current freedom in the modelling of star formation and feedback in simulations makes it difficult to disentangle their effects from those arising from the nature of the dark matter. Although we have considered only a subset of all the possible model variations, our work suffices to highlight the problem and the current limitations on interpreting observational results. We thus conclude that it will be challenging to constrain the nature of dark matter based solely on the properties of $M_* \geq 10^5\,\mathrm{M}_\odot$ satellite systems.

A promising avenue to explore further is the population of ultra-faint satellites. As shown in the lower row of Fig. 3.5, the effects of baryons become increasingly less important in lower mass haloes, a direct consequence of their low baryonic content (Di Cintio et al., 2014b; Tollet et al., 2016). The internal structural differences in the halos of ultra-faint satellites, driven by the nature of dark matter, are largely preserved in the presence of baryons and affect their resilience to tidal stripping. Therefore, the properties of the ultra-faint population may retain an imprint of the nature of the dark matter. The study of these galaxies requires very high-resolution simulations that can resolve not only the formation of the faintest systems but also track their evolution as they fall into the halo and undergo tidal stripping.

Indeed, adequate numerical resolution is essential to model tidal stripping correctly. Work based on idealised collisionless simulations suggests that cuspy dark matter haloes are resilient to tides and always leave a small bound remnant behind (Errani & Navarro, 2021). However, the limited resolution of cosmological simulations makes this regime difficult to follow, further exacerbated by the fact that the rate of tidal stripping is artificially high for poorly-resolved subhaloes (van den Bosch & Ogiya, 2018). Overall, this amounts to an artificial suppression of subhalo population abundance on a 10% to 20% level (Green et al., 2021), at least based on cold dark matter-only simulations.

Studies comparing the convergence of hydrodynamical cosmological simulations are difficult to conduct, due to a combination of their high computational cost and stochastic changes in the satellite orbital properties and host galaxy ones. Nonetheless, Grand et al. (2021) find that for a resolution similar to the ones used here (Auriga L4, $m_{\mathrm{DM}} \sim 2.9 \times 10^5\ \mathrm{M}_\odot$), artificial disruption becomes important for satellites with $M_* \lesssim 2 \times 10^5\,\mathrm{M}_\odot$. Note that

Auriga MW-like galaxies are more baryon-dominated than in EAGLE (e.g. Fragkoudi et al., 2020), and so the timescale on which subhaloes are stripped below the resolution level is likely faster in the former than in the latter (Green et al., 2022). Given their findings, we believe it is unlikely that our main conclusions, which rely on relative comparisons across dark matter and galaxy formation models, are strongly affected by these issues. In essence, studying the overall, rather than relative, abundance ultra-faint satellites and unveiling their constraining power on the nature of the dark matter will thus require very high-resolution simulations.

Our analysis relies on several assumptions. There are also limitations inherent to our simulations. Firstly, our sample selection is based solely on the virial mass of FoF groups at $z = 0$. This criterion does not account for other factors relevant to tidal stripping, such as the mass of the host's stellar component. The reference EAGLE subgrid model underpredicts the stellar mass of MW-mass haloes by a factor of ~ 2 (Schaye et al., 2015). Changes to the subgrid physics alter, to some degree, the resulting stellar masses of individual haloes. However, the average stellar-to-halo-mass relation is insensitive to the models considered here. Thus, we are confident that the relative differences we observe across the average satellite populations are due to structural changes in the subhaloes rather than differences in the central galaxy properties. The numerical resolution of our simulations also plays an important role in our predictions concerning predicting the number and distribution of low-mass satellites, which are likely to suffer from enhanced stripping (and hence disruption), as well a suppression in the initial number of low-mass galaxies that manage to form. These effects, which are difficult to quantify in hydrodynamical cosmological simulations, are likely to affect objects with low masses, accreted at early times and near the centre of the haloes we study.

To ameliorate the concerns driven by limited particle mass resolution in the radial distribution of satellites, we used an orphan model to track disrupted objects as "sub-resolution" galaxies. Nonetheless, this model is derived from convergence studies based on the Millenium I and II simulations. These are collisionless CDM simulations, which means that the effect of baryons, self-interactions and the presence of central density cores are not

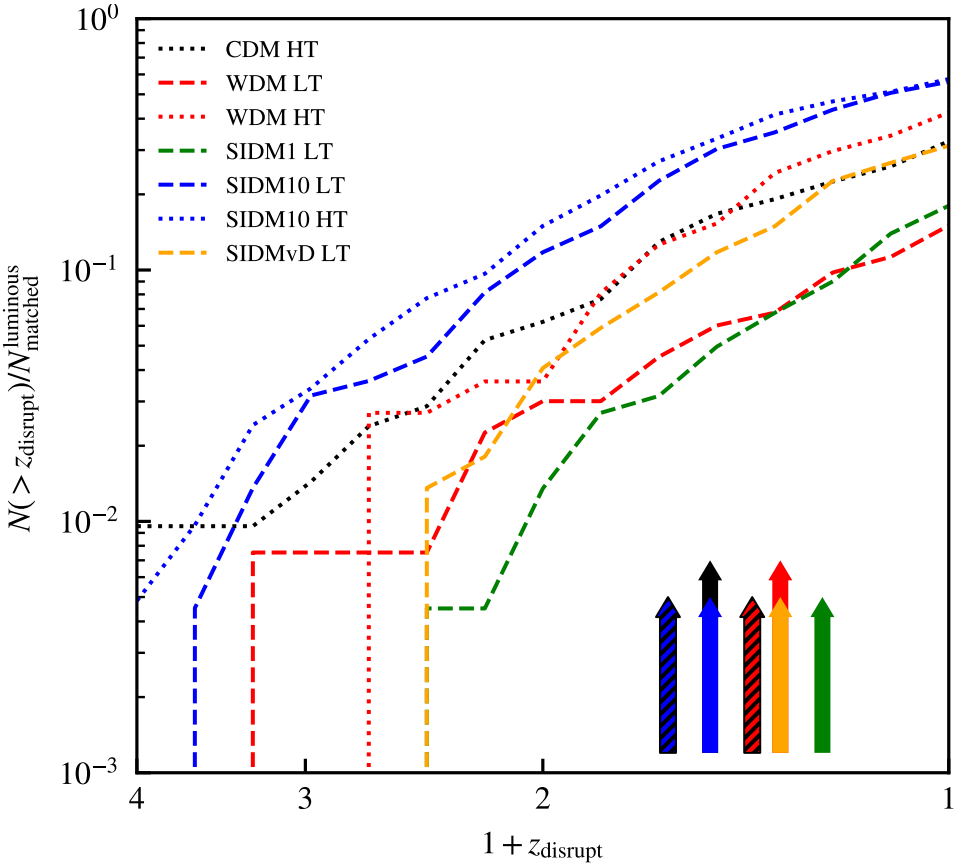

Figure 3.11: Cumulative distribution of the disruption redshifts for the luminous subset of matched satellites, relative to the total number of luminous objects. The colours of each line indicate the DM model as per the legend, with the dashed and dotted ones corresponding to the LT and HT versions' counterparts, respectively. The arrows on the bottom right indicate the redshift at which half of the total disrupted (luminous) population was reached. The hatched arrows correspond to the HT counterparts.

considered. Their dark matter resolution is several orders of magnitude lower (10^9 and 9×10^6 $M_\odot$, respectively) than in the simulations used in this work. This study extrapolates their findings to different DM models and higher mass resolutions. This framework will need to be extended to alternative DM models.

3.8 Conclusions

We have simulated the assembly of haloes with masses within a factor of two from the MW and their satellite systems in a cosmological setting using different dark matter models. They were run on DMO and hydrodynamical simulations via the inclusion of baryonic

physics using the EAGLE subgrid model, which under certain parameter choices, can lead to the formation of baryon-driven cores. This was done with the aim of studying how these changes affect the satellite populations between pairs of matched haloes and identify systematic differences.

Firstly, we saw significant differences at the field halo level across different simulations:

- Low mass haloes in hydrodynamical simulations lose their baryons at early times, leading to delays in their formation time and, correspondingly, lower $z = 0$ virial masses.
- The cut-off in the power spectrum of WDM leads to a smaller number of low mass haloes forming. It also leads to a formation time delay much larger than that caused by baryons. This further suppresses the galaxy population, since the halo occupation fractions change and thus galaxy formation becomes less efficient.
- The density profiles of CDM and WDM are virtually indistinguishable at high masses. They are significantly different at low masses, resulting from different concentrations that reflect their delayed formation times.
- All SIDM haloes show significant differences with respect to the CDM density profiles, due to the formation of cores whose size scales with cross-section value. However, the inclusion of baryons makes the differences less apparent. At high halo masses, this is due to an interplay between self-scatterings and a contraction caused by the central galaxy. At low masses, it is caused by decreases in the overall DM density due to the delay in formation time resulting from slower growth triggered by the loss of baryons. This consequently affects the scattering rate between particles and thus the radius at which haloes are considered to have been thermalised.

All of these changes propagate to the infall properties of satellites, either via a reduction in the accreted number or structural changes that alter their subsequent evolution under the influence of tides.

- The delay in formation time of haloes, either via the loss of baryons, a cut-off in the power spectrum or both, leads to lower bound masses at infall.
- Structural differences across models leads to different stripping rates, which are noticeable even after just one pericentric passage.
- In SIDM, increasing cross-sections lead to larger cores and thus more efficient stripping. At this resolution level, the lowest cross-section value used in this study, $1\,\mathrm{cm}^2\,\mathrm{g}^{-1}$, yields predictions with little to no difference compared to CDM.
- Increasing the density threshold for star formation allows the gas to accumulate in larger quantities before being blown out via supernovae feedback. This results in greater gravitational coupling to the DM, allowing it to flatten the inner DM density profile as its removed. This leads to more efficient stripping relative to their cuspy counterparts. The effect is minor in SIDM models, since haloes already have flat inner density profiles due to DM self-scattering.

The above changes lead to a suppression in the number of satellites at $z = 0$ and lower V_{max} values for those surviving. In SIDM, this is solely caused by the enhanced stripping as a consequence of their flat inner DM density profiles. The lack of satellites in WDM is almost entirely attributable to less haloes (and galaxies) forming in the first place. Models in which gas blowouts are able to flatten the density profiles of haloes also show a suppression in satellite numbers, even in CDM and WDM. In some cases, they lead to entirely degenerate satellite system properties, such as the stellar mass distribution in CDM with baryon-driven cores and velocity-dependent SIDM.

In summary, despite differences amongst dark matter models in DM-only simulations, the presence of baryons can erase the differences arising due to the nature of the dark matter. Our analysis demonstrates that the study of the satellite population in the mass range of $M_* \geq 10^5\ \mathrm{M}_\odot$ is unlikely set informative constraints on the nature of the DM. The lack of constraining power of massive satellites, however, does not rule out the possibility that less massive systems, particularly ultra-faint dwarfs, could be sensitive to the properties

of the DM. Understanding and quantifying these constraints will require the development of dedicated, extremely high-resolution cosmological simulations, an endeavour worth pursuing.

Fourth Chapter

Stellar haloes as a probe of the nature of the dark matter

4.1 Introduction

Many galaxies are surrounded by an extended stellar halo that is largely made up of its most metal-poor stars, which are themselves distributed both as coherent features in chemo-dynamical space and a kinematically hot, smooth component. The nearest example is the stellar halo of the Milky Way, which is one of the few sufficiently close for it to be resolved into individual stars and hence provides a unique laboratory to investigate its detailed properties.

These stars are characterised by two distinct populations (Nissen & Schuster, 1997; Fulbright, 2002), one which formed within the Milky Way proto-galaxy (Belokurov & Kravtsov, 2022) and disc (*in-situ*; Purcell et al. 2010; Cooper et al. 2015), with the latter component being subsequently kinematically heated. The other population seems to have formed beyond the Milky Way and was later accreted, based on its distinct chemical signature compared to the Milky Way stellar population.

The existence of an ex-situ component within stellar haloes is a natural consequence of the hierarchical build-up of structure in a ΛCDM universe (Bullock & Johnston, 2005; Read et al., 2006a). Objects formed in the vicinity of more massive galaxies are able to be accreted onto the latter, where gravitational tides strip their stars onto the surrounding halo (Searle & Zinn, 1978). It is therefore expected that the present-day properties of stellar haloes bear the imprint of the mass assembly history of their host galaxies, as well as reflect the properties of accreted and disrupted objects based on their 'cannibalised'

remains (Bullock & Johnston, 2005; Johnston et al., 2008).

For the Milky Way, precision astrometric and spectroscopic surveys such as GAIA (Gaia Collaboration et al., 2016a,b, 2018, 2023), APOGEE (Majewski et al., 2017) and H3 (Conroy et al., 2019) have strengthened earlier claims (Chiba & Beers, 2000; Nissen & Schuster, 2010) concerning a major merger that occurred ∼10 Gyr ago (Belokurov et al., 2018; Helmi et al., 2018), suggesting it experienced a relatively quiescent evolution since then. The effects of such large mergers result in density breaks within the stellar halo (Deason et al., 2018; Genina et al., 2023), as well as clearly discernible patterns in the velocity distribution (Mackereth et al., 2019; Belokurov et al., 2023), action-space (Myeong et al., 2019; Feuillet et al., 2020; Lane et al., 2022) and chemical abundances (Das et al., 2020) of stars. Less extreme merger and accretions events are nonetheless detectable, both as stellar streams (Johnston et al., 1995; Helmi & White, 1999) and clusters in action and energy space (Koppelman et al., 2019; Naidu et al., 2020)

Beyond the assembly histories of their host galaxies, the large spatial extent of stellar haloes make them powerful tracers of the underlying gravitational potential (Johnston et al., 1999). On large scales, this can be used to constrain the mass (Deason et al., 2021), shape (Bovy et al., 2016) and distortions (Erkal et al., 2021) of the dark matter halo that surrounds the Milky Way. On smaller scales, dynamical perturbations caused by substructure can create gaps in streams (Ibata et al., 2002) and wakes in stellar haloes (Buschmann et al., 2018). Their magnitude and frequency are sensitive to the subhalo mass function (Erkal & Belokurov, 2015), and its orbital distribution (Erkal et al., 2016), both of which are affected by changes to the nature of dark matter (e.g. Lovell et al., 2014; Nadler et al., 2021). Nonetheless, these probes are also sensitive to the potential of the central galaxy itself (e.g. the Milky Way stellar bar; Pearson et al., 2017)

To this day, only a few studies have considered the effect of dark matter models on the properties of stellar haloes beyond small-scale perturbations. Deason et al. (2022) explored how the stellar haloes of dwarf galaxies changed as a result of a cut-off in the power spectrum of density perturbations. The interest in this mass range reflects the expectation that the progenitors of these stellar haloes are strongly affected by said cut-off, whereas the haloes

in larger mass galaxies will have suppressed differences owing to the small contribution of the low mass objects towards the overall properties of the stellar halo.

Whilst using the stellar haloes of dwarf galaxies may connect its properties to the existence of low-mass progenitors in a more direct way, this approach also presents other challenges. For example, the details of galaxy formation in low-mass galaxies remain uncertain, affecting predictions concerning the number of haloes expected to host galaxies (e.g. Jethwa et al., 2018; Graus et al., 2019; Benitez-Llambay & Frenk, 2020) and how massive their stellar components should be (e.g. Brook et al., 2014; Read et al., 2017; Garrison-Kimmel et al., 2017). Additionally, if the stellar mass-halo mass relation has larger scatter at low masses, it will make their individual assembly histories more important (Rey et al., 2019).

Beyond theoretical considerations, detecting stellar haloes around dwarf galaxies remains a considerable observational challenge. Nonetheless, a number of extended stellar components have recently been identified around dwarfs in the Local Group (e.g. Chiti et al., 2021; Waller et al., 2023; Sestito et al., 2023a; Cerny et al., 2023). However, these often rely on a small sample size of associated stars, and a number of different processes are able to place in-situ stars on such extended orbits, like tidal interactions (Sestito et al., 2023a,b), outside-in formation (Benítez-Llambay et al., 2016), orbital expansion induced by bursty supernovae feedback (Waller et al., 2023) or orbital stirring (Kazantzidis et al., 2011).

It is, therefore, important to consider whether the stellar halo around more massive galaxies bears the imprints of the nature of dark matter. As discussed in the previous chapter, changing the dark matter model significantly affects the present-day properties of the satellite systems around Milky Way-mass haloes. In warm dark matter, this is primarily driven by a lower number of low-mass galaxies that form and, hence, to less accreted material. For SIDM, the differences manifest as a result of structural changes, which lead to enhanced rates of tidal stripping and disruption. As the stellar halo is built from the remnants of these galaxies, lowering their numbers, as well as when and where they disrupt (Amorisco, 2017), might result in observable differences in the properties of the stellar haloes.

Addressing this question is particularly timely, given the ongoing and upcoming surveys that will target the stellar halo of our Galaxy and those surrounding external Milky Way-mass galaxies, such as WEAVE (Jin et al., 2023), DESI MWS (Cooper et al., 2023) and Vera Rubin LSST (Ivezić et al., 2019). The larger sample size will provide a way of studying the average properties of stellar haloes around Milky Way-mass galaxies and, hence, be less dominated by the atypical assembly history of our own (Evans et al., 2020). This is a crucial step towards using them as dark matter probes since the stochasticity in their assembly histories leads to changes comparable to those caused by alternative dark matter models (Power & Robotham, 2016). Additionally, the outer stellar halo is likely to be more sensitive to the suppression of small-scale structure, as the most massive progenitors dominate the inner $\sim$ 50 kpc (Fattahi et al., 2020) and their imprints are less likely to be affected by the internal processes of the host galaxy.

To explore how strongly the stellar halo properties depend on the nature of the dark matter, we study eight different Milky Way-mass galaxies formed within high-resolution hydrodynamical simulations based on the EAGLE model of galaxy formation. The only changes across the three cosmological simulations we consider in this work concern the nature of dark matter. This allows us to study the same set of stellar haloes in their cold, warm and self-interacting versions, decoupling the effect of different assembly histories for different counterparts of the same Milky Way-mass haloes.

This chapter begins by introducing the simulations and galaxy formation model we used in this study, followed by the operational definitions we use to identify stellar haloes. In Section 4.3, we explore the present-day masses of these stellar haloes, how realistic they are, and whether they are sensitive to the nature of dark matter. We then proceed to investigate their spatial and dynamical properties, which are more sensitive to changes in the dark matter model, in §4.5. Lastly, we discuss how differences in the progenitors of the stellar halos have given rise to the observed changes in the $z = 0$ stellar haloes.

4.2 Simulations

In this section, we describe the code, galaxy formation physics prescriptions used in our simulations, and our implementations of alternative dark matter models.

4.2.1 The code

The EAGLE project (Schaye et al., 2015; Crain et al., 2015) is a suite of hydrodynamical cosmological simulations that follow the formation and evolution of cosmic structure from ΛCDM initial conditions assuming the cosmological parameter values from Planck Collaboration et al. (2014). They were performed using a modified version of the P-Gadget3 code (Springel, 2005) that incorporates subgrid prescriptions for the physics relevant to galaxy formation and evolution: radiative cooling and photoheating (Wiersma et al., 2009), star formation and evolution (Schaye, 2004; Schaye & Dalla Vecchia, 2008), stellar feedback (Dalla Vecchia & Schaye, 2012), black hole seeding (Springel et al., 2005a; Booth & Schaye, 2009), its subsequent growth and stochastic, thermal AGN feedback.

The values of the parameters used in modelling these processes were set by requiring a good match to the observed $z = 0.1$ galaxy stellar mass function, the distribution of galaxy sizes and the amplitude of the central black hole mass *vs* stellar mass relation. Once calibrated in this way, EAGLE reproduces a number of population statistics (Schaller et al., 2015; Ludlow et al., 2017).

We use the calibration made for the higher mass resolution version of EAGLE to simulate structure formation in a periodic volume of $(12\ \mathrm{Mpc})^3$. We populate it with 2×512^3 particles, half of which are dark matter and the rest gas particles. This corresponds to a particle mass resolution of $\sim 4\times10^5$ and $\sim 8\times10^4\ \mathrm{M}_\odot$, respectively. The initial conditions were generated using MUSIC (Hahn & Abel, 2011).

4.2.2 Warm dark matter

We obtain the power spectrum of WDM, $P_{\rm WDM}(k) = T^2(k)P_{\rm CDM}(k)$, using the transfer function of Bode et al. (2001):

$$T^2(k) = [1 + (\alpha k)^{2\nu}]^{-5/\nu} \,. \tag{4.1}$$

Here, ν is a fitting constant equal to 1.2 and the parameter α depends on the assumed mass of the WDM particle:

$$\alpha = 0.049 \left[\frac{m_{\rm th}}{\rm keV}\right]^{-1.11} \left[\frac{\Omega_{\rm WDM}}{0.25}\right]^{0.11} \left[\frac{h}{0.7}\right]^{1.22} h^{-1}\,{\rm Mpc}\,. \tag{4.2}$$

For this work we assume $m_{\rm th} = 2.5\,{\rm keV}$. This is lighter than the equivalent thermal relic mass of a 7 KeV sterile neutrino model associated with the unidentified 3.5 KeV X-ray line (Boyarsky et al., 2014). Nonetheless, we chose this value to enhance the differences with respect to CDM to allow for an easier comparison. We can estimate the mass scale where the differences with respect to CDM are noticeable, $m_{1/2}$. It corresponds to the Jean's mass of a perturbation with a wavelength equal to the one where the WDM power spectrum is half of the CDM one. For the values used in this work, $m_{1/2} = 1.4 \times 10^9\,{\rm M}_\odot$.

4.2.3 Self-interacting dark matter

Self-interactions are modelled using the Monte-Carlo implementation described in Robertson et al. (2017). Dark matter particles can scatter each other when they are closer than the Plummer-equivalent softening length of the simulations. The probability of any two neighbouring particles scattering is a function of their relative velocity and the assumed cross-section. In this study, we use an isotropic cross-section of 10 $\rm cm^2 g^{-1}$

4.3 Methods

4.3.1 Structure finding and merger trees

To identify cosmic structures, we assign particles into distinct groups according to the friends-of-friends (FoF) percolation algorithm (Davis et al., 1985). Each group is made up of particles that are within 0.2 times the mean interparticle separation from one another. Gravitationally bound substructures are found with the SUBFIND algorithm (Springel et al., 2001), which, using particle velocity and position information, identifies self-bound structures within a larger FoF group.

We follow the time evolution of all SUBFIND groups using their merger trees, which are built by cross-matching a subset of the most bound particles between consecutive time outputs (Jiang et al., 2014). This implementation is able to link SUBFIND groups that have temporarily disappeared from the catalogues (e.g. due to insufficient density contrast near centres of more massive haloes) for five consecutive data outputs or less. The main progenitor branch is then found by identifying the progenitor branch with the largest integrated mass (De Lucia & Blaizot, 2007). This reduces the influence that halo switching, prone to occur during major mergers, has on the identification of the main progenitor at high redshifts.

4.3.2 WDM spurious group removal

Particle-based simulations starting from a density perturbation power spectrum with a resolved cut-off produce spurious structures along filaments. This is a consequence of the discrete representation of the underlying density field (Wang & White, 2007). Consequently, this results in an artificially high number of objects below the mass scale where no structure is expected to form.

In this study, we remove them from the WDM simulations using the two criteria of Lovell et al. (2014). Firstly, we remove all groups whose peak bound mass is below the mass scale

at which the number of spurious groups equals genuine ones, $M_{\rm lim}$. This is related to the mass resolution of the simulation and the assumed power spectrum via:

$$M_{\rm lim} = 5.05\,\bar{\rho} d k_{\rm peak}^{-2}, \tag{4.3}$$

where d is the mean interparticle separation, $k_{\rm peak}$ the wavelength at which the dimensionless power spectrum, $\Delta^2(k)$, peaks and $\bar{\rho}$ the mean density of the universe. For the simulations and WDM model used in this study, $M_{\rm lim} = 1.4 \times 10^8$ M$_\odot$.

Finally, we select the particles bound to the group when the group first reached half of its peak bound mass. We then compute the inertia tensor of those particles in the initial conditions and define the sphericity as the ratio between the smallest and largest eigenvalue of their inertia tensor, $s \equiv c/a$. All groups with $s \leq 0.16$ are removed since the Lagrangian regions associated with spurious groups are significantly more flattened than those in which genuine haloes form.

4.3.3 Identification of the stellar halo

Identifying the stellar haloes within simulations is not straightforward, as there are different ways of doing so. Some rely on cuts based on the spatial (e.g. Monachesi et al., 2019) and circularity distribution of stars (e.g. Font et al., 2011), and others do so based on whether they have been accreted from other galaxies (e.g. Fattahi et al., 2020). Choosing a particular definition reflects the questions one wants to address, which in our case concerns whether the changes in the progenitors of the stellar halo, induced by different dark matter models, result in detectable differences. As such, we define the stellar halo as being composed solely by stars formed beyond the central galaxies within the Milky Way-mass haloes in our sample.

In practice, reliably identifying which stars have formed in-situ and which ones have been accreted is not trivial. For instance, the concept of a dominant 'main progenitor' becomes less well-defined at high redshifts, and even high-mass ratio mergers at low redshifts can lead to central misidentification, blurring the boundary between ex-situ and in-situ components.

Our initial selection of stars to analyse is done at $z = 0$, by identifying all stellar particles within the FoF groups hosting our sample of MW-mass haloes. To prevent including in our analysis the stellar component of resolved satellites, we further require that particles are classified as bound to either the MW subgroup (i.e. the most massive subgroup of the FoF group) or unbound. This results in a population that includes stars formed within the MW and those originating from the orbital debris of previously-accreted galaxies. Since we are interested in the latter, we need to further clean this sample.

We have explored two alternative ways to select ex-situ stars, based on either their radial distance to the Milky Way main progenitor (e.g. Sanderson et al., 2018) or whether they were bound to it (e.g. Fattahi et al., 2020), both measured when the star formed. Although the formation time of each stellar particle is precisely known, only discrete outputs in time contain information about their spatial position or structure membership. This entails either using the output immediately following their formation, or the one just before they form, relying instead on the information concerning the gas particle that will subsequently become the star.

By comparing the above methods, we find a cleaner identification of the ex-situ component based on the subgroup membership of the gas particle preceding its conversion to a star particle. We identified several progenitor galaxies that continued forming stars during sub-30 kpc pericentric passages, which were likely triggered by the compression of gas by its tidal interaction with the host (Genina et al., 2019). As such, the spatial criterion would have misidentified stars during these occurrences. The choice between the star or gas-based particle selection was based on visual inspection of the resulting in-situ components, with the former being more contaminated by ex-situ material than the latter.

4.4 Ex-situ masses

We start by examining whether the stellar haloes in our simulations are realistic based on their stellar mass. In Fig. 4.1, we show how the ex-situ mass varies across our halo sample, whose average is in broad agreement with observational estimates of the Milky Way (ex-

situ) stellar halo mass (e.g. Deason et al., 2019). There is a significant halo-to-halo scatter, reflecting the important role that the assembly history has on the mass of the stellar halo. Some differences are also likely to exist based on the mass range we used to select Milky Way-mass haloes, which lie between $5 \times 10^{11} \leq M_{200} \leq 2.5 \times 10^{12}$ M$_{\odot}$.

We note that observational estimates of the stellar halo of the MW are subject to assumptions and observational limitations that make comparisons to simulations less clear cut (e.g. Sanderson et al. 2018). For example, Deason et al. (2019) classify red giant branch stars into disk and halo populations based on GAIA DR2 proper motions, and it can therefore include an in-situ component whose kinematics are difficult to distinguish from the largely ex-situ halo. Moreover, a density profile to volume correct for completeness is also required, which in the above case is based on an Einasto fit to the inner 40 kpc of the halo (based on Deason et al., 2011), which is then extrapolated out to 100 kpc. Lastly, assumptions concerning the average metallicity of the stellar halo, as well as the choice of initial mass function and stellar evolution models can further affect the final estimated stellar halo mass. Overall, these assumptions typically amount to changes in the estimated MW stellar halo mass of up to 40% (density profile), 55% (average metallicity) and 10% (stellar evolution model) in Deason et al. (2019).

The ex-situ mass, $M_{\rm exsitu}$, relative to the total stellar mass within a spherical aperture of 30 kpc, $M_{\rm tot}$, is nonetheless typically larger ($M_{\rm exsitu}/M_{\rm tot} \sim 0.2$) than the Milky Way ($M_{\rm exsitu}/M_{\rm tot} \sim 0.01$; Deason et al. 2019), which is consistent with predictions based on other simulation suites (e.g Monachesi et al., 2019). This discrepancy is primarily driven by an under-prediction of galaxy stellar masses for haloes with $M_{200} \sim 10^{12}$ M$_{\odot}$ in the EAGLE model of galaxy formation, boosting the values of $f_{\rm exsitu}$ despite being consistent in terms of absolute mass. Nonetheless, we find that two of the galaxies with the most quiescent evolutions in our sample have much lower ex-situ mass relative to their overall stellar content, and hence are in better agreement with the real MW estimates – although still larger by a factor of a few. This is in line with other studies that find that the low ex-situ mass fraction observed in the MW requires the build-up of its stellar halo to have occurred early on during its evolution (e.g. Fig. 13 of Deason et al. 2019), rather than the

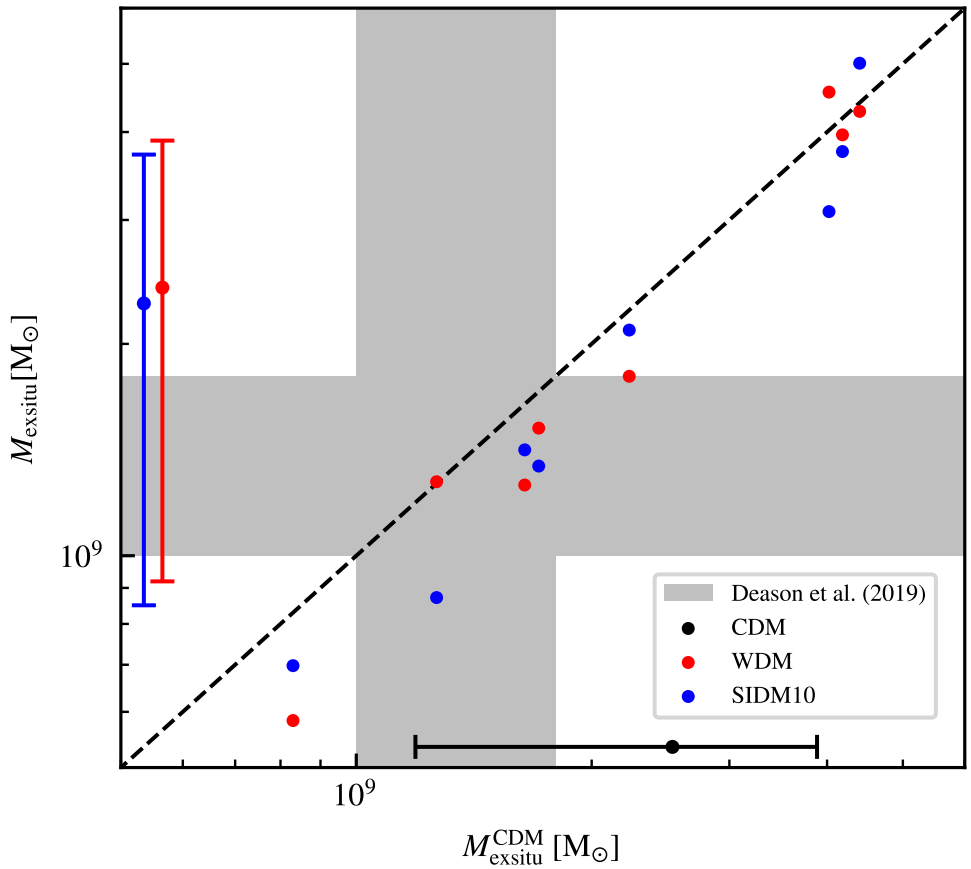

Figure 4.1: Measured ex-situ masses for the eight MW-mass haloes in our sample. Their mass in the CDM versions is indicated by the marker position along the x-axis, whilst its value for the corresponding counterparts in WDM (red) and SIDM (blue) are shown across the y-axis. The average ex-situ mass for each simulation is shown by the markers with error bars, with the latter indicating one standard deviation. The grey bands correspond to the estimated halo mass of the Milky Way based on Deason et al. (2019).

later assembly experienced by a typical MW-mass halo.

It is worth noting that, as explained previously, we have not considered the in-situ component of the stellar halo. As such, our estimate likely corresponds to the lower bound of the total stellar halo mass. Given that we observe morphological changes in the SIDM galaxies compared to their CDM and WDM counterparts, it will be worth exploring in future work whether the in-situ stellar halo in SIDM cosmologies is systematically larger that those in CDM ones. This could be caused by more efficient heating of in-situ stars during mergers, resulting from the shallower potential well of the central galaxies.

Fig. 4.1 also shows how changing the nature of the dark matter modifies the predicted

mass of ex-situ component. Similarly to CDM, their mass is consistent with that found for the Milky Way. This reflects the fact that none of the alternative dark matter models considered here produce significant changes in the mass of the stellar halo, aside from a small systematic decrease.

We conclude that the ex-situ mass of stellar haloes is insensitive to changes in the nature of the dark matter. The two main drivers behind its overall properties are the assembly histories of their host haloes and the way in which one populates the stellar mass function, both in an absolute ($M_{\rm exsitu}$) and relative way ($f_{\rm exsitu}$). Neither warm nor self-interacting dark matter significantly alter either of them on the scales corresponding to the largest progenitors, which dominate the mass budget of the halo. It is therefore unsurprising that the stellar halo mass remains unchanged.

Nonetheless, warm dark matter suppresses and delays the formation of low mass galaxies, which lowers the overall number of accretions. Self-interacting dark matter alters the internal structure of dark matter haloes, making them more easily stripped and disrupted, accelerating the deposition of stars in the stellar halo with respect to CDM. Both of these differences might result in imprints that are relegated to the detailed spatial, dynamical and chemical properties of stellar haloes. We explore whether this is the case for the first two in the following section, with the chemical imprints left as future work.

4.5 Phase-space distribution

We begin exploring the spatial distribution of ex-situ stars by measuring how their mass density varies with radial distance to the centre of the halo. This was calculated using 30 logarithmically spaced bins between 1 and 300 kpc, measured from the centre of the host dark matter halo. For the remainder of this subsection, we define the centre and reference frame of the host dark matter halo based on the mass-weighted position and velocity of all dark matter particles within 5 kpc from the potential centre identified by SUBFIND.

The top panel of Fig. 4.2 shows how the median density profile of Milky Way-mass haloes vary across the dark matter models we consider in this work. They have similar shapes

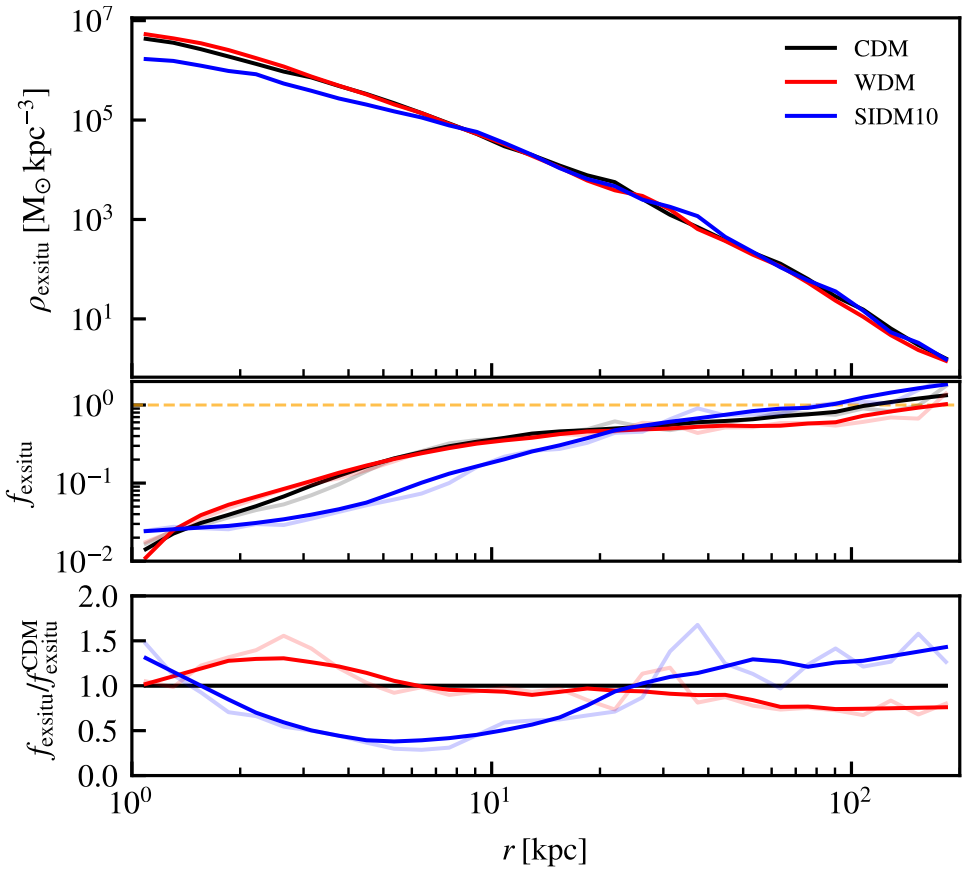

Figure 4.2: *Top panel*: median density profiles of the ex-situ stellar component around MW-mass haloes in CDM (black), WDM (red) and SIDM (blue). *Middle panel*: median radial dependence of the ex-situ component, relative to the in-situ component. Semitransparent lines correspond to absolute values, and solid lines to values that have been smoothed using a running average algorithm. *Bottom panel*: same as the middle panel, but expressed relative to the ex-situ fraction found in the CDM version.

in the outskirts of the stellar halo, but show noticeable differences in the inner tens of kiloparsecs. In particular, the haloes that form in self-interacting dark matter simulations are, on average, noticeably flatter than their CDM and WDM counterparts.

By fitting a power law of the form $\rho \propto r^{\alpha}$ to the average density distribution within 10 kpc, and using as uncertainties the standard deviation of the densities measured at each radial bin, we obtain $\langle\alpha_{\rm CDM}\rangle = -2.12 \pm 0.06$, $\langle\alpha_{\rm WDM}\rangle = -2.28 \pm 0.06$ and $\langle\alpha_{\rm SIDM}\rangle = -1.70 \pm 0.04$. The uncertainties in the average slope were estimated by using the corresponding diagonal entries of the covariance matrix of the fit. Thus, the SIDM profiles are flatter than the CDM counterparts, even if the halo-to-halo scatter is included in the fit. These values also

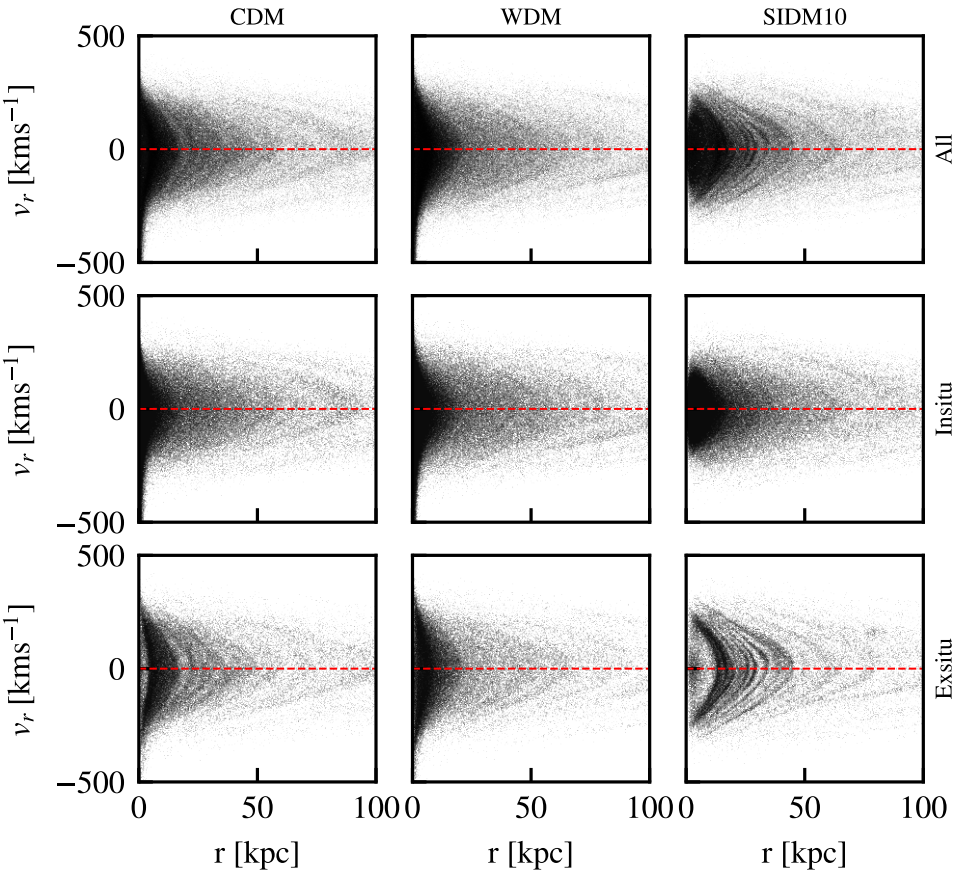

Figure 4.3: Radial velocity of stellar particles as a function of their radial distance to the centre of their host galaxy, shown for a $z = 0$ halo across its CDM, WDM and SIDM versions, as indicated on the top of each column. The in-situ and ex-situ subsets of stellar particles are shown in the middle and bottom rows, respectively

suggest that the WDM are somewhat steeper than in CDM, which will be discussed later in this section.

The observed flattening in SIDM could be driven by the shallower potential in the inner dark matter density profile that resulted from self-interactions. This would cause an overall expansion of the stellar component, both in-situ and ex-situ, and hence not reflect the changes in the assembly of the stellar halo itself. Indeed, we do observe a decrease in the central in-situ density in SIDM compared to CDM and WDM, but as we argue below, the changing central potential is not the sole cause behind the observed differences.

To show this is the case, we measure how the local ex-situ mass fraction relative to the in-situ one, $f_{\mathrm{exsitu}} = M_{\mathrm{exsitu}}/M_{\mathrm{insitu}}$, changes with respect to the radial distance to the centre

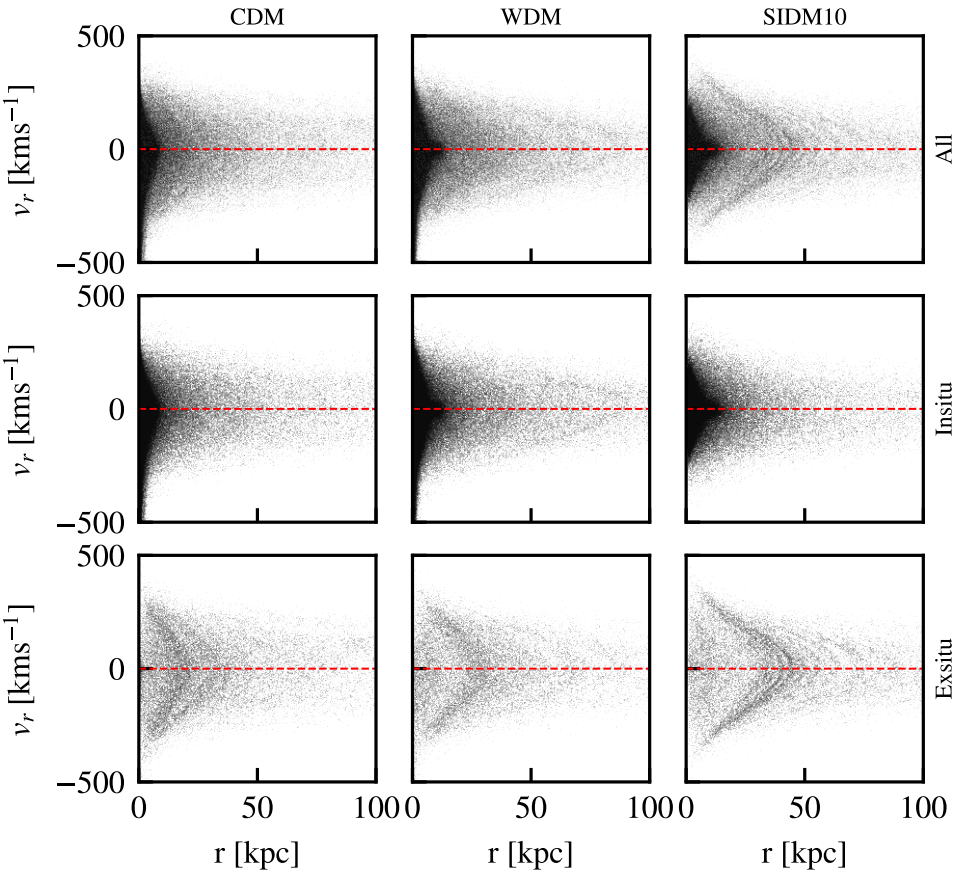

Figure 4.4: Same as Fig. 4.3, but with less prominent substructure in the stellar halo.

of the dark matter halo. The median values measured across our sample are shown in the middle panel of Fig. 4.2, with its running average indicated by the solid lines. As expected, the ex-situ component is only dominant in the outer parts of the stellar halo, with $f_{\rm exsitu}(10\,{\rm kpc}) \sim 0.37$, 0.36 and 0.22 in the CDM, WDM and SIDM10 haloes, respectively.

The shape of the ex-situ fraction in SIDM is substantially different to CDM or WDM, with its ex-situ fraction within ~25 kpc significantly lower. The differences between dark matter models become even clearer once the ex-situ fraction of each model is expressed relative to the one found in CDM, as shown the bottom panel of Fig. 4.2. Indeed, we see that the SIDM ex-situ fraction is suppressed by up to 70%, and remains lower for much larger radii than the spatial extent of the flat-density cores that form in these MW-mass haloes (see Fig. 3.5).

Aside from the changes present in the self-interacting model we consider here, the ex-

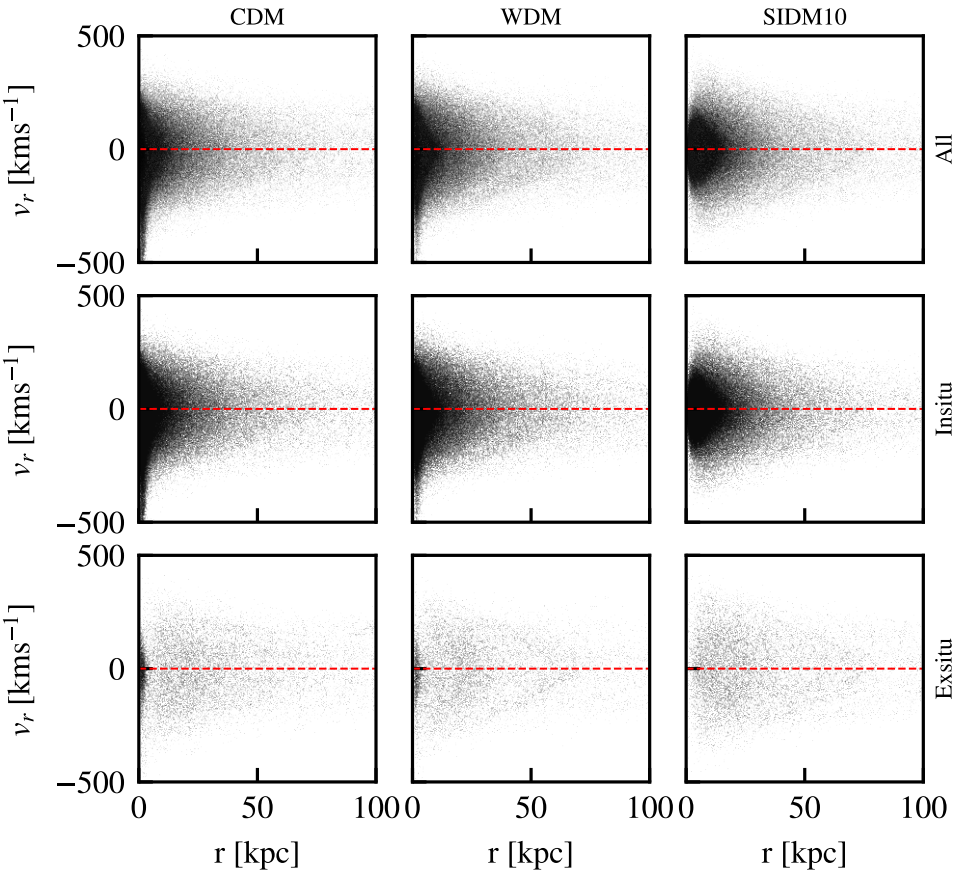

Figure 4.5: Same as Fig. 4.3, but with no prominent substructure in the stellar halo.

situ component in WDM also shows measurable differences relative to CDM. Similarly to SIDM, these are mostly confined within the inner halo, but result in an enhancement of its density within ∼7 kpc, rather than its suppression. Indeed, this fact was already evident from the inferred steeper profiles based on fitting a power law to the inner density distribution. This finding is in qualitative agreement with the more concentrated WDM stellar haloes discussed in Power & Robotham (2016).

We thus confirm that the relative distributions of ex-situ and in-situ material vary depending on the dark matter model. For SIDM (WDM), the inner regions of the stellar halo are less (more) massive than in CDM, with up to a 72% (55%) suppression (enhancement) within 10 (7) kpc. The decrease (increase) suggests a rearrangement of ex-situ material so as to become less (more) concentrated, a fact also suggested by its increased (decreased) dominance in the outer halo.

Beyond the spatial distribution of stellar haloes, another observable that might be also affected by the nature of dark matter are the velocity distributions of its stars. These encode the contribution of major accretion events and individual stripping episodes, and so changing the efficiency of stripping or the number of accretions and mergers might be reflected in the number of phase-space features, as well as how prominent they are.

In this ongoing work, we have so far examined how the radial velocity of stars varies as a function of their radial distance to their host. This is shown for three different representative examples taken from our sample in Fig. 4.3, Fig. 4.4 and Fig. 4.5, which are sorted based on how prominent the features present in this velocity space ('chevrons') are.

Focusing on the first two, it is clear that the amount of structure varies according to the dark matter model, with WDM having the fewest and SIDM having the most. The thickness of each individual chevron also changes with the dark matter model, with the thinnest ones present in SIDM. In line with our findings concerning the spatial distribution of the stellar halo, the SIDM chevrons are typically found at larger radii than the other two models.

By inspecting the assembly of their stellar haloes across DM models, it is clear that, despite experiencing the same accretion events at the same time, the subsequent merging timescale – here defined as time elapsed between the first infall and when the object was last resolved – is different across DM models. For the example of Fig. 4.3, the object responsible for the latest major merger was accreted at $t_{\rm u}$ ~5.76 Gyr, which then took 4, 4.3 and 3.2 Gyr to disrupt in the CDM, WDM and SIDM10 simulations, respectively. Similarly, the largest contribution to the stellar halo of the example shown in Fig. 4.4 took 3.2, 3.5, 3.0 Gyr to merge in CDM, WDM and SIDM10, after being accreted at $t_{\rm u} \sim 4.71$ Gyr. Consequently, the amount of pericentres and dynamical friction these objects have experienced before merging differs, resulting in different normalisation and scatter for the orbital energies of the ex-situ component. The former affects its spatial distribution, whereas the latter results in changing chevron morphology since it reflects the spread in energies when stars are stripped.

The last example represents a stellar halo with no prominent features in any of the dark

matter models. This galaxy experienced a relatively quiescent evolution, reflected in the low mass of its ex-situ component. Doing the same exercise as above, we found that the object responsible for the last major merger was accreted at $t_u \sim 1.9$ Gyr. As such, any previously existing chevron – which would be difficult to adequately sample due to the resolution of this simulation – would have been stretched out, blending into the surrounding background, and hence leading to a featureless distribution like the one observed here. This suggests that the most informative haloes concerning the nature of dark matter are the ones that form later, which are also the most massive ones. This could have important implications for the usefulness of stellar halo of our Milky Way as a dark matter constraint, which we will address in future work.

In summary, both the spatial and velocity distribution of the ex-situ components depends on the assumed dark matter. To understand the reason why different models result in changing properties, it is crucial to investigate how the properties of its building blocks vary, both prior to being accreted (e.g. peak mass), and during stripping and merging (e.g. stellar deposition radii).

4.6 The building blocks of stellar haloes

The dynamical and spatial differences of present-day stellar haloes reflect the properties of accreted objects and the host assembly history. Given that we have considered the same sample of Milky Way-mass haloes, whose counterparts share the same overall assembly histories, the relative differences must be due to changes in the population of accreted haloes. Indeed, as discussed in the previous chapter, the changes lead to different amounts of accreted substructure, how much disruption occurs, and also when they disrupt (e.g Fig. 3.11).

To find which galaxies contributed to the build up of the stellar haloes in our sample, we identify all structures whose main merger tree branches eventually merge with the main progenitor of the Milky Way. We note that this criterion also includes any objects that were disrupted whilst orbiting a galaxy that would subsequently be accreted onto the virial

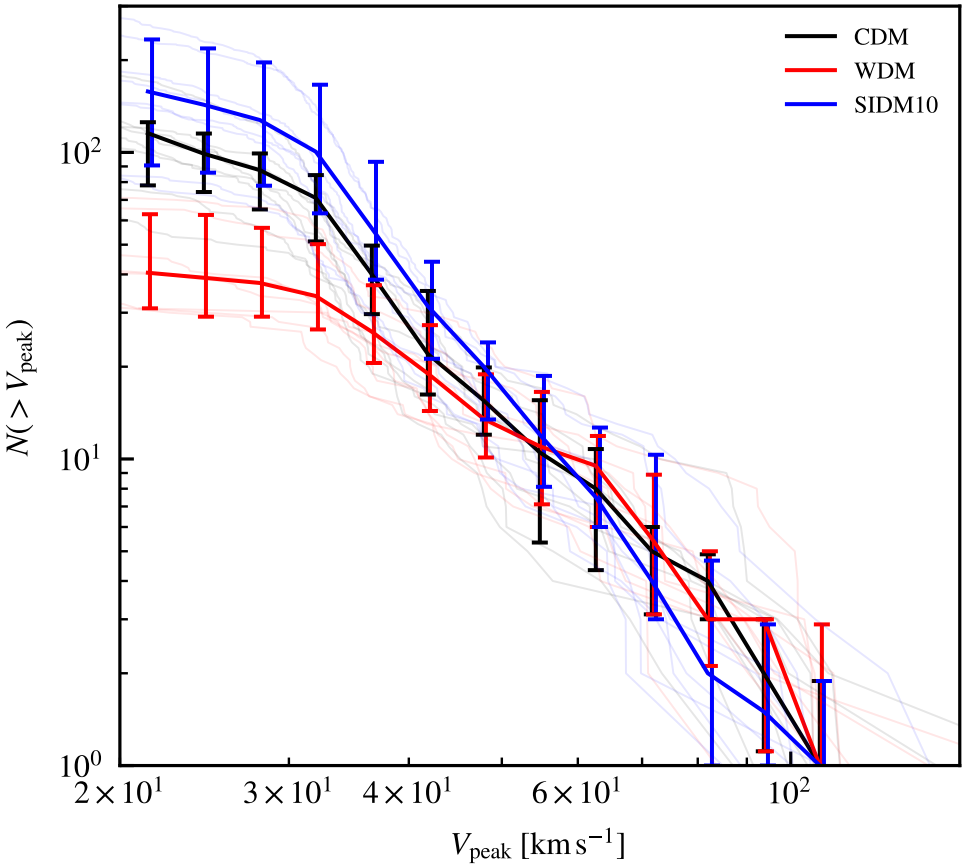

Figure 4.6: Distribution of the peak maximum circular velocity of subgroups whose merger tree branches eventually merge with the MW-mass haloes in our simulation, which we take as the build blocks of their stellar halo. This is shown across different DM models, as indicated by the top right legend. The lines and associated error bars, which have been horizontally shifted for legibility, indicate the 16th, 50th and 84th percentiles of the distribution in each $V_{\rm peak}$ bin

region of the MW-mass haloes we study here, but these belong to the low-mass end of the population. We begin by showing in Fig. 4.6 the $V_{\rm peak}$ function of the population we find, which is a good proxy for halo mass, and hence stellar mass. We find the value of this quantity by identifying the highest value of the circular velocity, $V_{\rm max}$, that the subgroup had before it was no longer present in the halo catalogues.

Focusing on the total number disrupted objects, we note there are significant changes across dark matter models. The lowest number corresponds to a WDM model, where the suppression reflects lower numbers of galaxies forming (both due to less haloes forming and lower occupation fractions; see §3), and hence discrete contributions to the build-up

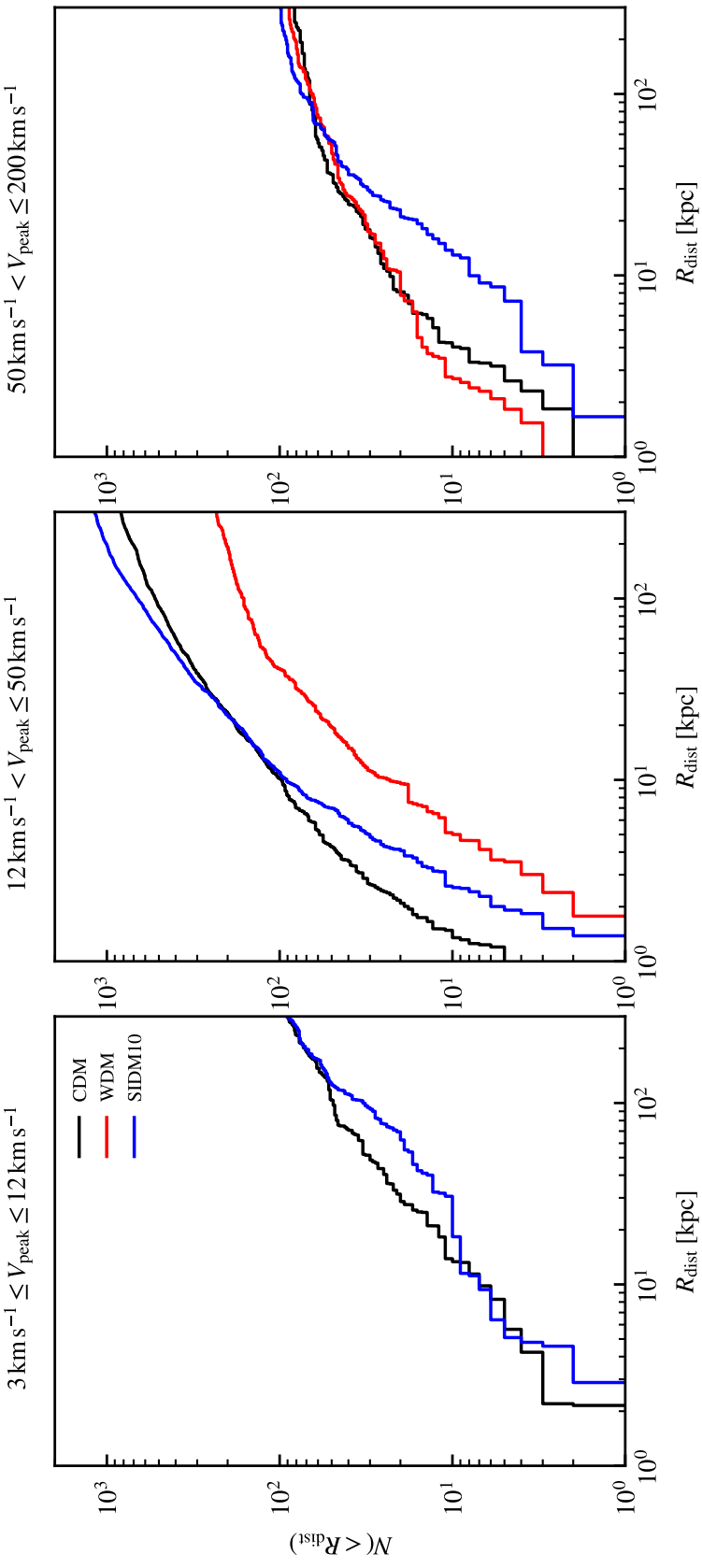

Figure 4.7: Disruption distance of the halo building blocks to the MW-mass halo onto which they deposit their stars. This is shown in three different V_{peak} bins, which were chosen to approximately split the CDM population into their 10% least and most massive progenitors (left and right), and the remainder (centre).

of the stellar halo. The largest number of disruptions occur in SIDM10, which forms the same amount of structure as in CDM (their power spectra are the same), but the structural changes result in more efficient stripping.

Nonetheless, the differences discussed in the previous section concern the inner region of the stellar halo, and so are likely to be driven by its most massive progenitors. However, no significant differences are present in this mass range across models, which are all consistent within their 1σ scatter. This is perhaps unsurprising, due to the fact that their disruption is driven by a merger with the central galaxy, rather than tidal stripping. As the models we have used here primarily affect their internal structure of sugroups, or the masses of less massive ones (e.g. Fig 3.2), the total masses of the largest contributors are unaffected, and so the efficiency of dynamical friction and how much mass they deposit remains similar.

However, the changes could have indeed affected the evolution of these objects prior to disruption. For example, a galaxy that experiences more tidal stripping whilst sinking towards the centre of its host, will result in stars with higher energy orbits and less circular orbits compared to one that is not as easily stripped. This will subsequently alter the orbital distributions of the stars, and hence their spatial and dynamical distribution.

As such, we investigate what the typical distance to the Milky Way main progenitor is when progenitor galaxies disrupt. We use this in lieu of more accurate methods that require potential modelling to integrate their orbits to estimate the true orbital parameters of stars. We believe this metric, though approximate, is sufficient to capture the major trends in the population we study here.

Since the mass of the progenitor is also important in determining how many stars are placed at a given distance, we measure the distribution of disruption distances across three different sub-samples of the progenitor population, classified according to their $V_{\rm peak}$. The limits used to identify each sub-sample are approximately based on the 10% and 90% percentiles of the total CDM $V_{\rm peak}$ distribution, defining low, intermediate and high mass progenitor bins (below 10%, between 10% and 90%, and above 90%, respectively). The resulting distributions are shown in Fig 4.7.

The distributions are significantly different across $V_{\rm peak}$ bins and dark matter models. A trend persistent across these bins is the less concentrated distributions of the SIDM progenitor subgroups, with the normalisation comparable to CDM on the larger mass bin, but higher on the intermediate one. This suggests that the number of contributions towards the build up of the halo through dynamical friction is the same in CDM and SIDM. However, the contributions based on tidal disruption are greater in SIDM, reflecting that CDM galaxies are more resilient to tidal stripping.

As most of the mass of the stellar halo is contributed by the upper $V_{\rm peak}$ bin, the fact that SIDM progenitors typically disrupt at larger radii (and earlier times, see Fig. 3.11) means they have experienced less overall dynamical friction before disrupting. Consequently, their stars have more extended orbits and thus the stellar haloes in SIDM are less concentrated.

The distribution of disruption distances for WDM progenitors have similar shapes to CDM in the intermediate $V_{\rm peak}$ bin, but less contributions due to less accreted galaxies. Interestingly, the most massive contributions seem somewhat more concentrated than in CDM, which could explain the central enhancement of the ex-situ material in WDM models, as discussed earlier. Power & Robotham (2016) attribute similar findings to an on-average increase of the dynamical friction that massive progenitors experience, which is supposedly caused by their increased bound mass, as a reflection of lower amounts of mass in substructure. Although this might seem a plausible explanation to what we observe, we believe this warrants further investigation. This will be done in upcoming work.

4.7 Conclusions and future work

We have used simulations of the assembly of Milky Way-mass haloes in a cosmological environment to explore the effect that the nature of dark matter has on the properties of their accreted stars. The original simulation suite, initially run to study the satellite systems of Milky Ways, included a variety of dark matter models and galaxy formation physics. In our initial step towards understanding the connection between their stellar halo and the nature of dark matter, we have opted for the use of the subset that enhances the predicted

differences across models: galaxy formation is unable to create flat density cores in dwarfs, and we use the highest self-interaction cross-section ($10\,\mathrm{cm}^2\,\mathrm{g}^{-1}$) out of the available SIDM models.

Using all accreted stars as our definition of the stellar halo, we find that the masses found in our sample of eight Milky Way-mass haloes is, on average, consistent with that of our own Galaxy. This is true regardless of whether the dark matter is cold, warm or self-interacting, and so the stellar halo mass is insensitive to its nature.

We do however find a dependence of the spatial distribution of the stellar halo on what dark matter model we assume. This primarily concerns its inner parts, with the average density profile slope within 10 kpc being steeper (shallower) in WDM (SIDM) than in CDM. Consequently, the ex-situ fraction of stars in the inner parts shows an average enhancement (suppression) of up to 55% (72%) in the former (latter).

Beyond density profiles, the velocities distributions of stars show suppressed (enhanced) substructure in WDM (SIDM) compared to CDM. The prominence and number count of the associated chevrons appears to be dependent on the assembly history of each individual halo. As such, finding differences between DM models based on this metric alone becomes more difficult for earlier forming, less massive stellar haloes.

To understand the causes behind the above differences, we identified all galaxies that eventually deposited their stars on the stellar haloes we study. As expected, the lowest number of individual contributions occurs in WDM, reflecting the suppression in the amount of galaxies that form and hence accretions. On the other hand, SIDM haloes suffer from enhanced tidal stripping, and so a larger number of them contribute toward the build up of stellar halo.

However, these changes are relegated to the low-mass end of accretion spectrum, as their most massive ones remain similar throughout the three models. The main difference thus appears to be how quickly their most massive progenitors merge and get stripped from their stars. In SIDM, the radial distribution of disruptions is the least concentrated of the models considered here. Together with their faster disruption times, this likely means

the apocentres of the stripped stars have larger values than those formed in the CDM counterpart, leading to a less concentrated stellar halo. For WDM, the cause might be stronger dynamical friction, as originally proposed by Power & Robotham (2016). We will however check whether this is the case in future work.

In summary, our findings highlight a new potential way to constrain the nature of dark matter, based on the stellar halo of Milky Way-mass galaxies. Beyond the differences discussed here, there are others observables which we have not considered and could be similarly affected, such as the radial anisotropy, two-point correlation function in phase-space, clustering in action space, and metallicity slopes. Given ongoing and upcoming efforts towards studying the stellar halo Milky Way and those of external Milky Way-mass haloes, this exciting prospect warrants further investigation. We conclude by noting several limitations of this study, and how they will be addressed in future work.

Firstly, we have considered simulations in which the predicted differences between dark matter models are exacerbated, i.e. no flat-density core formation through gas blowouts in dwarf galaxies. As shown in the previous chapter, this process can mimic the effects of SIDM on the satellite population, and could therefore similarly affect the most massive stellar halo progenitors and thus its final properties. This possibility will be explored by using the remaining suite of simulations presented during the previous chapter. Secondly, we have used relatively extreme variations in the nature of dark matter, and so follow-up work should consider versions that are more consistent with current observational constraints. Lastly, our comparisons between dark matter models do not include observational uncertainties. This means that the differences we identified in this work may not be observable in the real Universe. As such, mock observations should be made based on these simulations, to enable a fairer comparison to real data.

Fifth Chapter

The time and spatially resolved population of galactic subhaloes across dark matter models

5.1 Introduction

Around 85% of the total matter energy-density in our Universe is made up of dark matter (Planck Collaboration et al., 2020b), making it a crucial ingredient in our understanding of how cosmic structure forms. Based on theoretical expectations arising from extensions to the Standard Model of Particle Physics, such as supersymmetry (Wess & Zumino, 1974), dark matter is commonly assumed to be made of massive, weakly interacting particles, known as cold dark matter (CDM).

The CDM model predicts a hierarchical growth of structure, with small-scale overdensities being the first to undergo gravitational collapse. Larger structures do so later, subsequently growing in mass through a combination of smooth mass accretion and mergers with neighbouring structures. The end result of this process is the formation of dark matter haloes with density profiles that follow a smoothly varying power law (e.g. NFW or Einasto; Navarro et al. 1995; Einasto et al. 1974) and characteristic densities that reflect the mean density of the Universe when they formed (Navarro et al., 1997).

Another consequence of structure formation in CDM is that dark matter haloes are predicted to contain a substantial amount of substructure (e.g. Springel et al., 2008). These initially formed in the vicinity of their host and were subsequently accreted onto it. The most

massive ones quickly sink to the centre due to dynamical friction (Chandrasekhar, 1943), but the lowest mass ones remain as self-bound substructures and subsequently evolve under the effect of the tidal field of their host. As such, the properties of the subhalo population initially reflect those found in the field, with their present-day properties determined by the integrated efficiency of tidal stripping.

The number of accreted subhaloes is connected to their overall number density, which is itself dependent on the matter power spectrum of density perturbations. The nature of dark matter affects its amplitude and shape by smoothing out density fluctuations on scales smaller than its free-streaming scale. As this is related to its initial velocity distribution, the amount of structure that forms is dependent on the nature of dark matter. For a thermal relic, the scale increases with decreasing dark matter particle mass.

Once a halo is accreted by a larger host, its evolution is largely driven by tidal stripping. Its efficiency depends on the structural and orbital parameters (e.g. Peñarrubia et al., 2010; Errani & Navarro, 2021), which reflect how tightly bound the subhalo is and the strength of the tidal field it experiences, respectively. As such, differences in the density profile of subhaloes that have the same orbital parameters lead to diverging evolutionary histories and, hence, different final properties.

Large-scale observations constrain the suppression of structure below massive galaxies, consistent with predictions based on CDM models. In fact, viable particle candidates are sufficiently massive that the suppression of structure only occurs below Earth masses (Hofmann et al., 2001). Consequently, structures form on all astronomically relevant scales, and hence, a CDM universe is inherently ‘clumpy’ (Jenkins et al., 2001).

Nonetheless, this entails extrapolating large-scale constraints to the highly non-linear small-scale regime. Well-motivated dark matter models that differ from CDM, like a 7 keV sterile neutrino (Boyarsky et al., 2014, 2015), are consistent with CDM on large scales but differ in their predictions concerning the abundance of small-scale structures (Lovell et al., 2014). It is thus necessary to focus on understanding the smallest scales to further constrain the nature of the dark matter. This has motivated searches for signatures of the suppression of

structure on small scales: perturbations in strong gravitational lensing (Vegetti et al., 2010, 2012), reionisation-limited HI clouds (Benítez-Llambay et al., 2017b), stellar stream gaps (Ibata et al., 2002), dwarf galaxy stellar haloes (Deason et al., 2022), etc.

A complementary approach is to focus on dwarf galaxies, which are predicted to be the most common type of galaxies in the Universe. They represent the smallest scales where galaxy formation can occur (Jethwa et al., 2018; Graus et al., 2019; Benitez-Llambay & Frenk, 2020), and are therefore the most dark matter-dominated luminous systems. This makes them ideal laboratories to test the nature of dark matter. This is reflected in their centrepiece role within the small-scale challenges of CDM, which were/are tensions between predictions and observations concerning their abundance (Kauffmann et al., 1993; Klypin et al., 1999; Moore et al., 1999), distribution (Lynden-Bell, 1976; Kroupa et al., 2005; Ibata et al., 2013; Martínez-Delgado et al., 2021) and structural parameters (de Blok, 2010; Oman et al., 2015).

Many are too faint to be detected beyond the Local Group, with the closest comprising the satellite system of the Milky Way. Indeed, many of its constituents have remained undetected until recently (e.g. Drlica-Wagner et al., 2015; Mau et al., 2020; Cerny et al., 2021a,b, 2023), but surveys such as DES (The Dark Energy Survey Collaboration, 2005) and DELVE (Drlica-Wagner et al., 2021) have allowed the characterisation of the MW satellite population at an unprecedented depth. As changing the nature of dark matter alters the density profiles and abundance of dark matter haloes, both of which affect the present-day population of subhaloes surrounding MW-mass haloes, the properties of the Milky Way satellite system provide a powerful test bench on our understanding of the dark matter.

However, as discussed in §3, galaxy formation can mimic the effects of alternative dark matter models. For example, sufficiently strong and bursty gas blowouts are able to turn an initially steep density profile into one with a flat-density core (Navarro et al., 1995; Read & Gilmore, 2005), leading to similar changes as those predicted by alternative dark matter models. Given the uncertainty in how star formation should be modelled and whether gas blowouts are able to flatten the density profile of dwarf galaxies, one cannot use galaxies

where gas blowouts can potentially affect them to make a definitive statement about the nature of dark matter.

The effectiveness of supernovae-driven flat-density cores is nonetheless predicted to be dependent on halo mass (Di Cintio et al., 2014a; Tollet et al., 2016). Those with masses $\geq 10^{11}\,M_{\odot}$ have enhanced central densities resulting from the contraction induced by the central galaxy, whereas the baryonic content in the lowest mass haloes is insufficient to result in significant structural differences, regardless of the details of how galaxy formation is implemented (e.g. Benítez-Llambay et al., 2019). As such, only dwarf galaxies in a narrow range of mass, those corresponding to classical satellite galaxies, can effectively mimic the effects of alternative dark matter models.

It is, therefore, possible to circumvent the degeneracies caused by galaxy formation by using ultra-faint galaxies. These are interesting objects in their own right since they probe the limits of galaxy formation and are likely relics from the epoch of reionisation. For the purpose of dark matter studies, the unaltered distribution of its dark matter halo allows a more direct connection to the inferred structural changes due to different dark matter models.

Following the evolution of structure at these small scales is challenging since their low masses translate into a numerical high mass resolution to resolve their formation and subsequent evolution. Recent hydrodynamical simulations have managed to simulate the formation of ultra-faint galaxies (e.g. Rey et al., 2019; Gutcke et al., 2022), but these are selected from isolated populations, hence not representative of the environment where ultra-faint satellites form and evolve.

Cosmological simulations that follow the evolution of the Milky Way and its satellite system have a much lower mass resolution, regardless of whether they are dark matter only or include galaxy formation. This means that the formation of the lowest mass satellites is not resolved (Grand et al., 2021), and even if it is, their subsequent tidal evolution is prone to numerical limitations resulting from flat-density cores caused by artificial two-body relaxation.

The extent of these issues in cosmological simulations has been highlighted in recent work (van den Bosch & Ogiya, 2018), and there is growing consensus that haloes with density cusps never disrupt, at least based on idealised simulations (Peñarrubia et al., 2010; Errani & Navarro, 2021). As such, much of the disruption in simulations appears to be a combination of limited amounts of particles used to identify the smallest structures, and artificially enhanced tidal stripping (Green et al., 2021). Consequently, predictions reliant on accurately following the tidal evolution of subgroups, like those concerning the satellite system of the Milky Way, are severely limited by inadequate resolution.

Methods to address these limitations exist based on the so-called 'orphan' or 'type II' galaxies. These are models that treat the remnants of disrupted subhaloes as sub-resolution objects, with their subsequent evolution based on models that can include dynamical friction, tidal stripping or tidal disruption. Their inclusion in simulations reproduces predictions based on higher resolution simulations (Guo & White, 2014; Newton et al., 2018), and results in better agreement with analytical predictions and observations on small (Bose et al., 2020) and large scales (Wang et al., 2006).

The implementation details vary, and similarly to semi-analytical models, they often rely on several free parameters that need to be calibrated (e.g. Jiang & van den Bosch, 2016; Simha & Cole, 2017; Nadler et al., 2019). This has been done in a variety of ways, such as statistical matching of subhalo properties across resolutions or based on idealised high-resolution numerical experiments.

In short, despite ultra-faints representing a powerful tool to constrain the nature of the dark matter, they are poorly resolved objects in realistic cosmological simulations, biasing predictions about their population. Although orphans ameliorate some of these problems, their models have been tested in idealised setups or environments not representative of the Milky Way. The natural question is, hence, whether these are accurate in realistic cosmological simulations, and ultimately, what is the true ('converged') distribution of subhaloes hosting ultra-faints around the Milky Way, and how it varies across dark matter models.

Resolution Level	$M_{\rm highres}$ [$\mathrm{M}_\odot$]	$N_{\rm highres}$	$N_{\rm tidal}$	IC file size [GB]
Au6-L5	3.50×10^6	1.19×10^6	2.62×10^6	0.143
Au6-L4	4.37×10^5	9.54×10^6	5.07×10^6	0.514
Au6-L3	5.47×10^4	7.63×10^7	2.60×10^7	3.477
Au6-L2	6049	6.90×10^8	2.45×10^8	31
Au6-L1	756	5.52×10^9	1.77×10^9	245
Au6-L0	95	4.41×10^{10}	1.40×10^{10}	1905

Table 5.1: Summary of the mass resolution of the simulations we propose to run, as a function of their assigned 'resolution level'. The number of high resolution and tidal particles, as well as the storage footprint, were obtained after generating the initial conditions (IC).

To address these concerns, we are currently working on a project to perform the highest-resolution simulation to date of a Milky Way-mass galaxy. This simulation will consider a dark matter particle mass of 95 $\mathrm{M}_\odot$. This will be done using a dark matter-only zoom-in both in CDM and the 7 keV sterile neutrino WDM model. This will provide accurate predictions concerning the subhalo population and its evolution, providing a realistic environment to verify the 'tidal tracks' derived from idealised simulations. When coupled to a semi-analytical model of galaxy formation, this will return the total number of predicted of Milky Way satellites, without having to resort to orphans.

In this chapter, we will discuss the preparations towards this objective. This involves identifying a code that can handle the extreme density contrasts in these zooms and selecting a halo representative of the one that hosts our Milky Way. Shortly before the submission of this thesis, we have applied for computing time to run these expensive simulations.

5.2 Simulations

In this section, we present an overview of the software we will use for running the simulations, what are the outputs (and storage) requirements to address the questions posed above, and which Milky Way-mass object we will simulate.

5.2.1 The code

The extreme dynamic range involved in running zoom-in simulations requires good load balance across parallel tasks to enable adequate scaling when running the simulation in state-of-the-art computing facilities. Given this, we choose to use the state-of-the-art cosmological code GADGET-4 (Springel et al., 2021). The newest iteration of GADGET includes a new array of improvements that improve scalability and code accuracy. It additionally includes tools that are particularly well suited for the extreme zoom-ins simulations we aim to run. For example, it allows placing a smaller mesh around the zoom-in region, speeding up long range PM-based gravity calculations that would be achieved based on the global mesh, since each of its cells is typically larger than the whole region of interest.

5.2.2 Output requirements

An additional choice relevant to our study is how often we want to save information concerning the distribution of substructure. For the studies we want to do, it should be as often as possible, to accurately identify the pericentric radius of the orbits of substructure. Idealised simulations have found that this is an important parameter, since the density contrast between the subhalo and the host halo at pericentre sets the maximum amount of stripping it can experience (e.g. Errani & Navarro, 2021).

Simulations which do not have sufficient time resolution have to resort to orbit interpolation and integration to estimate when and how close pericentric passages occur, introducting some level of uncertainty (e.g. Sawala et al., 2016; Richings et al., 2020). As such, we choose to output substructure information every ~ 10 Myr below $z = 2$, generating almost 1500 outputs through the whole simulation. This is sufficient to not have to rely on interpolations or orbit integration.

5.2.3 Identifying a representative halo

The highest resolution dark matter-only simulation of a Milky Way-mass halo is part of the Aquarius simulation suite (Springel et al., 2008), which was run over 15 years ago and, hence, uses WMAP cosmological parameters (Spergel et al., 2003). The halo simulated at the highest resolution level, Aquarius-A, is very concentrated, and hence not representative of the average Milky Way-mass halo (Ludlow et al., 2014) nor our own (Cautun et al., 2020). This affects the properties of the subhalo population through a combination of earlier accretion times and stronger tides caused by a denser host halo (Nadler et al., 2023).

As such, we focus our efforts towards simulating the Auriga-6 halo (Grand et al., 2017), which has updated cosmological parameters (Planck Collaboration et al., 2014) and a concentration consistent with that of the Milky Way (Callingham et al., 2020). Beyond these criteria, we also select this halo based on the fact that it has already been simulated at one of the highest resolution magnetohydrodynamical simulations of a Milky Way-mass halo ($m_b = 800\,\mathrm{M}_\odot$; Grand et al. 2021). This will enable future comparisons of how tidal stripping differs in the presence of a galaxy disc, which enhances the tidal field strength (D'Onghia et al., 2010; Garrison-Kimmel et al., 2017; Sawala et al., 2017), and whether orphan models derived from DMO simulations are still applicable in hydrodynamical simulations.

The Auriga halo sample is a random subset selected from the most isolated Milky Way-mass haloes ($10^{12} \leq M_{200} \leq 2 \times 10^{12}\,\mathrm{M}_\odot$) found at $z = 0$ in Eagle simulation (Schaye et al., 2015). To generate the ICs, all the particles within $4R_{200}(z = 0)$ are traced back to their original locations in the $z = 127$ initial conditions. The resulting Lagrangian region is sampled at higher resolution, with variable-mass particles placed outside of it to reproduce the overall tidal field of the original cosmological box (Jenkins, 2010). The resulting particle masses, their storage footprints, and resolution level nomenclature are summarised in Table 5.1.

5.3 Substructure finding

The questions we want to address in this project rely on being able to accurately measure the properties of the subhalo population found around simulated Milky Way-mass haloes. As such, an essential step for interpreting the predictions stemming from these simulations is identifying the structures as they form, following their time evolution, and accurately measuring their properties. In practice, doing so is a non-trivial problem.

Finding field haloes has a relatively well-defined approach that uses the friends-of-friends (FOF) percolation algorithm (Davis et al., 1985). This algorithm groups particles within a certain distance from each other, often 20% the mean interparticle distance of the simulation. On the other hand, identifying substructures is a more complicated procedure. This can be understood by considering two previously independent FOF groups that have just been linked as a consequence of the close spatial proximity between their outer boundaries, e.g. when one is an accreted object. Running an unbinding algorithm on the resulting FOF particle distribution will, at best, recover a single-bound object, often the most massive of the two. Nonetheless, this can fail even more spectacularly if the estimated frame of reference used during unbinding (often based on the centre of mass) converges to the unbound background that exists between the density peaks, finding no bound objects at all.

As such, substructure-finding algorithms typically rely on identifying subsets of particles within FOF groups that comprise one or more candidate substructures and then checking whether they are self-bound or not. There are different ways to do this, such as simply using the hierarchical spatial distribution of particles (e.g. More et al., 2011), finding local or spherical overdensities (e.g. Springel et al., 2001; Knollmann & Knebe, 2009), or using the position and velocity information (e.g. Diemand et al., 2006; Behroozi et al., 2013a). All of these different operational choices result in significant differences in the measured properties of the substructure population (Knebe et al., 2011, 2013), as well as computational cost and scalability.

Beyond identifying substructure, following their evolution requires linking them across

consecutive data outputs. Aside from the multiple choices involved in how to match substructure between consecutive outputs, e.g. tracking a subset of the most bound particles (Springel et al., 2005a) or using additional dynamical information (Behroozi et al., 2013b), limitations present during substructure identification further complicate this process. For example, substructure can be temporarily lost from the catalogues for one or more output times, or can fragment if near the resolution limit of the simulation. As such, similarly to substructure finders, different approaches result in different evolutionary histories (Srisawat et al., 2013).

In summary, the measured properties of subhalo populations and their evolution are strongly dependent on the algorithm used to find them and link them. For the purposes of this project, preventing the premature loss of substructure is crucial, since this would bias the predicted galactic subhalo population, inferring larger disruption rates and hence overpopulating substructure catalogues with orphan galaxies.

Given this, we opt to use a particle tracking method to find substructures. This approach consists of identifying sets of associated particles according to some criterion that is implementation-dependent (e.g. Tormen et al., 1998; Han et al., 2018; Mansfield et al., 2023; Diemer et al., 2023), tagging them and retaining their association to identify candidate substructures later in time. The main benefit of these algorithms is to refine the definition of 'source subgroup', which is the set of particles that comprise a substructure candidate that will be subject to gravitational unbinding.

For example, SUBFIND updates the source subgroup continuously based on the density peaks it finds within a FOF group, making it susceptible to completely losing substructure if the density contrast is insufficient. This typically occurs during pericentric passages, as it is unable to find saddle points in the density field. Unless appropriate care is taken when building the resulting merger trees, this will result in disjoint merger tree branches. Even if the subgroup is not lost, the changing spatial extent of the subgroup leads to significant mass fluctuations.

One can, therefore, imagine a more robust method that identifies which particles are

associated with a given structure prior to pericentre and keeps checking for the self-boundness of this grouping, regardless of whether there is a density peak or not. This is the working principle behind particle tracking that allows it to fare better than traditional algorithms, enabling better subhalo convergence properties at the same resolution level (e.g. Springel et al., 2021; Mansfield et al., 2023)

For this project, we have implemented Hierarchical Bound Tracing (HBT+; Han et al. 2018) to work on the fly within GADGET-4, which we refer to as Concurrent Tracking of the Assembly of Particles into Substructure (CTAPS). In the following subsection, we will present the main features of the HBT+ algorithm itself, followed by the details of our CTAPS implementation. Finally, we will discuss what differences exist between our newly-implemented version and 'SUBFIND-HBT', an HBT-inspired substructure finder packaged inside the original public release of GADGET-4 that can also run on the fly.

5.3.1 Hierarchical Bound Tracing

As mentioned before, identifying the set of particles to track in time is implementation-dependent. In HBT+, this is done based on the assumption that structure forms in a hierarchical manner, such that any substructure would have been an isolated structure in the past. The terminology employed throughout the remainder of the text is as follows: group as a Friends of Friends group, subgroup as a self-bound structure, central (subgroup) as the most massive one within group and secondary subgroups the remaining ones within the group.

5.3.1.1 Tracking

In hierarchical structure formation, haloes initially form in isolation but can later be accreted onto neighbouring haloes, where they become part of its substructure population or merge with them. This fact is used by HBT+ to simplify the process of substructure finding, as it relies on identifying haloes when they first form as independent structures, following their

growth and evolution during this initial stage, and if they are accreted, it tracks the particles associated to when it was last independent to identify substructure candidates.

This approach naturally results in the creation of merger trees, as subgroup tracking is done by construction and hence is automatically identifiable with distinct merger tree branches, which we refer to as 'tracks'. In practice, each subgroup is assigned tracer particles sampled from its $N_{\rm tracer}$ (defaults to 1) most bound particles, which are used to identify which FOF group it belongs to and, therefore, whether they have been accreted by a neighbouring structure.

Consequently, more expensive algorithms used to build merger tree branches, like bijectively matching subgroup catalogues to identify progenitors and descendants, are not required. This is also partly because subgroup fragmentation is less common than other approaches, and hence, descendants are better defined. Nonetheless, fragmentation can occur for FOF groups near the resolution limit, a fact addressed in the original version of HBT through 'splinter branches'. In this work we do not consider using splinters, assuming instead that the tracer particles reliably identify the most likely FOF host of a track.

The creation of a new merger tree branch / track, occurs whenever a FOF group contains no tracer particles associated with any previously existing ones. If the newly created track has no bound component, it is discarded; otherwise, a persistent entry with a unique identifier is created. The number it gets assigned reflects the size of its FOF host relative to all other ones with newly found tracks at said time. This allows the group catalogues at each output to be sorted according to this 'TrackID', and therefore, the whole assembly history of a track is quickly recoverable.

5.3.1.2 Central identification

Every track is initially the central of its own FOF group, but this changes if two of them coalesce together. Defining the resulting central establishes the hierarchical relations between its substructure and, hence, which track is able to grow through the smooth accretion of mass. Decisions concerning the central occur when two or more tracks that

were central in the previous output are found in the same FOF group, which signifies an accretion event has taken place.

When this occurs, each central candidate is ranked according to its bound mass in the previous output, $M_{\rm bound}$. The most massive candidate, with mass $M^{\rm max}_{\rm bound}$, is used to define the following mass threshold:

$$M_{\rm large} = f_{\rm threshold} M^{\rm max}_{\rm bound} \, , \tag{5.1}$$

with $f_{\rm threshold} = 0.8$ by default. Any candidate with masses lower than the above is automatically considered a secondary subgroup, with the remaining ones classified as large candidates. If only one large candidate exists, it is automatically chosen as the central.

The presence of more than one large candidate indicates a major accretion event. Correctly identifying the central in such cases is crucial, since a misidentification would lead to significant mass fluctuations at later times, e.g. 'central switching'. To make a physically informed decision, we compute the orbital kinetic energy of each large candidate, defined by the centre of mass position and velocity of the particles that were bound to it in the previous output, in the frame of reference of its host FOF group. The lowest value corresponds to the one moving most like the bulk flow of its host, and hence, it is tagged as the central.

In a minority of cases, particularly close to the resolution limit of the simulation, we find that certain centrals with substructure can suddenly disrupt. If this occurs, the most massive substructure in the group is chosen as the new central.

5.3.1.3 Source subgroup

Defining a source subgroup that is not too small nor too large is essential for robustly finding substructures. Both extremes can lead to finding no bound component at all, either because of the lack of particles, or too many truly unbound particles contaminating estimates concerning the frame of reference. As such, the source subgroup should be able to grow or decrease in size in a way that reflects the evolutionary stage of its bound component, e.g. accreting mass or being stripped.

For centrals, the source is able to grow by the accretion of new particles onto its host FOF group. As such, any particle found in its FOF group that does not already belong to a substructure becomes assigned to it. Additionally, its source is confined to its host FOF group.

Throughout the evolution of tracks, they can lose substantial amounts of mass, particularly once they become a secondary substructure. To prevent its source from becoming too large relative to the bound component, it is kept below a maximum size that is determined by how many bound particles belong to it:

$$N_{\rm source} \leq f_{\rm source} N_{\rm bound} \, . \tag{5.2}$$

Here, $f_{\rm source} = 3$ by default. If the condition is not fulfilled, the least bound particles belonging to the source are assigned to its parent track, if it is a secondary subgroup. This means that the sources of secondary subgroups can grow if they have children.

5.3.1.4 Substructure unbinding

Determining which particles within a source are bound requires specifying a reference frame to estimate their kinetic energies relative to a bulk motion. To include Hubble flow component of the physical velocities, a centre also needs to be specified. In this algorithm, like many others, the mass-weighted position and velocities of the particles belonging to the bound component of the candidate subgroup is used as the centre and reference frame.

The particle unbinding algorithm follows an iterative approach. Starting from all of the source particles, it computes their centre of mass centres and velocities, and thus their kinetic energies. Combining it with their potential energies estimates yields binding energies, and all unbound particles ($E_{\rm binding} \geq 0$) are discarded. This procedure is repeated until the number of bound particles converges.

Substructures in a given group are analysed in a depth-first approach, reflecting their hierarchical nature. As such, particles not bound to a substructure will be considered during the unbinding of its parent, if it has any. However, these particles still retain their

association to their original subgroup, unless they have been removed from the source subgroup as a consequence of the condition (5.2) being triggered.

5.3.1.5 Substructure mergers

Sufficiently massive subgroups experience strong dynamical friction, as the efficiency of this mechanism depends on the mass ratio between the satellite and the host. This drives a loss in the orbital angular momentum of the satellite, causing it to sink towards the centre of the host, where it merges.

However, as shown in Fig 5.1, particle tracking methods are still able to find bound components in these sunken substructures. A bound component is found because it is effectively similar to running the unbinding on a subset of the most bound particles of the host. This can negatively impact the subsequent evolution of its host when using an exclusive mass definition, since it is missing a subset of its most bound particles.

As such, we explicitly check whether two tracks have merged based on the phase-space distance between the parent and its child:

$$\frac{|\bar{\mathbf{x}}_{\rm parent} - \bar{\mathbf{x}}_{\rm child}|}{\sigma_{x_{\rm parent}}} + \frac{|\bar{\mathbf{v}}_{\rm parent} - \bar{\mathbf{v}}_{\rm child}|}{\sigma_{v_{\rm parent}}} < 2\,, \tag{5.3}$$

where $\bar{\mathbf{x}}_i$ and $\bar{\mathbf{v}}_i$ the average position and velocity of particles that comprise the 'core' of the parent and its child subgroup, which are normalised by the standard deviation in the position and velocity of the core of former, $\sigma_{x,v}$. These quantities are estimated using the $N^{\rm core}_{\rm parent}$ and $N^{\rm core}_{\rm child}$ most bound particles of the parent and child subgroups, which default to 20 and 1 particles, respectively.

If a merger occurs, the particles previously associated to the child are assigned to its parent, the merger time is logged and the children of the merged child get their parents reassigned.

5.3.1.6 Disruptions, re-appearances, and low-density structures

Substructure can eventually disrupt if the number of bound particles drops below a given threshold. If this occurs, the subgroup is subsequently treated as an orphan, whereby its

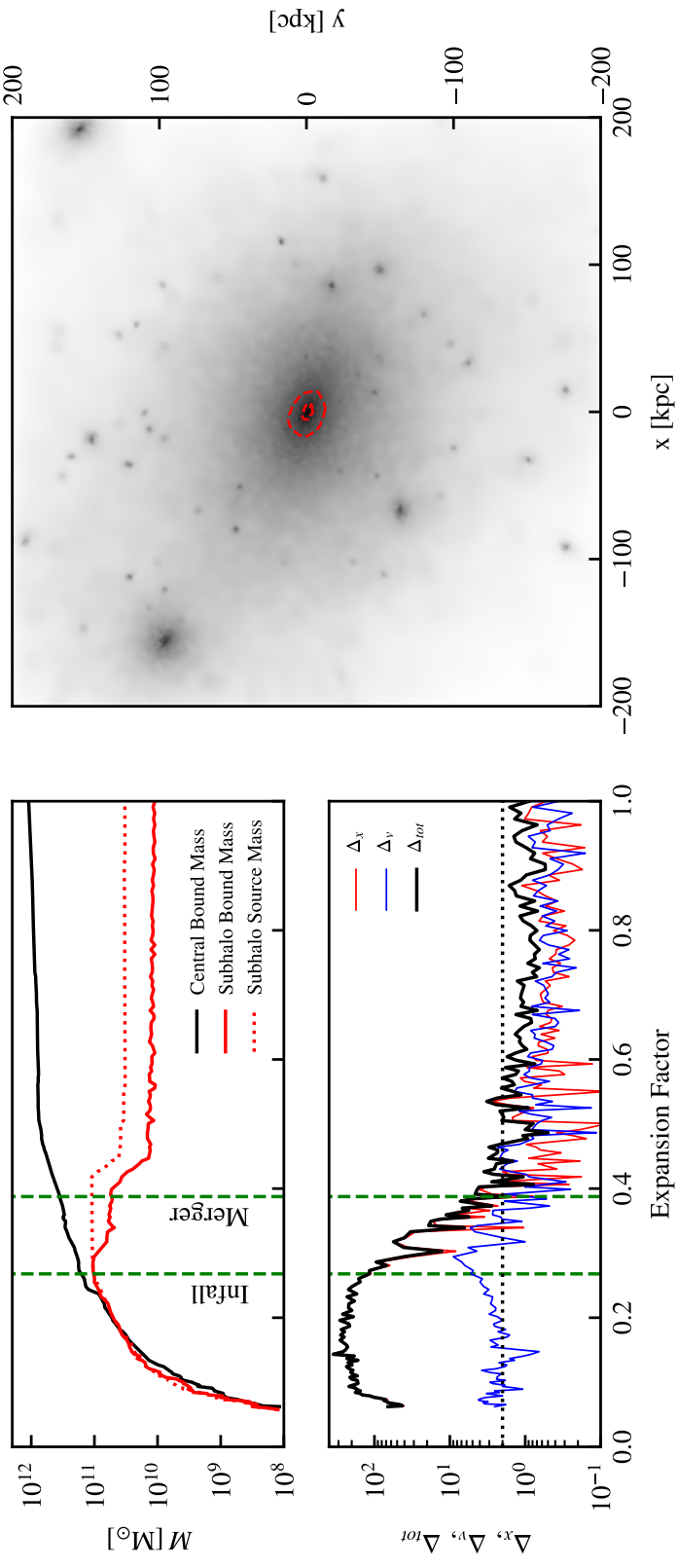

Figure 5.1: Example of a subgroup that merges with the Milky Way progenitor at $z \sim 1.6$, with a mass ratio of $\sim$ 1:1.6 at infall time. *Top left panel:* Time evolution of the bound mass of the MW main progenitor (black) and the merged subhalo (solid red), with the mass associated with the source of latter shown as a solid dashed line. *Bottom left panel:* evolution of the position and velocity offset between the Milky Way main progenitor and the merged subgroup, normalised to the velocity and position dispersion of the 20 most bound particles of the former. The time of merger is identified with the first output when $\Delta_{tot} \leq 2$. *Right panel:* present-day surface density distribution of dark matter around the Milky Way, with the contours enclosing 50% and 90% of the particles identified as bound to the merged subhalo at $z = 0$.

position, velocity and host group are determined solely by the most bound particle when it was last identified as a self-bound structure.

Nonetheless, particle noise caused by the discrete sampling of the density field can also lead to the premature loss of bound centrals when near the resolution limit of the simulation. This is often driven by the temporary classification of a few particles as unbound, causing the structure to drop below the particle threshold limit for detection. This can occur several times, and so it is therefore necessary to account for its possible re-emergence, as it will otherwise lead to the creation of multiple tracks and orphans for the same underlying structure.

This is achieved by checking for any tracer particles in FOF groups, regardless of whether they are associated to a bound or orphaned subgroup. If no tracers associated to pre-existing bound tracks are found, but there is a tracer associated to an orphaned one, the FOF particles are assigned to its source subgroup. If a bound component is found within the source of this track, it is no longer considered disrupted.

Lastly, bound substructure may also exist in low density haloes near the resolution limit. In certain cases, they are dense enough to be associated to a FOF groups but subsequently expand or fragment, dropping below the particle detection threshold. In many algorithms (e.g. SUBFIND, ROCKSTAR), only particles belonging to FOF groups can be part of subgroups, which means the substructure that was hosted in the now non-existing group is automatically considered as disrupted. However, these hostless particles still retain information concerning their prior association thanks to particle tracking, and hence their self-boundness can be explicitly checked, leading to the concept of 'hostless' subgroups.

We show one such example in Fig. 5.2, where we have identified a subhalo that remains hostless for several output times in a test run of the Au6-L5 ($m_{\rm DM} = 3.5 \times 10^6$ M$_\odot$). It is initially associated to a FOF group, enabling the original spawning of the track, and the growth of its source subgroup. It eventually expands, splitting the original FOF group into several fragments of sizes smaller than the detection threshold. This leaves the particles hostless, but since they retain their association to their now hostless track, they can be listed

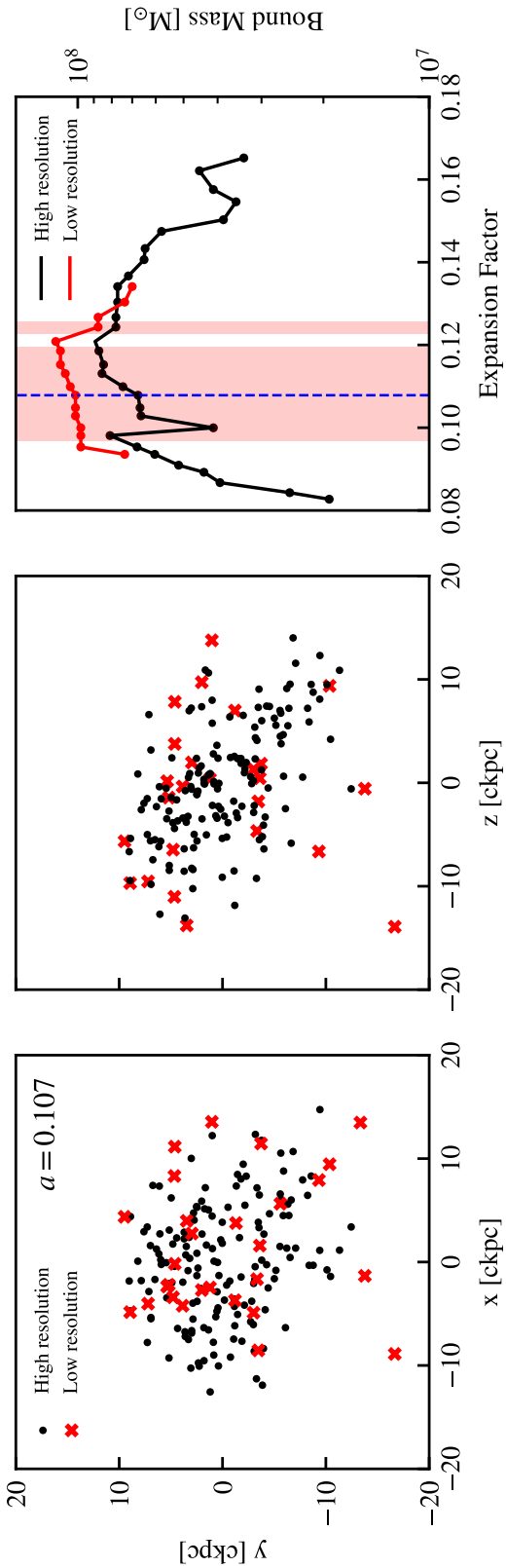

Figure 5.2: An example of a bound subgroup that is not part of any Friends of Friends group. *Left and middle panels*: distribution of the particles bound to the low (red crosses) and high resolution (black circles) version of the subgroup, projected along the z and x axis of the simulation box. *Right panel*: evolution of the bound mass of the subgroup in the low resolution simulation (red), and its higher resolution counterpart (black). The shaded area indicates the times during which the low resolution version of the subgroup is hostless, and the vertical blue line the time when the particle distribution is shown

as a candidate subgroup.

Indeed, the particles are still part of a self-bound subgroup for several outputs after becoming hostless. These times are indicated by the red shaded regions in Fig. 5.2, which amount to two distinct episodes, one lasting 9 output times and a final one that lasts 1 output time. To show that this is not a long-lived noise fluctuation in the density and velocity field, we match subgroups between Au6-L5 and Au6-L4 based on spatial proximity during an output when this subgroup is hostless.

We see that in the higher resolution simulation there is a subgroup that is co-spatial with the hostless subgroup we have examined. The higher resolution version is always found to be in a FOF group, since it is approximately sampled with eight times as many particles, and is therefore well above the particle number threshold. The increased resolution also leads to its earlier detection and longer survival time. Although the bound masses differ, this amounts to ~8 particles at the Au6-L5 resolution when it is hostless, and just ~2 particles when both are associated to a FOF group. These slight differences are explained by more structure forming in the high resolution version, meaning that some particles are instead assigned to different groups and subgroups.

The existence of hostless subgroups, as illustrated by the above example, suggests that substructure finders reliant an inital FOF group finding step are missing a population of low density subgroups (i.e. with lower concentrations) near the resolution limit of the simulation.

The above example also highlights the fact that merger tree codes that can account for the temporary disappearance of subgroups would have likely failed to link them. This is because these algorithms rely on specifying the number of snapshots to look ahead by, which is commonly chosen to be 5. This choice would have been insufficient to link the subgroups, given the long length of the first hostless episode. Given that how often substructure information is saved will also play a role in how long these hostless episodes last, there is clearly no best value to choose for this free parameter.

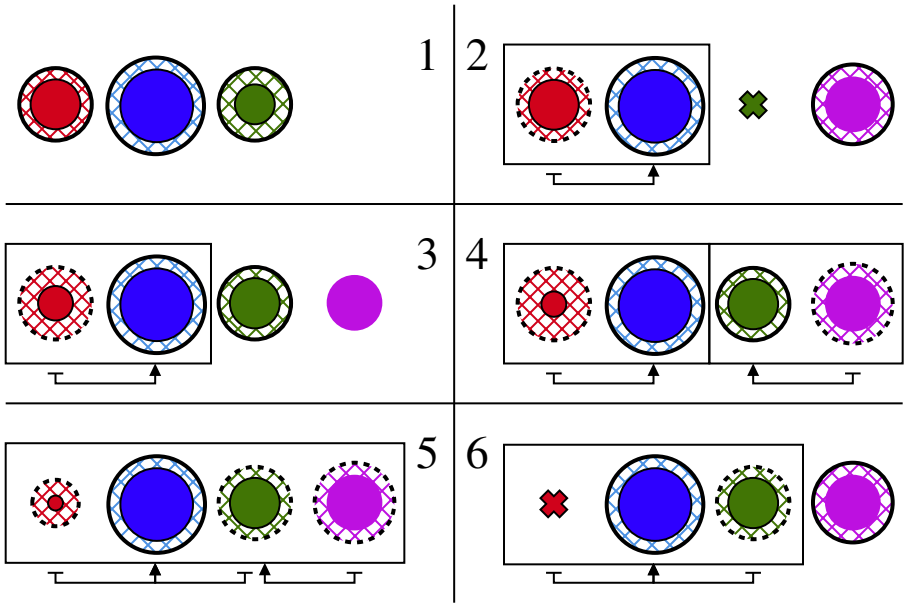

Figure 5.3: Diagram illustrating several scenarios that arise during the assembly of structure tracked with HBT, with time progressing as indicated by the panel numbers along the central spline. Solid circles represent the bound component of a subgroup, and the surrounding hatched circle represents its unbound source. If its exterior is outlined by a (dashed) solid line, it is the (substructure) central of its FOF group. If it is a hostless subgroup, no outline is present. Crosses indicate orphaned tracks and represent the most bound particle of the subgroup when it was last resolved. The colours indicate unique tracks, which are numbered according to the relative size of their FOF group at the time of creation: blue (0), red (1), green (2), and purple (3). FOF groups with one than more track are enclosed by black rectangles, and the hierarchy between tracks within is indicated by the inferior arrows.

5.3.1.7 A worked example

We now discuss how the principles of the HBT algorithm translate into the practical tracking of the evolution of substructure. For this purpose, we use as an example the simple setup shown in Fig. 5.3, which only considers a subset of all physical processes at play during the evolution of substructure. For example, the mass growth of subgroups is not shown here, but this is unimportant to represent the logic behind the algorithm, which is our main intent here. In increasing output times, or alternatively, ascending panel number:

1. Three new FOF groups form, none of which contain tracer particles associated to pre-existing tracks. As such, three new temporary tracks are spawned, whose source subgroup corresponds to the FOF particles they are hosted in. After subjecting them

to an unbinding algorithm, they are confirmed to be self-bound, and hence three new unique tracks are created, with their IDs based on the relative size of their FOF group: 0 (blue), 1 (red) and 2 (green).

2. We again find three FOF groups, two of which contain tracer particles associated to the tracks spawned in the first panel. The blue and red are in the same one, but were both previously centrals, meaning that one has to become secondary substructure. Based on its large mass relative to the red one, the blue track is assigned to be the central. The green is in a separate FOF group, but it has no bound component. Consequently, its source is trimmed to be 0, its disruption time is logged and the subsequent position & velocity of this track is represented by its most bound particle identified during the first output. The third FOF group has no associated tracer particles, creating a new temporary track, which is later confirmed to have a bound component. We now have a new (magenta) track, with TrackID 3.

3. The red track progressively loses mass, but its source subgroup remains the same since it is still small relative to its bound component. The tracer of the (orphaned) green track is found within a FOF group that contains no other tracers, allowing its source subhalo to grow. After unbinding, a bound component is once again found, and hence the track is no longer orphaned. The magenta tracer is not found within any FOF group, making it hostless. Nonetheless, the particles that belonged to its source in the previous panel can still be subject to unbinding, finding a bound subgroup.

4. The red track continues to be stripped of mass, but the source is still small compared to its bound component. The green and magenta tracers are found in the same FOF, and so a central needs to be decided. Given their similar bound masses in the previous output, a decision based on kinetic energy is triggered, which selects the green as the central.

5. There is only one FOF group, which contains all particle tracers. As the green and blue tracks were centrals in the previous panel, a central decision is made, making the blue one its central based on its mass. The red track has lost sufficient mass to

trigger the trimming of its source, with the particles removed from it now associated to its parent, the blue track.

6. The red track has been stripped of so much mass that it has disrupted, and is therefore subsequently tracked as an orphan track. The magenta tracer is found in a separate FOF group, meaning it has detached, and thus it has become a central again.

5.3.2 Concurrent Tracking of the Assembly of Particles into Substructure

The large amounts of data storage required for the highest resolution version of our simulations limits how many outputs we can store. Given our interest in studying the fine-grained time evolution of the subhalo population around the MW, we require about 1500 outputs to provide a time resolution of 10 Myr below $z = 2$. This would require $\sim$ 3000 TB of storage in uncompressed particle data for Au6-L0 alone, and so we opt for saving substructure information more often than particle data.

This can be achieved in two different ways. The simplest is to save particle information during every output time of interest, run the substructure finding algorithm in post-processing, and then delete the particle dumps that are no longer required. This approach results in unnecessary I/O time, to save unwanted particle information, load them to post-process and then remove them.

The alternative we choose is to run the substructure finding algorithm on the fly, so that no unnecessary particle information needs to be saved. The original public release of GADGET-4 comes with two substructure finding algorithms that work on-the-fly: SUBFIND and SUBFIND-HBT. Neither of these are suitable for the simulations and analysis we plan on doing. The former is prone to suffering from mass fluctuations and temporarily loss of substructure near pericentre, which is illustrated by the red lines in Fig. 5.4. The latter makes different algorithmic choices compared to HBT+, leading to changes in the measured evolution of subgroups. These will be discussed in the next subsection.

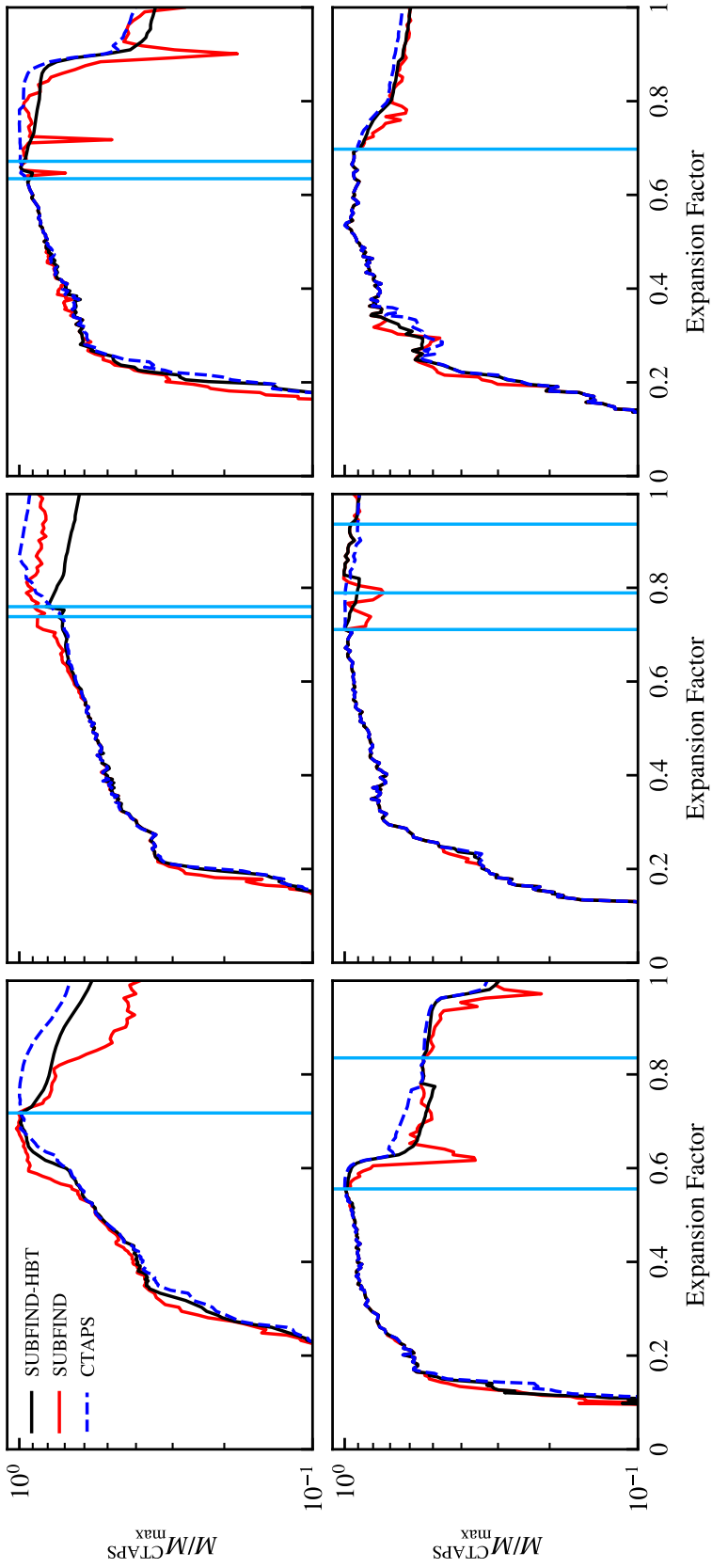

Figure 5.4: Comparison of the bound mass evolution of six Milky Way satellites, measured the three different substructure algorithms now implemented in GADGET-4 and able to run on the fly: SUBFIND (red), SUBFIND-HBT (black) and our new implementation, CTAPS (dashed blue). The times when the substructure is accreted by the MW halo are indicated by the vertical blue lines. The identification of substructure was done using the same particle information, and all methods use the same unbinding algorithm. The changes are thus caused by different definitions of the source subhalo.

As such, we have ported the working principles of HBT+ into GADGET-4, creating a new implementation able to run on the fly and provide robust substructure finding and tracking. This new implementation, which we refer to as CTAPS (**C**oncurrent **T**racking of the **A**ssembly of **P**articles into **S**ubstructures), leverages several of the tools and algorithms already present in GADGET-4 to enable efficient parallelisation.

The initial step of identifying FOF groups is done using the tree-based algorithm available in GADGET-4, which is able to handle large groups and scale well. Following this, pre-existing tracks get their host group updated based on the FOF membership of their tracer particle, and if one or more accretions have occurred within a group, central decisions take place. Our implementation is able to handle decisions based on kinetic energies in parallel, which speeds up calculations for large groups whose particles are split across several tasks. Any remaining FOF groups without centrals get assigned a newly created, temporary track. Finally, the source subgroup of centrals is updated.

The subsequent unbinding of individual groups and its substructure requires balancing how many get analysed in parallel, and if so, how many tasks they get assigned. For this purpose, we use the scheduling algorithm used in SUBFIND. Particles that share the same central track are grouped, and the total number of associated particles is tallied. Note that these particle groupings do not correspond to FOF groups, since they include the source of secondary subgroups, which are not necessarily confined to a FOF group (see Fig. 5.5), and also account for hostless subgroups.

Any grouping whose particle count exceeds a threshold, proportional to the mean particle number per task, is analysed in parallel using more than one task. The remaining groupings are analysed in serial using the tasks not dedicated to parallel analysis, which get assigned in a round-robin fashion. Each task will then analyse each grouping it was assigned to from the largest to the smallest in mass, leaving hostless tracks until last.

The analysis of individual particle groupings begins by creating a list of subgroup candidates, based on the tracks that share the same central. An illustration of how this is handled within the code is show in Fig 5.5. The hierarchical connections determine which sub-

groups need to be analysed first, which as mentioned before, should be done in a depth-first approach: satellites need to be analysed before the central, the satellites-of-satellites before the satellites, etc.

We do this using an iterative approach, which identifies in each iteration which candidates have not been analysed yet and which have no dependent subgroups waiting to be analysed. This list of independent subgroups is then analysed sequentially, if only one task is available, or each candidate gets distributed in a round-robin fashion if more are available. This continues until no more candidates are left to be analysed.

After all tracks have been analysed, the resulting information is stored as subgroup catalogues, which include all tracks which have ever been identified in the simulation, regardless of whether they are now orphans or have merged previously. These are sorted in ascending TrackID number, to enable fast access to the evolutionary histories of subgroups, based on the direct correspondence between the TrackID of a given object and its index location within the subgroup information array. If particle information is saved, they also get sorted according to which track they are bound to. The required particle array offsets and lengths used to quickly select a sub-array of particles bound to a given TrackID are available in the subgroup catalogues.

In Fig. 5.4 we show the measured evolution of six satellites found around the Milky Way halo at $z = 0$, and how their mass evolution compare between SUBFIND, SUBFIND-HBT and CTAPS. As mentioned previously, SUBFIND suffers from mass fluctuations, particularly during pericentric passages. CTAPS leads to smoother mass evolutions, and although not shown in for these examples, the implementation is able to handle all the features discussed within the HBT algorithm, including hostless subgroups. Throughout the implementation process, we have verified that our results agree with those found using the standalone version of HBT+.

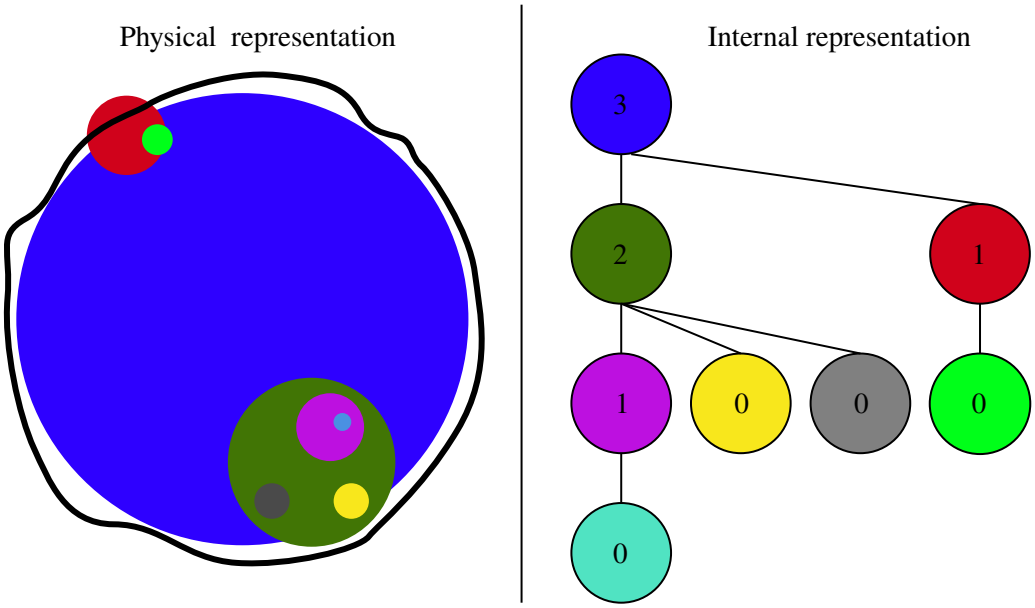

Figure 5.5: Diagram illustrating the spatial distribution of all substructures associated to a unique central subgroup, and how the hierarchical information between them is encoded within CTAPS. *Left side*: spatial distribution of substructures, represented by coloured circles, whose centres are contained within their subgroup parents. The boundary of the FOF group is represented by the solid black contour, and its central subgroup is the blue. Note that particles not formally classified as part of the FOF group are still included in this particle grouping, e.g. those belonging to the red subgroup. *Right side*: encoding of the hierarchical relations between the subgroups shown in the left side, represented as nodes whose parent-child relations are shown by the black lines. The number within each node indicates the iteration when the subgroup was subject to unbinding, which can only occur when all children have been analysed first.

5.3.3 Comparison to SUBFIND-HBT

One of the new features of GADGET-4 is a substructure finder inspired by the particle tracking method of HBT: SUBFIND-HBT. Despite their similar names, it is based on different algorithmic choices that lead to changes in the measured evolution of subhaloes.

For example, there is no persistent track information in the simulation, meaning that it relies on an additional step to build merger trees and link consecutive data outputs. This is based on using the 20 most bound particles of subgroups to identify the most likely descendant and progenitor, based on scoring candidates using a sum weighted by the boundness ranking of the tracer particles.

The lack of information about the past merger history of subhaloes also entails that no hierarchical information between substructure exists. This speeds up the process of unbinding, as substructure does not need to be analysed in a depth-first approach, enabling more efficient parallelisation for the unbinding of the now-independent subhaloes. However, this is potentially detrimental to studies concerning the satellites of satellites and group infall, such as the case for the LMC, SMC and additional satellites it brought with it.

Similarly to SUBFIND, it only considers particles that are linked in FOF groups during substructure identification. As such, background subgroups like those discussed in §5.3.1.6 are not identified. Together with the fact that the merger tree algorithm it uses does not allow for the possibility of temporarily missing subgroups, even if they are associated to FOF groups, this will lead to many more disjoint merger tree branches and hence orphans.

Lastly, it over-trims the source subgroup of secondary subgroups, leading to the continuous 'evaporation' of their outer boundary. This occurs because it assigns the source subgroup of candidates to be particles that were bound to its progenitor during the previous output, i.e. $f_{\rm source} = 1$. In principle, this choice still enables the possibility of secondary subhaloes retaining their mass, but in practice always results in mass losses.

This is the cause behind the differences between CTAPS and SUBFIND-HBT shown in Fig. 5.4. The time at which subgroups become secondary are indicated by the vertical lines in each panel, which marks the onset of continuous mass loss, occurring even at large distances from the centre of the halo.

The effect of this spurious mass loss is clear for the example shown in bottom left panel. Shortly before $a \sim 0.8$, the subgroup becomes detached from the FOF group of the MW-mass halo (i.e. this is a backsplash halo) and SUBFIND-HBT reactivates the accretion of mass. At this stage, it finds the outer boundary that was previously lost, instantaneously correcting the value to one consistent with that found in CTAPS and SUBFIND.

In essence, repeatedly sampling the binding energy of particles will lead to a few being classified as unbound, although they may later be found as bound. Defining the source by 'instantaneous' boundness permanently removes unbound particles that would contribute

bound mass at later times. Since this is likely to occur for those near $E_{\rm binding} = 0$, it primarily affects the outer halo boundary.

5.4 Summary and future work

In summary, ultra-faints represent a powerful tool to constrain the nature of the dark matter, given that they are sensitive to a cut-off in the power spectrum and structural changes caused by self-interactions. This affects their numbers and distribution around the Milky Way, and hence their predicted detectability. Nonetheless, numerical limitations prevalent in these poorly resolved objects bias predictions concerning their evolution, and hence compromise their usefulness to constrain the nature of dark matter .

To address these concerns, we are proposing an ambitious project aimed to simulate Milky Way-mass haloes at the highest resolution to date. Compared to its spiritual predecessor, Aq-A, it will have updated cosmological parameters, simulate a halo that is more representative of our own, and have $\sim$ 18 times better mass resolution. To enable constraints based on different DM models, the halo will be run using a CDM and 7 keV sterile neutrino model.

As a first step, we have outlined the technical and output frequency requirements for these simulations to enable a comprehensive analysis of the evolution of galactic subhaloes. Based on the limitations of most substructure algorithms, we have decided to use HBT+, which finds substructure using particle tracking, a more robust method that limits the amount of spurious disruption present in other codes. This is crucial not only for unbiased predictions concerning the smallest substructures, but also to asses the convergence of their properties across different resolution simulations, and to test whether commonly used orphan models can provide realistic predictions at lower resolutions.

However, the requirements needed to analyse the time-evolution of substructure at a sufficiently high cadence to resolve pericentric passages means that saving particle data is prohibitively expensive storage-wise. This means that only a subset of the outputs can be saved with particle information, whereas the majority only contain subgroup information.

To enable doing this without excessive I/O time, we have implemented the working principles of HBT+ in the state-of-the-art cosmological code GADGET-4. This new on the fly substructure implementation, CTAPS (**C**oncurrent **T**racking of the **A**ssembly of **P**articles into **S**ubstructures), has been tested against the predictions of HBT+ to verify its correct implementation, and will be eventually be publicly released.

Shortly before the submission of this thesis, we have sent a computing time proposal requesting 20 million CPU-hours to carry out the simulations we have discussed in this chapter. This will be sufficient to run a CDM and 7 keV sterile neutrino versions of Auriga halo 6 at a particle mass resolution of $m_{\rm DM} \sim 750\,{\rm M}_\odot$. Although this is not our final sub-$100\,{\rm M}_\odot$ target, it will constitute an essential stepping stone towards assessing the scalability and accuracy of the methods and codes discussed above. Nonetheless, these record-breaking simulations (a factor of 2.5 and 22.5 times higher mass resolution in CDM) will also be extremely useful to begin making predictions concerning galactic subhaloes and testing orphan modelling schemes.

Sixth Chapter

Conclusions

This thesis has explored how differences in the nature of dark matter affects small-scale predictions concerning MW-mass haloes and their surrounding galactic environment. We have done so whilst keeping in mind the important effects of galaxy formation, which play an important role on these scales. Our main findings are summarised below.

6.1 The central DM density of MW-mass haloes is modified by internal galactic processes

In Chapter 2 we investigated the internal distribution of dark matter within haloes with masses similar to the Milky Way. We found that their central dark matter density is enhanced in hydrodynamical simulations that model galaxy formation realistically, compared to their dark matter-only counterparts. The resulting steepening of the density profile is caused by the contraction of the halo, which is induced by the gravitational attraction of a sufficiently massive galaxy at its centre.

Given that the effect of contraction has been inferred from real observations of elliptical galaxies and our Galaxy (e.g. Oldham & Auger, 2018; Cautun et al., 2020), understanding its effects plays an essential role in the dynamical modelling of massive galaxies. This also concerns predictions on the direct DM detection prospects, since they rely on an estimate for the DM density background near the Solar neighbourhood.

Models to account for the effect of halo contraction have been developed under a variety of assumptions. The simplest rely on adiabatic modelling, whilst more realistic ones derive empirical fits based on the properties of $z = 0$ galaxies formed in hydrodynamical

simulations. However, we find that this process is non-adiabatic, and that there is a substantial time evolution in how contracted a given halo is.

The changing degree of contraction is driven by processes internal to the central galaxy. We found that gas blowouts driven by Active Galacti Nuclei (AGN), as well as stellar bars, are the main processes behind the observed evolution. Since the number of AGN episodes and the properties of the stellar bar (strength and age) vary from galaxy to galaxy, both effects make assembly histories of galaxies an important element to include in contraction models.

6.2 Baryonic effects mimic alternative dark matter models in the classical dwarf galaxy regime

We examined how different dark matter models affect the predicted properties of the satellite systems of the Milky Way-mass haloes in Chapter 3. To do so, we used a suite of hydrodynamical simulations based on the EAGLE galaxy formation model which included different dark matter models: cold, warm and self-interacting with varying cross-sections.

The properties of isolated haloes were found to be dependent on the dark matter halo. The overall number of haloes and the fraction that host galaxies, is heavily suppressed in WDM. Their density profiles are also different, reflecting the lower concentrations resulting from a delayed growth. For the model of SIDM that we considered, which has the same power spectrum as CDM, the only changes occur in their internal structure. The self-interactions lead to the formation of flat-density cores, with their size increasing monotonically with the value of cross-section.

These differences propagate to the properties of satellites when they are first accreted by their hosts, which also determines their subsequent tidal evolution based on their structural parameters. As such, despite starting with the same number of satellite galaxies in CDM and SIDM, the enhanced tidal stripping in the latter results in less surviving satellites than the former at $z = 0$. In WDM, the suppression of the satellite population is largely driven

by less galaxies forming, rather than enhanced stripping caused by lower concentrations.

In this work we also considered variations in the galaxy formation physics. In our fiducial model, based on the EAGLE galaxy formation physics, gas blowouts in dwarfs cannot create flat-density cores. To allow for this possibility, we increased the density threshold for star formation, a free parameter of the subgrid physics that regulates the efficiency (and existence) of baryon-driven flat-density core.

After doing so, the density profiles in CDM and WDM closely resemble those found in SIDM models. This subsequently results in their enhanced tidal stripping, and so by $z = 0$, it becomes difficult to differentiate between CDM models with cores, and certain models of SIDM.

The current uncertainties regarding galaxy formation at the dwarf galaxy regime hinders their use as powerful power constraints on the nature of dark matter. As shown in our work, their predicted properties are strongly dependent on the assumed galaxy formation physics, which are themselves degenerate with the changes found in alternatives to CDM.

Given this, furthering our understanding of the nature of dark matter based on small scale constraints can only progress along two different avenues. The first is, of course, to better constrain the effects of feedback in real dwarf galaxies. Impulsive gas blowouts may leave a dynamical imprint on stars, whereas self-interactions do not (Burger et al., 2022). This can help disentangle the precise origins behind inferred cores. Another alternative is to focus instead on ultra-faint galaxies, which have such low baryonic mass that the processes discussed in this work are unable to significantly alter the DM density distribution. As such, their internal structure will be more directly connected to the nature of dark matter itself. This motivates the work done in Chapter 5 of this thesis.

6.3 The stellar haloes of MW-mass galaxies bear the imprints of the nature of dark matter

Chapter 4 was dedicated to an ongoing study of how the properties of the stellar halo around MW-mass haloes relate to the underlying dark matter model. This is a natural extension of Chapter 3, given our findings concerning the differences caused by alternative dark matter models in modifying the number of galaxies accreted by the MW-mass haloes, as well as their subsequent tidal evolution. Since the stellar haloes are made up by their stripped remnants, it is interesting to consider whether these changes result in observable differences at the present day.

We found no differences on the total mass of accreted stars, which is unsurprising based on the fact that the total mass budget is largely composed of a few massive objects. For the models we have considered, there are no significant changes in their total and stellar mass, and hence they contribute the same amount of stellar mass to the stellar halo after sinking through dynamical friction.

Nonetheless, differences in how the stellar halo is spatially distributed exist. We found evidence for a significantly shallower inner density profile in SIDM, whilst the those formed in a WDM cosmology are slightly steeper. This results in ex-situ mass fractions that are noticeably different than CDM within 10 kpc: up to a 55% (73%) enhancement (suppression) in WDM (SIDM).

The properties of the substructure present in phase-space also differ across dark matter models. In haloes where chevrons are present, the SIDM counterparts have larger amounts of them and are thinner than in CDM and WDM. However, the differences become less pronounced once the stellar halo becomes less massive. As this correlates with the assembly history of its host galaxy, it will be interesting to explore what the implications are for the stellar halo of the Milky Way.

To understand the origin behind these differences, we identified the progenitor galaxies of the stellar haloes, finding that their characteristic mass distribution is similar across

dark matter models. This suggests the differences found above are due to orbital changes. Indeed, we find that progenitors of the stellar haloes in SIDM always disrupted at larger distances, whereas the most massive ones in WDM seem to disrupt at slightly smaller distances that those found CDM.

To summarise, we have only considered a subset of stellar halo properties that could be modified as a consequence of changing dark matter models. For example, the relative importance between tidal stripping and dynamical friction will also influence the circularity parameter of stars, and hence the anisotropy profiles. These properties are, in principle, observable. Our initial findings are promising, and thus motivate further exploration in preparation for upcoming data concerning the stellar halo of the Milky Way (e.g. DESI MW, Vera Rubin LSST, etc).

6.4 Towards unbiased predictions of the ultra-faint satellite population around the Milky Way

The final chapter of this thesis discussed ongoing preparations towards running the highest resolution dark matter-only simulations of Milky Way-mass haloes in CDM and WDM to date. These will reach a final mass resolution of $\sim 95\,\mathrm{M}_\odot$, about 20 times higher than the previous record holder. This unprecedented resolution level will provide unbiased predictions concerning the full satellite population in different DM models without resorting to 'orphan modelling'.

As part of our initial preparation, we have considered the problem of substructure finding, and how different algorithms perform between each other. Based on the performance of particle tracking methods, we have chosen to use an algorithm based on Hierarchical Bound Tracing.

To reduce the storage footprint and I/O time of the simulation, we have ported the working principles of HBT+ into the state-of-the-art cosmological code GADGET-4. This new substructure finding implementation, which is able to run on the fly, will eventually be

made public. Just before completing this thesis, we submitted a computing time proposal requesting 20 million CPU-hours, which is sufficient to complete all resolution levels in CDM and WDM up to the second highest resolution we consider in this project ($m_{\rm DM} \sim 750\,{\rm M}_{\odot}$).

6.5 Final remarks

The cold dark matter model has proven to be an invaluable tool in our understanding of cosmic structure formation. Nonetheless, the original particle physics models that motivated it remain undetected. As such, our priors should be relaxed, an well-motivated alternatives should also be considered.

The increasing depth of surveys targeting the environment of Local Group has resulted in an ever growing census of small-scale structure. These objects lie in the mass range best suited to further constrain the nature of dark matter, since differences between alternative models occur on these scales.

There is, however, an increasing mismatch between small-scale observations and predictions based from simulations, as evidenced by the numerical limitations that plague most cosmological simulations. Until these are not addressed, corrected and understood, we will not be able to fully leverage the wealth of data that is coming and is to come.

Addressing this gap will require increasingly expensive computational calculations, which in the author's opinion, is an extremely worthwhile investment towards unravelling the nature of one of the most important unanswered questions of modern science.

Bibliography

Abadi M. G., Navarro J. F., Fardal M., Babul A., Steinmetz M., 2010, MNRAS, 407, 435

Abbott B. P., et al., 2016, Phys. Rev. Lett., 116, 061102

Abbott T. M. C., et al., 2022, Phys. Rev. D, 105, 023520

Adriani O., et al., 2009, Nature, 458, 607

Agertz O., et al., 2020, MNRAS, 491, 1656

Agnello A., Evans N. W., 2012, ApJ, 754, L39

Alam S., et al., 2015, ApJS, 219, 12

Alam S., et al., 2021, Phys. Rev. D, 103, 083533

Algorry D. G., et al., 2017, MNRAS, 469, 1054

Alpher R. A., Bethe H., Gamow G., 1948, Physical Review, 73, 803

Amorisco N. C., 2017, MNRAS, 464, 2882

Amorisco N. C., Evans N. W., 2012, MNRAS, 419, 184

Aprile E., et al., 2018, Phys. Rev. Lett., 121, 111302

Arkani-Hamed N., Finkbeiner D. P., Slatyer T. R., Weiner N., 2009, Phys. Rev. D, 79, 015014

Arnold C., Leo M., Li B., 2019, Nature Astronomy, 3, 945

Artale M. C., Pedrosa S. E., Tissera P. B., Cataldi P., Di Cintio A., 2019, A&A, 622, A197

Asplund M., Lambert D. L., Nissen P. E., Primas F., Smith V. V., 2006, ApJ, 644, 229

Athanassoula L., 2003, Angular Momentum Redistribution and the Evolution and Morphology of Bars. Springer, Berlin, Heidelberg, pp 313–326, doi:10.1007/978-3-540-45040-

5_26

Athanassoula E., 2013, Bars and secular evolution in disk galaxies: Theoretical input. Cambridge University Press, p. 305–352, doi:10.1017/CBO9781139547420.006

Bahl H., Baumgardt H., 2014, MNRAS, 438, 2916

Balberg S., Shapiro S. L., Inagaki S., 2002, ApJ, 568, 475

Barnes J., White S. D. M., 1984, MNRAS, 211, 753

Bechtol K., et al., 2015, ApJ, 807, 50

Behroozi P. S., Wechsler R. H., Wu H.-Y., 2013a, ApJ, 762, 109

Behroozi P. S., Wechsler R. H., Wu H.-Y., Busha M. T., Klypin A. A., Primack J. R., 2013b, ApJ, 763, 18

Belokurov V., Kravtsov A., 2022, MNRAS, 514, 689

Belokurov V., Erkal D., Evans N. W., Koposov S. E., Deason A. J., 2018, MNRAS, 478, 611

Belokurov V., Vasiliev E., Deason A. J., Koposov S. E., Fattahi A., Dillamore A. M., Davies E. Y., Grand R. J. J., 2023, MNRAS, 518, 6200

Benitez-Llambay A., Frenk C., 2020, MNRAS, 498, 4887

Benítez-Llambay A., Navarro J. F., Abadi M. G., Gottlöber S., Yepes G., Hoffman Y., Steinmetz M., 2016, MNRAS, 456, 1185

Benítez-Llambay A., et al., 2017a, MNRAS, 465, 3913

Benítez-Llambay A., et al., 2017b, MNRAS, 465, 3913

Benítez-Llambay A., Frenk C. S., Ludlow A. D., Navarro J. F., 2019, MNRAS, 488, 2387

Berentzen I., Athanassoula E., Heller C. H., Fricke K. J., 2004, Monthly Notices of the Royal Astronomical Society, 347, 220

Berrier J. C., Sellwood J. A., 2015, ApJ, 799, 213

Bhargava S., et al., 2020, MNRAS, 497, 656

Binney J., Gerhard O. E., Stark A. A., Bally J., Uchida K. I., 1991, MNRAS, 252, 210

Blennow M., Fernandez-Martinez E., Mena O., Redondo J., Serra P., 2012, JCAP, 07, 022

Blumenthal K. A., Barnes J. E., 2018, MNRAS, 479, 3952

Blumenthal G. R., Faber S. M., Flores R., Primack J. R., 1986, ApJ, 301, 27

Boddy K. K., Kaplinghat M., Kwa A., Peter A. H. G., 2016, Phys. Rev. D, 94, 123017

Bode P., Ostriker J. P., Turok N., 2001, ApJ, 556, 93

Booth C. M., Schaye J., 2009, MNRAS, 398, 53

Borukhovetskaya A., Navarro J. F., Errani R., Fattahi A., 2022, MNRAS, 512, 5247

Bose S., et al., 2017, MNRAS, 464, 4520

Bose S., et al., 2019, MNRAS, 486, 4790

Bose S., Deason A. J., Belokurov V., Frenk C. S., 2020, MNRAS, 495, 743

Bouché N. F., et al., 2022, A&A, 658, A76

Bovy J., 2015, ApJS, 216, 29

Bovy J., Bahmanyar A., Fritz T. K., Kallivayalil N., 2016, ApJ, 833, 31

Boyarsky A., Ruchayskiy O., Iakubovskyi D., Franse J., 2014, Phys. Rev. Lett., 113, 251301

Boyarsky A., Franse J., Iakubovskyi D., Ruchayskiy O., 2015, Phys. Rev. Lett., 115, 161301

Boyarsky A., Malyshev D., Ruchayskiy O., Savchenko D., 2020, arXiv e-prints, p. arXiv:2004.06601

Boylan-Kolchin M., Bullock J. S., Kaplinghat M., 2011, MNRAS, 415, L40

Bozorgnia N., Bertone G., 2017, International Journal of Modern Physics A, 32, 1730016

Bozorgnia N., et al., 2016, J. Cosmology Astropart. Phys., 2016, 024

Breddels M. A., Helmi A., van den Bosch R. C. E., van de Ven G., Battaglia G., 2013, MNRAS, 433, 3173

Brook C. B., Di Cintio A., Knebe A., Gottlöber S., Hoffman Y., Yepes G., Garrison-Kimmel S., 2014, ApJ, 784, L14

Bryan G. L., Norman M. L., 1998, ApJ, 495, 80

Buck T., Obreja A., Macciò A. V., Minchev I., Dutton A. A., Ostriker J. P., 2020, MNRAS, 491, 3461

Buckley M. R., Fox P. J., 2010a, Phys. Rev. D, 81, 083522

Buckley M. R., Fox P. J., 2010b, Phys. Rev. D, 81, 083522

Bulbul E., Markevitch M., Foster A., Smith R. K., Loewenstein M., Randall S. W., 2014, ApJ, 789, 13

Bullock J. S., Johnston K. V., 2005, ApJ, 635, 931

Bullock J. S., Kravtsov A. V., Weinberg D. H., 2000, ApJ, 539, 517

Burger J. D., Zavala J., Sales L. V., Vogelsberger M., Marinacci F., Torrey P., 2022, MNRAS,

Burkert A., 1995, ApJ, 447, L25

Buschmann M., Kopp J., Safdi B. R., Wu C.-L., 2018, Phys. Rev. Lett., 120, 211101

Buta R. J., et al., 2015, ApJS, 217, 32

Caldwell N., et al., 2017, ApJ, 839, 20

Callingham T. M., et al., 2019, MNRAS, 484, 5453

Callingham T. M., Cautun M., Deason A. J., Frenk C. S., Grand R. J. J., Marinacci F., Pakmor R., 2020, MNRAS, 495, 12

Calore F., et al., 2015, J. Cosmology Astropart. Phys., 2015, 053

Canepa A., 2019, Reviews in Physics, 4, 100033

Carlsten S. G., Greene J. E., Peter A. H. G., Greco J. P., Beaton R. L., 2020, ApJ, 902, 124

Cautun M., Bose S., Frenk C. S., Guo Q., Han J., Hellwing W. A., Sawala T., Wang W., 2015, MNRAS, 452, 3838

Cautun M., et al., 2020, MNRAS, 494, 4291

Cerny W., et al., 2021a, ApJ, 910, 18

Cerny W., et al., 2021b, ApJ, 920, L44

Cerny W., et al., 2023, ApJ, 942, 111

Ceverino D., Klypin A., 2007, MNRAS, 379, 1155

Chan T. K., Kereš D., Oñorbe J., Hopkins P. F., Muratov A. L., Faucher-Giguère C.-A.,

Quataert E., 2015, Monthly Notices of the Royal Astronomical Society, 454, 2981

Chandrasekhar S., 1943, ApJ, 97, 255

Chiba M., Beers T. C., 2000, AJ, 119, 2843

Chiti A., et al., 2021, Nature Astronomy, 5, 392

Cirelli M., Gouttenoire Y., Petraki K., Sala F., 2019, JCAP, 02, 014

Clowe D., Bradač M., Gonzalez A. H., Markevitch M., Randall S. W., Jones C., Zaritsky D., 2006, ApJ, 648, L109

Cohl H. S., Tohline J. E., 1999, ApJ, 527, 86

Cole S., et al., 2005, MNRAS, 362, 505

Combes F., Gerin M., 1985, A&A, 150, 327

Conn A. R., et al., 2013, ApJ, 766, 120

Conroy C., et al., 2019, ApJ, 883, 107

Cooper A. P., Parry O. H., Lowing B., Cole S., Frenk C., 2015, MNRAS, 454, 3185

Cooper A. P., et al., 2023, ApJ, 947, 37

Correa C. A., 2021, MNRAS, 503, 920

Cowsik R., McClelland J., 1973, ApJ, 180, 7

Crain R. A., et al., 2015, MNRAS, 450, 1937

D'Onghia E., Springel V., Hernquist L., Keres D., 2010, ApJ, 709, 1138

Dalla Vecchia C., Schaye J., 2012, MNRAS, 426, 140

Das P., Hawkins K., Jofré P., 2020, MNRAS, 493, 5195

Davies J. J., Crain R. A., Oppenheimer B. D., Schaye J., 2020, MNRAS, 491, 4462

Davis M., Efstathiou G., Frenk C. S., White S. D. M., 1985, ApJ, 292, 371

Dawson W. A., et al., 2012, ApJ, 747, L42

Dayal P., Choudhury T. R., Bromm V., Pacucci F., 2017, ApJ, 836, 16

De Lucia G., Blaizot J., 2007, MNRAS, 375, 2

Deason A. J., Belokurov V., Evans N. W., 2011, MNRAS, 416, 2903

Deason A. J., Belokurov V., Koposov S. E., Lancaster L., 2018, ApJ, 862, L1

Deason A. J., Belokurov V., Sanders J. L., 2019, MNRAS, 490, 3426

Deason A. J., et al., 2021, MNRAS, 501, 5964

Deason A. J., Bose S., Fattahi A., Amorisco N. C., Hellwing W., Frenk C. S., 2022, MNRAS, 511, 4044

Debattista V. P., Mayer L., Carollo C. M., Moore B., Wadsley J., Quinn T., 2006, ApJ, 645, 209

Debattista V. P., Moore B., Quinn T., Kazantzidis S., Maas R., Mayer L., Read J., Stadel J., 2008, ApJ, 681, 1076

Delos M. S., 2023, MNRAS, 522, L78

Delos M. S., White S. D. M., 2022, arXiv e-prints, p. arXiv:2209.11237

Dessert C., Foster J. W., Park Y., Safdi B. R., 2023, arXiv e-prints, p. arXiv:2309.03254

Di Cintio A., Brook C. B., Macciò A. V., Stinson G. S., Knebe A., Dutton A. A., Wadsley J., 2014a, MNRAS, 437, 415

Di Cintio A., Brook C. B., Dutton A. A., Macciò A. V., Stinson G. S., Knebe A., 2014b, MNRAS, 441, 2986

Dicke R. H., Peebles P. J. E., Roll P. G., Wilkinson D. T., 1965, ApJ, 142, 414

Diemand J., Kuhlen M., Madau P., 2006, ApJ, 649, 1

Diemer B., Behroozi P., Mansfield P., 2023, arXiv e-prints, p. arXiv:2305.00993

Dodelson S., 2011, International Journal of Modern Physics D, 20, 2749

Dodelson S., Widrow L. M., 1994, Phys. Rev. Lett., 72, 17

Downing E. R., Oman K. A., 2023, MNRAS, 522, 3318

Drlica-Wagner A., et al., 2015, ApJ, 813, 109

Drlica-Wagner A., et al., 2020, ApJ, 893, 47

Drlica-Wagner A., et al., 2021, ApJS, 256, 2

Dubinski J., 1994, ApJ, 431, 617

Dubinski J., Carlberg R. G., 1991, ApJ, 378, 496

Dubinski J., Berentzen I., Shlosman I., 2009, The Astrophysical Journal, 697, 293–310

Dutton A. A., et al., 2016, MNRAS, 461, 2658

Dwek E., et al., 1995, ApJ, 445, 716

Dyson F. W., Eddington A. S., Davidson C., 1920, Philosophical Transactions of the Royal Society of London Series A, 220, 291

Eddington A. S., 1930, MNRAS, 90, 668

Efstathiou G., Lake G., Negroponte J., 1982, MNRAS, 199, 1069

Efstathiou G., Frenk C. S., White S. D. M., Davis M., 1988, MNRAS, 235, 715

Efstathiou G., Sutherland W. J., Maddox S. J., 1990, Nature, 348, 705

Einasto J., 1965, Trudy Astrofizicheskogo Instituta Alma-Ata, 5, 87

Einasto J., Kaasik A., Saar E., 1974, Nature, 250, 309

Einstein A., 1917, Sitzungsber. Preuss. Akad. Wiss. Berlin (Math. Phys.), 1917, 142

Einstein A., de Sitter W., 1932, Proceedings of the National Academy of Science, 18, 213

Eisenstein D. J., et al., 2005, ApJ, 633, 560

Eke V. R., Cole S., Frenk C. S., 1996, MNRAS, 282, 263

El-Zant A., Shlosman I., Hoffman Y., 2001, ApJ, 560, 636

El-Zant A. A., Hoffman Y., Primack J., Combes F., Shlosman I., 2004, ApJ, 607, L75

El-Zant A. A., Freundlich J., Combes F., 2016, MNRAS, 461, 1745

Elbers W., Frenk C. S., Jenkins A., Li B., Pascoli S., 2021, MNRAS, 507, 2614

Elbert O. D., Bullock J. S., Garrison-Kimmel S., Rocha M., Oñorbe J., Peter A. H. G., 2015, Mon. Not. Roy. Astron. Soc., 453, 29

Ellis J., Hagelin J. S., Nanopoulos D. V., Olive K., Srednicki M., 1984, Nuclear Physics B, 238, 453

Emami N., Siana B., Weisz D. R., Johnson B. D., Ma X., El-Badry K., 2019, ApJ, 881, 71

Erkal D., Belokurov V., 2015, MNRAS, 454, 3542

Erkal D., Belokurov V., Bovy J., Sanders J. L., 2016, MNRAS, 463, 102

Erkal D., et al., 2021, MNRAS, 506, 2677

Errani R., Navarro J. F., 2021, MNRAS, 505, 18

Errani R., Navarro J. F., Peñarrubia J., Famaey B., Ibata R., 2022, Monthly Notices of the Royal Astronomical Society, 519, 384

Eskridge P. B., et al., 2000, AJ, 119, 536

Evans T. A., Fattahi A., Deason A. J., Frenk C. S., 2020, MNRAS, 497, 4311

Everitt C. W. F., et al., 2011, Phys. Rev. Lett., 106, 221101

Faber S. M., Lin D. N. C., 1983, ApJ, 266, L17

Fan J., Katz A., Shelton J., 2014, JCAP, 06, 059

Fanali R., Dotti M., Fiacconi D., Haardt F., 2015, MNRAS, 454, 3641

Fattahi A., et al., 2016, MNRAS, 457, 844

Fattahi A., Navarro J. F., Frenk C. S., Oman K. A., Sawala T., Schaller M., 2018, MNRAS, 476, 3816

Fattahi A., et al., 2020, MNRAS, 497, 4459

Feuillet D. K., Feltzing S., Sahlholdt C. L., Casagrande L., 2020, MNRAS, 497, 109

Fitts A., et al., 2017, MNRAS, 471, 3547

Flores R. A., Primack J. R., 1994, ApJ, 427, L1

Font A. S., McCarthy I. G., Crain R. A., Theuns T., Schaye J., Wiersma R. P. C., Dalla Vecchia C., 2011, MNRAS, 416, 2802

Fragkoudi F., Grand R. J. J., Pakmor R., Springel V., White S. D. M., Marinacci F., Gomez F. A., Navarro J. F., 2020, arXiv e-prints, p. arXiv:2011.13942

Friedmann A., 1922, Zeitschrift fur Physik, 10, 377

Fu S. W., Simon J. D., Alarcón Jara A. G., 2019, ApJ, 883, 11

Fukuda Y., et al., 1998, Phys. Rev. Lett., 81, 1562

Fulbright J. P., 2002, AJ, 123, 404

GRAVITY Collaboration et al., 2020, A&A, 636, L5

Gaia Collaboration et al., 2016a, A&A, 595, A1

Gaia Collaboration et al., 2016b, A&A, 595, A2

Gaia Collaboration et al., 2018, A&A, 616, A1

Gaia Collaboration et al., 2023, A&A, 674, A1

Gamow G., 1946, Physical Review, 70, 572

Garrison-Kimmel S., Boylan-Kolchin M., Bullock J. S., Lee K., 2014, MNRAS, 438, 2578

Garrison-Kimmel S., et al., 2017, MNRAS, 471, 1709

Gaskins J. M., 2016, Contemporary Physics, 57, 496

Genel S., et al., 2014, MNRAS, 445, 175

Genina A., Frenk C. S., Benítez-Llambay A., Cole S., Navarro J. F., Oman K. A., Fattahi A., 2019, MNRAS, 488, 2312

Genina A., Deason A. J., Frenk C. S., 2023, MNRAS, 520, 3767

Gentile G., Famaey B., de Blok W. J. G., 2011, A&A, 527, A76

Ghosh S., Saha K., Di Matteo P., Combes F., 2021, MNRAS, 502, 3085

Glazebrook K., Blake C., Economou F., Lilly S., Colless M., 1999, MNRAS, 306, 843

Gnedin O. Y., Ostriker J. P., 2001, ApJ, 561, 61

Gnedin O. Y., Kravtsov A. V., Klypin A. A., Nagai D., 2004, ApJ, 616, 16

Goerdt T., Moore B., Read J. I., Stadel J., Zemp M., 2006, MNRAS, 368, 1073

Governato F., et al., 2010, Nature, 463, 203

Grand R. J. J., et al., 2017, MNRAS, 467, 179

Grand R. J. J., et al., 2021, MNRAS, 507, 4953

Graus A. S., Bullock J. S., Kelley T., Boylan-Kolchin M., Garrison-Kimmel S., Qi Y., 2019, MNRAS, 488, 4585

Green S. B., van den Bosch F. C., Jiang F., 2021, MNRAS, 503, 4075

Green S. B., van den Bosch F. C., Jiang F., 2022, MNRAS, 509, 2624

Gunn J. E., Gott J. Richard I., 1972, ApJ, 176, 1

Guo Q., White S., 2014, MNRAS, 437, 3228

Guo Q., White S., Li C., Boylan-Kolchin M., 2010, MNRAS, 404, 1111

Gutcke T. A., Pakmor R., Naab T., Springel V., 2021, MNRAS, 501, 5597

Gutcke T. A., Pfrommer C., Bryan G. L., Pakmor R., Springel V., Naab T., 2022, ApJ, 941, 120

Guth A. H., 1981, Phys. Rev. D, 23, 347

Guth A. H., Pi S. Y., 1982, Phys. Rev. Lett., 49, 1110

Guzzo L., et al., 2008, Nature, 451, 541

Hafele J. C., Keating R. E., 1972, Science, 177, 168

Hahn O., Abel T., 2011, MNRAS, 415, 2101

Haidar H., et al., 2022, MNRAS, 514, 4912

Han J., Cole S., Frenk C. S., Benitez-Llambay A., Helly J., 2018, MNRAS, 474, 604

Hannestad S., Upadhye A., Wong Y. Y. Y., 2020, J. Cosmology Astropart. Phys., 2020, 062

Harvey D., Massey R., Kitching T., Taylor A., Tittley E., 2015, Science, 347, 1462

Hawking S. W., 1982, Physics Letters B, 115, 295

He Q., et al., 2020, MNRAS, 496, 4717

Helmi A., White S. D. M., 1999, MNRAS, 307, 495

Helmi A., Babusiaux C., Koppelman H. H., Massari D., Veljanoski J., Brown A. G. A., 2018, Nature, 563, 85

Hoeft M., Yepes G., Gottlöber S., Springel V., 2006, MNRAS, 371, 401

Hofmann S., Schwarz D. J., Stöcker H., 2001, Phys. Rev. D, 64, 083507

Hohl F., 1971, ApJ, 168, 343

Holley-Bockelmann K., Weinberg M., Katz N., 2005, MNRAS, 363, 991

Holtzman J. A., 1989, ApJS, 71, 1

Hopkins P. F., Bahcall N. A., Bode P., 2005, ApJ, 618, 1

Hopkins P. F., et al., 2018, MNRAS, 480, 800

Hubble E. P., 1926, ApJ, 64, 321

Hubble E., 1929, Proceedings of the National Academy of Science, 15, 168

Ibata R. A., Lewis G. F., Irwin M. J., Quinn T., 2002, MNRAS, 332, 915

Ibata R. A., et al., 2013, Nature, 493, 62

Ibe M., Yu H.-B., 2010, Physics Letters B, 692, 70

Ivezić Ž., et al., 2019, ApJ, 873, 111

Jeltema T., Profumo S., 2016, MNRAS, 458, 3592

Jenkins A., 2010, MNRAS, 403, 1859

Jenkins A., Frenk C. S., White S. D. M., Colberg J. M., Cole S., Evrard A. E., Couchman H. M. P., Yoshida N., 2001, MNRAS, 321, 372

Jethwa P., Erkal D., Belokurov V., 2018, MNRAS, 473, 2060

Jiang F., van den Bosch F. C., 2016, Monthly Notices of the Royal Astronomical Society, 458, 2848

Jiang L., Helly J. C., Cole S., Frenk C. S., 2014, MNRAS, 440, 2115

Jin S., et al., 2023, MNRAS,

Johnston K. V., Spergel D. N., Hernquist L., 1995, ApJ, 451, 598

Johnston K. V., Zhao H., Spergel D. N., Hernquist L., 1999, ApJ, 512, L109

Johnston K. V., Bullock J. S., Sharma S., Font A., Robertson B. E., Leitner S. N., 2008, ApJ, 689, 936

Kahn F. D., Woltjer L., 1959, ApJ, 130, 705

Kaiser N., 1984, ApJ, 284, L9

Kaplinghat M., Tulin S., Yu H.-B., 2016, Phys. Rev. Lett., 116, 041302

Kapteyn J. C., 1922, ApJ, 55, 302

Kataria S. K., Das M., 2019, ApJ, 886, 43

Katz H., et al., 2020, MNRAS, 494, 2200

Kauffmann G., White S. D. M., Guiderdoni B., 1993, MNRAS, 264, 201

Kazantzidis S., Kravtsov A. V., Zentner A. R., Allgood B., Nagai D., Moore B., 2004, ApJ, 611, L73

Kazantzidis S., Łokas E. L., Callegari S., Mayer L., Moustakas L. A., 2011, ApJ, 726, 98

Kelley T., Bullock J. S., Garrison-Kimmel S., Boylan-Kolchin M., Pawlowski M. S., Graus A. S., 2019, MNRAS, 487, 4409

Kelly A. J., Jenkins A., Deason A., Fattahi A., Grand R. J. J., Pakmor R., Springel V., Frenk C. S., 2021, arXiv e-prints, p. arXiv:2106.08618

Kelly A. J., Jenkins A., Deason A., Fattahi A., Grand R. J. J., Pakmor R., Springel V., Frenk C. S., 2022, MNRAS, 514, 3113

Khimey D., Bose S., Tacchella S., 2021, MNRAS, 506, 4139

King S. F., 2015, Journal of Physics G Nuclear Physics, 42, 123001

Kleyna J. T., Wilkinson M. I., Evans N. W., Gilmore G., 2001, ApJ, 563, L115

Klypin A., Kravtsov A. V., Valenzuela O., Prada F., 1999, ApJ, 522, 82

Knebe A., et al., 2011, MNRAS, 415, 2293

Knebe A., et al., 2013, MNRAS, 435, 1618

Knollmann S. R., Knebe A., 2009, ApJS, 182, 608

Koppelman H. H., Helmi A., Massari D., Price-Whelan A. M., Starkenburg T. K., 2019, A&A, 631, L9

Kroupa P., Theis C., Boily C. M., 2005, A&A, 431, 517

Kunkel W. E., Demers S., 1976, in The Galaxy and the Local Group. p. 241

Kusenko A., Steinhardt P. J., 2001, Phys. Rev. Lett., 87, 141301

Lada C. J., Lombardi M., Alves J. F., 2009, ApJ, 703, 52

Lagattuta D. J., et al., 2023, MNRAS, 522, 1091

Lane J. M. M., Bovy J., Mackereth J. T., 2022, MNRAS, 510, 5119

Laporte C. F. P., White S. D. M., Naab T., Ruszkowski M., Springel V., 2012, MNRAS, 424, 747

Lemaître G., 1927, Annales de la Société Scientifique de Bruxelles, 47, 49

Lemaître G., 1931, Nature, 127, 706

Libeskind N. I., Frenk C. S., Cole S., Jenkins A., Helly J. C., 2009, MNRAS, 399, 550

Linde A. D., 1982, Physics Letters B, 108, 389

Łokas E. L., Ebrová I., del Pino A., Sybilska A., Athanassoula E., Semczuk M., Gajda G., Fouquet S., 2016, ApJ, 826, 227

Lovell M. R., Frenk C. S., Eke V. R., Jenkins A., Gao L., Theuns T., 2014, MNRAS, 439, 300

Ludlow A. D., Navarro J. F., Angulo R. E., Boylan-Kolchin M., Springel V., Frenk C., White S. D. M., 2014, MNRAS, 441, 378

Ludlow A. D., Bose S., Angulo R. E., Wang L., Hellwing W. A., Navarro J. F., Cole S., Frenk C. S., 2016, MNRAS, 460, 1214

Ludlow A. D., et al., 2017, Phys. Rev. Lett., 118, 161103

Lynden-Bell D., 1976, MNRAS, 174, 695

Lynden-Bell D., 1979, MNRAS, 187, 101

Lynden-Bell D., 1981, The Observatory, 101, 111

Lynden-Bell D., Kalnajs A. J., 1972, MNRAS, 157, 1

Lynden-Bell D., Wood R., 1968, MNRAS, 138, 495

Ma E., 1998, Phys. Rev. Lett., 81, 1171

Mackereth J. T., et al., 2019, MNRAS, 482, 3426

Majewski S. R., et al., 2017, AJ, 154, 94

Mandelbaum R., Seljak U., Cool R. J., Blanton M., Hirata C. M., Brinkmann J., 2006, MNRAS, 372, 758

Mansfield P., Darragh-Ford E., Wang Y., Nadler E. O., Wechsler R. H., 2023, arXiv e-prints, p. arXiv:2308.10926

Marasco A., Oman K. A., Navarro J. F., Frenk C. S., Oosterloo T., 2018, MNRAS, 476, 2168

Marrodán Undagoitia T., Rauch L., 2016, Journal of Physics G Nuclear Physics, 43, 013001

Martínez-Delgado D., et al., 2021, A&A, 652, A48

Martinez-Valpuesta I., Aguerri J. A. L., González-García A. C., Dalla Vecchia C., Stringer M., 2017, MNRAS, 464, 1502

Martizzi D., Teyssier R., Moore B., 2013, MNRAS, 432, 1947

Mashchenko S., Couchman H. M. P., Wadsley J., 2006, Nature, 442, 539

Mathews W. G., 1978, ApJ, 219, 413

Mau S., et al., 2020, ApJ, 890, 136

McConnachie A. W., 2012, AJ, 144, 4

McDonald J., 2002, Phys. Rev. Lett., 88, 091304

McGaugh S. S., 2012, AJ, 143, 40

McGaugh S. S., Lelli F., Schombert J. M., 2016, Phys. Rev. Lett., 117, 201101

Menéndez-Delmestre K., Sheth K., Schinnerer E., Jarrett T. H., Scoville N. Z., 2007, ApJ, 657, 790

Metz M., Kroupa P., Jerjen H., 2007, MNRAS, 374, 1125

Metz M., Kroupa P., Libeskind N. I., 2008, ApJ, 680, 287

Milgrom M., 1983, ApJ, 270, 371

Milgrom M., 1988, ApJ, 333, 689

Miller R. H., Prendergast K. H., Quirk W. J., 1970, ApJ, 161, 903

Miller A. D., et al., 1999, ApJ, 524, L1

Monachesi A., et al., 2019, MNRAS, 485, 2589

Moore B., 1994, Nature, 370, 629

Moore B., Ghigna S., Governato F., Lake G., Quinn T., Stadel J., Tozzi P., 1999, ApJ, 524, L19

More S., Kravtsov A. V., Dalal N., Gottlöber S., 2011, ApJS, 195, 4

Moster B. P., Somerville R. S., Maulbetsch C., van den Bosch F. C., Macciò A. V., Naab

T., Oser L., 2010, ApJ, 710, 903

Moster B. P., Naab T., White S. D. M., 2013, MNRAS, 428, 3121

Müller O., Scalera R., Binggeli B., Jerjen H., 2017, A&A, 602, A119

Myeong G. C., Vasiliev E., Iorio G., Evans N. W., Belokurov V., 2019, MNRAS, 488, 1235

Nadler E. O., Mao Y.-Y., Green G. M., Wechsler R. H., 2019, ApJ, 873, 34

Nadler E. O., et al., 2020, ApJ, 893, 48

Nadler E. O., Banerjee A., Adhikari S., Mao Y.-Y., Wechsler R. H., 2021, ApJ, 920, L11

Nadler E. O., et al., 2023, ApJ, 945, 159

Naidu R. P., Conroy C., Bonaca A., Johnson B. D., Ting Y.-S., Caldwell N., Zaritsky D., Cargile P. A., 2020, ApJ, 901, 48

Navarro J. F., Frenk C. S., White S. D. M., 1995, MNRAS, 275, 720

Navarro J. F., Eke V. R., Frenk C. S., 1996a, MNRAS, 283, L72

Navarro J. F., Frenk C. S., White S. D. M., 1996b, ApJ, 462, 563

Navarro J. F., Frenk C. S., White S. D. M., 1997, ApJ, 490, 493

Navarro J. F., et al., 2004, MNRAS, 349, 1039

Ness M., et al., 2016, ApJ, 819, 2

Neto A. F., et al., 2007, MNRAS, 381, 1450

Newton O., Cautun M., Jenkins A., Frenk C. S., Helly J. C., 2018, MNRAS, 479, 2853

Nishikawa H., Boddy K. K., Kaplinghat M., 2020, Phys. Rev. D, 101, 063009

Nissen P. E., Schuster W. J., 1997, A&A, 326, 751

Nissen P. E., Schuster W. J., 2010, A&A, 511, L10

Noguchi M., 1987, MNRAS, 228, 635

Nordtvedt K., 1968, Physical Review, 170, 1186

Oñorbe J., Boylan-Kolchin M., Bullock J. S., Hopkins P. F., Kereš D., Faucher-Giguère C.-A., Quataert E., Murray N., 2015, MNRAS, 454, 2092

Oh S.-H., et al., 2015, AJ, 149, 180

Okamoto T., Frenk C. S., 2009, MNRAS, 399, L174

Oldham L. J., Auger M. W., 2018, MNRAS, 476, 133

Oman K. A., et al., 2015, MNRAS, 452, 3650

Oman K. A., Marasco A., Navarro J. F., Frenk C. S., Schaye J., Benítez-Llambay A., 2019, MNRAS, 482, 821

Oort J. H., 1932, Bull. Astron. Inst. Netherlands, 6, 249

Ostriker J. P., Peebles P. J. E., 1973, ApJ, 186, 467

Pakmor R., et al., 2023, MNRAS, 524, 2539

Papastergis E., Giovanelli R., Haynes M. P., Shankar F., 2015, Astron. Astrophys., 574, A113

Pardo K., Spergel D. N., 2020, Phys. Rev. Lett., 125, 211101

Pati J. C., Salam A., 1974, Phys. Rev. D, 10, 275

Pawlowski M. S., Kroupa P., 2013, MNRAS, 435, 2116

Pawlowski M. S., Pflamm-Altenburg J., Kroupa P., 2012, MNRAS, 423, 1109

Peñarrubia J., Benson A. J., Walker M. G., Gilmore G., McConnachie A. W., Mayer L., 2010, MNRAS, 406, 1290

Pearson S., Price-Whelan A. M., Johnston K. V., 2017, Nature Astronomy, 1, 633

Peccei R. D., Quinn H. R., 1977, Phys. Rev. Lett., 38, 1440

Peebles P. J. E., 1971, Physical cosmology

Peebles P. J. E., Yu J. T., 1970, ApJ, 162, 815

Penzias A. A., Wilson R. W., 1965, ApJ, 142, 419

Peter A. H. G., Rocha M., Bullock J. S., Kaplinghat M., 2013, MNRAS, 430, 105

Planck Collaboration et al., 2014, A&A, 571, A1

Planck Collaboration et al., 2020a, A&A, 641, A1

Planck Collaboration et al., 2020b, A&A, 641, A6

Pointecouteau E., Silk J., 2005, MNRAS, 364, 654

Pontzen A., Governato F., 2012, MNRAS, 421, 3464

Pontzen A., Governato F., 2014, Nature, 506, 171

Power C., Robotham A. S. G., 2016, ApJ, 825, 31

Power C., Navarro J. F., Jenkins A., Frenk C. S., White S. D. M., Springel V., Stadel J., Quinn T., 2003, MNRAS, 338, 14

Psaltis D., et al., 2020, Phys. Rev. Lett., 125, 141104

Purcell C. W., Bullock J. S., Kazantzidis S., 2010, MNRAS, 404, 1711

Randall S. W., Markevitch M., Clowe D., Gonzalez A. H., Bradac M., 2008, Astrophys. J., 679, 1173

Read J. I., Gilmore G., 2005, MNRAS, 356, 107

Read J. I., Pontzen A. P., Viel M., 2006a, MNRAS, 371, 885

Read J. I., Goerdt T., Moore B., Pontzen A. P., Stadel J., Lake G., 2006b, Mon. Not. Roy. Astron. Soc., 373, 1451

Read J. I., Agertz O., Collins M. L. M., 2016, MNRAS, 459, 2573

Read J. I., Iorio G., Agertz O., Fraternali F., 2017, MNRAS, 467, 2019

Read J. I., Walker M. G., Steger P., 2018, MNRAS, 481, 860

Read J. I., Walker M. G., Steger P., 2019, MNRAS, 484, 1401

Rey M. P., Pontzen A., Agertz O., Orkney M. D. A., Read J. I., Saintonge A., Pedersen C., 2019, ApJ, 886, L3

Richings J., et al., 2020, MNRAS, 492, 5780

Riess A. G., et al., 1998, AJ, 116, 1009

Roach B. M., et al., 2023, Phys. Rev. D, 107, 023009

Roberts M. S., Whitehurst R. N., 1975, ApJ, 201, 327

Robertson A., Massey R., Eke V., 2017, MNRAS, 465, 569

Robertson A., et al., 2018, MNRAS, 476, L20

Robertson A., Massey R., Eke V., Schaye J., Theuns T., 2021, MNRAS, 501, 4610

Rocha M., Peter A. H. G., Bullock J. S., Kaplinghat M., Garrison-Kimmel S., Oñorbe J., Moustakas L. A., 2013, MNRAS, 430, 81

Rodríguez-Torres S. A., et al., 2016, MNRAS, 460, 1173

Roper F. A., Oman K. A., Frenk C. S., Benítez-Llambay A., Navarro J. F., Santos-Santos I. M. E., 2022, arXiv e-prints, p. arXiv:2203.16652

Rubin V. C., Ford W. Kent J., 1970, ApJ, 159, 379

Ryden B. S., Gunn J. E., 1987, ApJ, 318, 15

Saha K., Martinez-Valpuesta I., Gerhard O., 2012, MNRAS, 421, 333

Sales L. V., Wetzel A., Fattahi A., 2022, Nature Astronomy, 6, 897

Sand D. J., Treu T., Ellis R. S., 2002, ApJ, 574, L129

Sanders R. H., 2003, MNRAS, 342, 901

Sanders R. H., Huntley J. M., 1976, ApJ, 209, 53

Sanderson R. E., et al., 2018, ApJ, 869, 12

Santos-Santos I. M. E., Fattahi A., Sales L. V., Navarro J. F., 2021, MNRAS, 504, 4551

Sawala T., Frenk C. S., Crain R. A., Jenkins A., Schaye J., Theuns T., Zavala J., 2013, MNRAS, 431, 1366

Sawala T., et al., 2016, MNRAS, 457, 1931

Sawala T., Pihajoki P., Johansson P. H., Frenk C. S., Navarro J. F., Oman K. A., White S. D. M., 2017, MNRAS, 467, 4383

Sawala T., et al., 2023, Nature Astronomy, 7, 481

Schaller M., et al., 2015, MNRAS, 451, 1247

Schaller M., et al., 2016, MNRAS, 455, 4442

Schaye J., 2004, ApJ, 609, 667

Schaye J., Dalla Vecchia C., 2008, MNRAS, 383, 1210

Schaye J., et al., 2015, MNRAS, 446, 521

Schaye J., et al., 2023, arXiv e-prints, p. arXiv:2306.04024

Searle L., Zinn R., 1978, ApJ, 225, 357

Sellwood J. A., 2006, ApJ, 637, 567

Sellwood J. A., 2008, ApJ, 679, 379

Sestito F., et al., 2023a, arXiv e-prints, p. arXiv:2301.13214

Sestito F., Roediger J., Navarro J. F., Jensen J., Venn K. A., Smith S. E. T., Hayes C., McConnachie A. W., 2023b, MNRAS, 523, 123

Shapiro I. I., 1964, Phys. Rev. Lett., 13, 789

Sheth K., et al., 2008, ApJ, 675, 1141

Simha V., Cole S., 2017, MNRAS, 472, 1392

Skibba R. A., et al., 2012, MNRAS, 423, 1485

Skordis C., Złośnik T., 2021, Phys. Rev. Lett., 127, 161302

Slipher V. M., 1917, Proceedings of the American Philosophical Society, 56, 403

Somerville R. S., Davé R., 2015, ARA&A, 53, 51

Spergel D. N., Steinhardt P. J., 2000, Phys. Rev. Lett., 84, 3760

Spergel D. N., et al., 2003, ApJS, 148, 175

Springel V., 2005, MNRAS, 364, 1105

Springel V., White S. D. M., Tormen G., Kauffmann G., 2001, MNRAS, 328, 726

Springel V., Di Matteo T., Hernquist L., 2005a, MNRAS, 361, 776

Springel V., et al., 2005b, Nature, 435, 629

Springel V., Frenk C. S., White S. D. M., 2006, Nature, 440, 1137

Springel V., et al., 2008, MNRAS, 391, 1685

Springel V., Pakmor R., Zier O., Reinecke M., 2021, MNRAS, 506, 2871

Srisawat C., et al., 2013, MNRAS, 436, 150

Starobinsky A. A., 1982, Physics Letters B, 117, 175

Strigari L. E., Frenk C. S., White S. D. M., 2010, Monthly Notices of the Royal Astronomical Society, 408, 2364–2372

Stücker J., Ogiya G., Angulo R. E., Aguirre-Santaella A., Sánchez-Conde M. A., 2023a, MNRAS, 521, 4432

Stücker J., Ogiya G., White S. D. M., Angulo R. E., 2023b, MNRAS, 523, 1067

Sunyaev R. A., Zeldovich Y. B., 1970, Ap&SS, 7, 3

Taylor J. H., Weisberg J. M., 1989, ApJ, 345, 434

Teyssier R., Pontzen A., Dubois Y., Read J. I., 2013, MNRAS, 429, 3068

The Dark Energy Survey Collaboration 2005, arXiv e-prints, pp astro–ph/0510346

Tollet E., et al., 2016, MNRAS, 456, 3542

Tormen G., Diaferio A., Syer D., 1998, MNRAS, 299, 728

Torrealba G., Koposov S. E., Belokurov V., Irwin M., 2016, MNRAS, 459, 2370

Torrealba G., et al., 2019, MNRAS, 488, 2743

Touboul P., et al., 2022, Phys. Rev. Lett., 129, 121102

Treu T., Koopmans L. V. E., 2004, ApJ, 611, 739

Turner H. C., Lovell M. R., Zavala J., Vogelsberger M., 2021, MNRAS, 505, 5327

Tyson J. A., Kochanski G. P., Dell'Antonio I. P., 1998, ApJ, 498, L107

Umetsu K., Diemer B., 2017, ApJ, 836, 231

Vasiliev E., 2019, MNRAS, 482, 1525

Vegetti S., Koopmans L. V. E., Bolton A., Treu T., Gavazzi R., 2010, MNRAS, 408, 1969

Vegetti S., Lagattuta D. J., McKean J. P., Auger M. W., Fassnacht C. D., Koopmans L. V. E., 2012, Nature, 481, 341

Vessot R. F. C., et al., 1980, Phys. Rev. Lett., 45, 2081

Villaescusa-Navarro F., et al., 2021, ApJ, 915, 71

Vogelsberger M., Zavala J., Loeb A., 2012, MNRAS, 423, 3740

Vogelsberger M., Zavala J., Simpson C., Jenkins A., 2014, MNRAS, 444, 3684

Vogelsberger M., Zavala J., Cyr-Racine F.-Y., Pfrommer C., Bringmann T., Sigurdson K., 2016, Mon. Not. Roy. Astron. Soc., 460, 1399

Voigt L. M., Fabian A. C., 2006, MNRAS, 368, 518

Wagoner R. V., Fowler W. A., Hoyle F., 1967, ApJ, 148, 3

Walker M. G., Peñarrubia J., 2011, ApJ, 742, 20

Waller F., et al., 2023, MNRAS, 519, 1349

Wambsganss J., Bode P., Ostriker J. P., 2004, ApJ, 606, L93

Wang J., White S. D. M., 2007, MNRAS, 380, 93

Wang L., Li C., Kauffmann G., De Lucia G., 2006, MNRAS, 371, 537

Wang L., Dutton A. A., Stinson G. S., Macciò A. V., Penzo C., Kang X., Keller B. W., Wadsley J., 2015, MNRAS, 454, 83

Wang J., Bose S., Frenk C. S., Gao L., Jenkins A., Springel V., White S. D. M., 2020, Nature, 585, 39

Weiland J. L., et al., 1994, ApJ, 425, L81

Weinberg S., 2008, Cosmology

Weinberg M. D., Katz N., 2002, ApJ, 580, 627

Weinberg M. D., Katz N., 2007a, MNRAS, 375, 425

Weinberg M. D., Katz N., 2007b, MNRAS, 375, 460

Wess J., Zumino B., 1974, Nucl. Phys. B, 70, 39

Wheeler C., Oñorbe J., Bullock J. S., Boylan-Kolchin M., Elbert O. D., Garrison-Kimmel S., Hopkins P. F., Kereš D., 2015, MNRAS, 453, 1305

White S. D. M., Rees M. J., 1978, MNRAS, 183, 341

White S. D. M., Frenk C. S., Davis M., 1983, ApJ, 274, L1

Wiersma R. P. C., Schaye J., Smith B. D., 2009, MNRAS, 393, 99

Wirtz C., 1924, Astronomische Nachrichten, 222, 21

Woo J., Courteau S., Dekel A., 2008, MNRAS, 390, 1453

XRISM Science Team 2020, arXiv e-prints, p. arXiv:2003.04962

Yue B., Chen X., 2012, ApJ, 747, 127

Zavala J., Okamoto T., Frenk C. S., 2008, MNRAS, 387, 364

Zel'dovich Y. B., 1970, A&A, 5, 84

Zhao H., 1996, MNRAS, 278, 488

Zolotov A., et al., 2012, ApJ, 761, 71

Zwicky F., 1933, Helvetica Physica Acta, 6, 110

de Bernardis P., et al., 2000, Nature, 404, 955

de Blok W. J. G., 2010, Advances in Astronomy, 2010, 789293

de Blok W. J. G., Walter F., Brinks E., Trachternach C., Oh S. H., Kennicutt R. C. J., 2008, AJ, 136, 2648

de Sitter W., 1917, MNRAS, 78, 3

van den Bosch F. C., Ogiya G., 2018, MNRAS, 475, 4066